NTNU
Norwegian University of
Science and Technology

Development of an asymmetrical oxygen permeable membrane based on hexagonal manganites

Stine Marie Hoggen

Chemical Engineering and Biotechnology
Submission date: September 2016
Supervisor: Sverre Magnus Selbach, IMTE
Co-supervisor: Sandra Helen Skjærvø, IMTE
Didrik René Småbråten, IMTE

Norwegian University of Science and Technology
Department of Materials Science and Engineering

Declaration

M.Sc. Candidate: Stine Marie Hoggen

Supervisor: Ass. Prof. Sverre Magnus Selbach

Co-supervisors: Ph.D. Candidates Sandra Helen Skjærvø and Didrik René Småbråten

This study has been performed at the Norwegian University of Science and Technology (NTNU) at the Department of Materials Science and Engineering. The work was conducted from April to September 2016. I hereby declare that this work has been conducted honestly and independently and that all used references have been denoted.

Trondheim, September 6th 2016

Stine Marie Hoggen

Stine Marie Hoggen

Acknowledgments

There are so many people that deserve my gratitude for helping me during my master's thesis. First of all, I would like to thank my supervisor, Associate Professor Sverre Magnus Selbach, for his dedication and knowledge about practically everything. His belief in the importance of this study has been very encouraging and has helped me stay motivated throughout this work. My co-supervisors Sandra Helen Skjærvø and Didrik René Småbråten also deserve thanks for setting aside time to answer my questions and giving me feedback. I would also like to thank the technical staff in the department for their invaluable help in the lab. Without them, my work would have come to a halt many times. Finally, I would like to thank my friends and family for always supporting me and being there for me. Without them it would have been almost impossible to finish this thesis. I especially need to thank Ove Øyås for teaching me how to make nice figures and graphs, but most of all for his invaluable encouragement and cheering up.

Abstract

Pure oxygen is a commodity chemical needed in many industries. Separation of oxygen from air is usually performed by the expensive and highly energy-demanding process of cryogenic distillation. A promising and more environmentally friendly alternative is the use of dense oxygen permeable membranes. The state-of-the-art perovskite membranes require high operating temperatures (600–1000 °C), which lead to membrane degradation and a short lifetime. There is a need for a new type of membrane material that will transport a sufficient amount of oxygen at lower temperatures. Hexagonal manganites have a crystal structure that allows for the incorporation of highly mobile interstitial oxygen ions, as opposed to the more dense perovskites, which need formation of oxygen vacancies to conduct oxygen. The incorporation of oxygen ions requires less energy than the formation of vacancies, and oxygen conduction can occur at lower temperatures (200–300 °C). This makes hexagonal manganites very good candidates for oxygen permeable membranes. Hexagonal manganites often have highly anisotropic thermal expansion, which can cause microcracking in the membrane and reduced mechanical stability. Doping of hexagonal $YMnO_3$ with titanium has shown to reduce this anisotropy and decrease the amount of microcracking in the material.

The aim of this study has been to find a fabrication route for an asymmetrical ceramic membrane based on titanium doped hexagonal $YMnO_3$. The solid state synthesis was used to create the porous support of the membrane, and the citric acid method was used to fabricate the nanoparticles for the functioning thin film. The nanoparticles were dispersed in a suspension and deposited onto the substrate using various deposition methods. The deposition techniques were spray coating, dip coating and drop casting, with drop casting giving the best results. The effect of the sintering temperature on the density of the film was also tested, showing that sintering at 1400 °C or above was necessary to achieve a dense film. Yttrium vacancies were introduced in the material to test the effect on its sintering properties, and it was found that yttrium deficiency increases densification. A dense thin film was achieved by drop casting very fine particles of $YMn_{0.85}Ti_{0.15}O_3$ onto a support, and sintering at 1400 °C for one hour. Finally, a strategy in further development of the deposition technique is proposed in order to optimize the fabrication route.

Samandrag

Rein oksygen er eit viktig kjemikalie i mange industriar. Separasjon av oksygen frå luft vert vanlegvis utført ved hjelp av den energikrevjande og dyre metoden kryogensk destillasjon. Eit lovande og meir miljøvenleg alternativ er å bruke tette oksygenpermeable membranar. Dagens state-of-the-art perovskitt-membranar krev høge driftstemperaturar (600–1000 °C), noko som fører til degradering av membranen og ei kort levetid. Det trengs ein ny type material som kan transportere oksygen ved lågare temperaturar. Heksagonale manganittar har ein krystallstruktur som gjer at dei kan ta opp interstitielle oksygenion med høg mobilitet, i motsetnad til den tettare perovskittstrukturen som treng oksygenvakansar for å leie oksygen. Opptak av oksygenion i strukturen krev mindre energi enn danning av oksygenvakansar, og oksygenleiing kan dermed skje ved lågare temperaturar (200–300 °C). Heksagonale manganittar er dermed gode kandidatar for bruk i oksygenpermeable membranar. Heksagonale manganittat har ofte ein anisotropisk termisk ekspansjon, noko som kan føre til danning av mikrosprekker i materialet og redusert mekanisk stabilitet. Doping av materialet med titan har vist seg å redusere denne anisotropien og danninga av mikrosprekker.

Målet med denne oppgåva har vore å finne ein fabrikasjonsmetode for ein asymmetrisk keramisk membran basert på heksagonal $YMnO_3$ dopa med titan. Faststoffmetoden vart nytta for å lage den porøse beraren, og sitronsyresyntesen vart brukt for å lage nanopartiklane nytta i den funksjonelle tynnfilmen. Nanopartiklane vart spreidd i ein suspensjon og deponert på beraren ved hjelp av ulike deponeringsmetodar. Deponeringsmetodane var spray coating, dip coating, og drop casting, der drop casting gav det beste resultatet. Effekten av sinteringstemperatur vart også testa, og det vart fastslått at ein temperatur på minst 1400 °C er nødvendig for å få ein tett tynnfilm. Yttrium-underskot vart også introdusert i materialet for å undersøkje effekten på sintringseigenskapane. Det vart fastslått at yttrium-underskot aukar fortetting av materialet. Ein tett tynnfilm vart oppnådd ved drop casting av $YMn_{0.85}Ti_{0.15}O_3$ nanopartiklar på ein berar og sintring ved 1400 °C i ein time. Ein strategi for vidare optimalisering av fabrikasjonmetoden vert foreslått.

Contents

Chapter 1

Introduction

Pure oxygen is a widely used commodity chemical with applications in several different industrial sectors. Since air consists of 21% oxygen, separation of oxygen from air is a good way of obtaining pure oxygen and is therefore a major industry. Nearly 100 million tons of oxygen are produced every year, and the demand is expected to grow [1, 2]. Pure oxygen plays an important role in the renewable energy industry, as most large-scale clean energy technologies require oxygen as a feed [1]. Pure oxygen can also be used in the production of syn-gas (CO + H_2), an important intermediate in the production of hydrogen. It is also used in the conversion of methane to a number of important products, such as parafins, olefins, and alcohols, most importantly methanol [3]. Other applications of pure oxygen are in oxy-fuel combustion for CO_2 capture in power plants [4], metallurgical industry, food industry, clean waste incineration, and for medical purposes [5]. Given this diversity of the oxygen industry and its areas of application, it is evident that there is a need for an energy-efficient and low-cost method of producing pure oxygen.

The conventional method of producing pure oxygen by separation from air is cryogenic distillation. This method operates at supercooled temperatures down to −185 °C and at high pressures in order to distill oxygen from liquid air [2, 5]. These operating conditions require a substantial amount of energy, which makes this process both costly and bad for the environment. In syn-gas production a cryogenic oxygen plant may comprise 45% of the total investment cost [3]. An alternative to the expensive cryogenic distillation is the use of ceramic membranes for oxygen separation. These membranes are selective purely to oxygen, ensuring that all other elements are retained on the feed side of the membrane. By replacing cryogenic distillation with dense ceramic membranes, the cost of oxygen production is estimated to be reduced by 35% [6]. Energy demand will also be greatly reduced, making the process more environmentally friendly as well as economical.

1.1 Mixed ionic-electronic conducting membranes

There are generally two types of membranes that are used for oxygen separation from air: pure oxygen conducting membranes and mixed ionic-electronic conducting (MIEC) membranes [7]. These types of membranes are dense, so the direct transport of oxygen molecules, along with other molecules, is blocked. The oxygen is transported through the membrane as O^{2-} ions, which ensures that, as long as the membrane does not have any defects, the permeate stream can consist of up to 100% pure oxygen [2]. The transportation of charged oxygen ions through the membrane will require an opposite flow of electrons in order to preserve the electroneutrality of the material. This can also be thought of as a flow of holes in the same direction as the oxygen ions.

The pure oxygen conducting membranes need electrodes to allow the opposite flow of electrons. The advantage of this type of membranes is that the oxygen flux through the membrane can be precisely controlled by the application of an electric current, and it is directly proportional to the current flowing through the cell [1, 5, 7]. The mixed ionic-electronic conducting (MIEC) membranes have the advantage that they do not need an external circuit for the charge compensating electron flow, as the material itself will conduct electrons. However, they do need a driving force to transport the oxygen ions through the membrane, which is provided by the difference in oxygen partial pressure through the membrane [1, 2, 5, 7]. This will cause the O^{2-} ions to migrate from the high oxygen partial pressure side (feed side) to the low oxygen partial pressure side (permeate side). The MIEC membrane essentially acts as a barrier between two chambers and only oxygen ions can pass through [8]. Figure 1.1 shows a schematic drawing of a MIEC asymmetric membrane with a dense, functional thin film on a porous support. A thin, functional layer reduces the necessary solid state diffusion of the oxygen ions, while the porous support increases the mechanical strength of the membrane so that it is able to withstand the difference in pressure across the membrane.

The mechanism for oxygen transport across the functional layer of the membrane at steady-state conditions is shown in Figure 1.2. The feed provides compressed air and a high oxygen partial pressure, while the permeate side contains the transported oxygen and a low oxygen partial pressure. This difference in the partial pressure of oxygen creates a gradient in oxygen chemical potential, $\Delta\mu_{O_2}$, which is the driving force for the oxygen ions through the membrane [9]. The transport of oxygen can be divided into three regions: i) interface 1 at the high oxygen partial pressure side, ii) bulk,

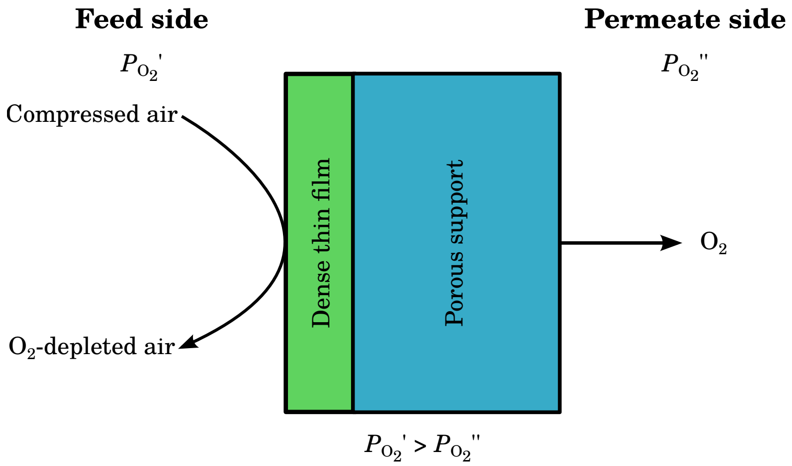

Figure 1.1: A schematic drawing of a mixed ionic-electronic conducting asymmetrical membrane for oxygen separation from air. The membrane consists of a dense, functional thin film and a porous support for mechanical strength. P'_{O_2} and P''_{O_2} is the oxygen partial pressure on the feed and permeate side, respectively.

and iii) interface 2 at the side with low partial pressure of oxygen [10]. At interface 1 surface exchange reactions dominate, where the oxygen molecules are adsorbed to the surface at active adsorption sites and dissociated into oxygen ions. At the bulk region, oxygen ions and electrons/electron holes migrate through the membrane through bulk diffusion. At interface 2 surface exchange reactions dominate again, as the O^{2-} ions recombine into O_2 and desorb from the surface [2, 7, 8]. Each of these three regions can be rate-limiting, and the total resistance to oxygen permeation in the membrane is the sum of the resistances in the equivalent circuit in Figure 1.2. The chemical potential will be distributed between the different regions, and the rate-limiting step will receive the greater proportion [9].

When the membrane is sufficiently thick, bulk diffusion will be the rate-limiting step and hence control the oxygen flux through the membrane. When the thickness decreases, the permeation will be controlled by both bulk diffusion and surface exchange reactions, and for very thin membranes, the kinetics of surface exchange reactions alone will dominate the permeation [9]. When bulk diffusion is the rate-limiting step, the oxygen flux through the membrane can be described by Equation 1.1, derived from Wagner theory [7, 9, 10].

$$J_{O_2} = -\frac{1}{4^2F^2L}\int_{\mu'_{O_2}}^{\mu''_{O_2}} \frac{\sigma_{\text{ion}}\sigma_{\text{el}}}{\sigma_{\text{ion}}+\sigma_{\text{el}}}\, d\mu_{O_2} \tag{1.1}$$

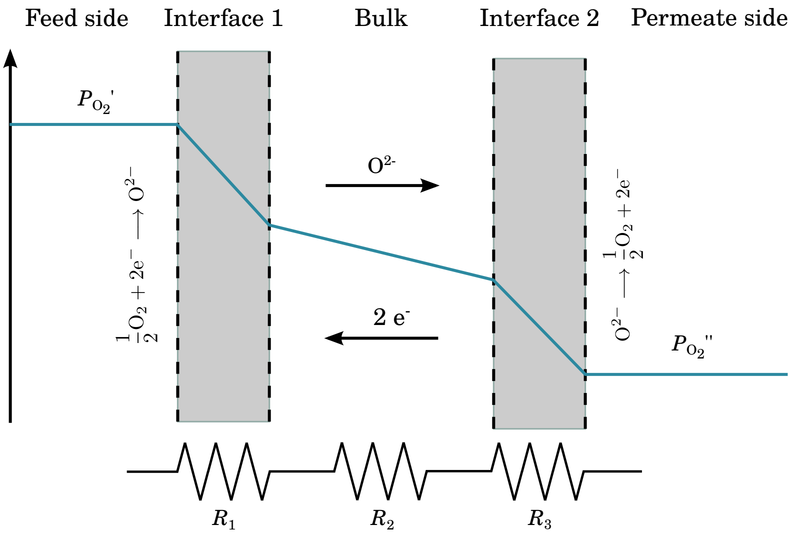

Figure 1.2: A schematic drawing of the transport of oxygen through the mixed ionic-electronic conducting membrane at steady-state conditions. P'_{O_2} and P''_{O_2} is the oxygen partial pressure on the feed and permeate side, respectively.

Here J_{O_2} is the oxygen flux, F is the Faraday constant, L is the membrane thickness, σ_{ion} and σ_{el} are the ionic and electronic conductivities, respectively, and μ_{O_2} is the chemical potential. The integration limits μ'_{O_2} and μ''_{O_2} are the chemical potentials at interface 1 and interface 2, respectively. The Wagner theory assumes that there exists a local equilibrium between the two charged species, in this case O^{2-} and e^-, and a hypothetical neutral species, O_2, in the bulk oxide [7, 10]. The slowest-moving species is thought to limit the rate of oxygen permeation. In this case this will be O^{2-}, giving the assumption that $\sigma_{\text{el}} >> \sigma_{\text{ion}}$. When assuming ideal thermodynamic behavior, the chemical potential of the system is given by $d\mu_{O_2} = RTd\ln P_{O_2}$ [7]. Combining this assumption with $\sigma_{\text{el}} >> \sigma_{\text{ion}}$, Equation 1.1 changes to Equation 1.2 [3, 7, 10],

$$J_{O_2} = -\frac{RT}{4^2F^2L}\int_{\ln P'_{O_2}}^{\ln P''_{O_2}} \sigma_{\text{ion}} d\ln P_{O_2} \tag{1.2}$$

where R is the gas constant, T is the temperature, and P_{O_2} is the partial pressure of oxygen. From this equation it can be seen that the flux of oxygen is directly dependent on the partial pressures of oxygen and the membrane thickness.

Decreasing the thickness of the membrane means that bulk diffusion no longer can be assumed to be the only rate-limiting step for oxygen permeation, and the Wagner equations no longer apply. When the membrane is sufficiently thin, the kinetics of the surface exchange reactions dominate the control of the oxygen flux through the membrane. Surface exchange reactions can involve several sub-steps, which can be O_2 adsorption, dissociation of adsorbed O_2, desorption of adsorbed O_2, and charge transfer reactions [10]. All of these steps might influence the overall permeation rate, and the determination of an explicit flux expression is therefore complicated.

At an intermediate thickness of the film, conditions will arise under which bulk diffusion and surface exchange reactions contribute equally to the oxygen flux. Lin et al. [10] have derived some fundamental equations which show that the oxygen flux through a mixed conducting membrane depends on the oxygen partial pressures on both the feed and permeate side, the electrochemical transport mechanism (electron or electron-hole conduction), initial defect concentrations, the rate constants associated with each rate step, and the thickness of the film. Bouwmeester et al. [9] have given an expression for the oxygen flux in steady-state conditions and derived a characteristic membrane thickness L_c, for which mixed control occurs. This derivation is shown below. The flux equation is given by Equation 1.3 and is only valid at small oxygen potential gradients.

$$J_{O_2} = -j_{ex}^{0'}\frac{\Delta\mu'_{O_2}}{RT} = \frac{\overline{-t_{el}t_{ion}\sigma_{total}}}{4^2F^2}\frac{\Delta\mu^{bulk}_{O_2}}{L} = -j_{ex}^{0''}\frac{\Delta\mu''_{O_2}}{RT} \tag{1.3}$$

Here j_{ex}^0 is a kinetic parameter that represents the exchange rate in the absence of oxygen potential gradients and is related to the surface exchange coefficient, k, by $j_{ex}^0 = 1/2kc_i$, where c_i is the oxygen ion concentration. One prime refers to the high oxygen partial pressure side and two primes to the low partial pressure side. $\Delta\mu^{bulk}_{O_2}$, $\Delta\mu'_{O_2}$, and $\Delta\mu''_{O_2}$ denotes the chemical potentials across the bulk, interface 1 and interface 2, respectively. The fractions of electronic and ionic conductivity are t_{el} and t_{ion}, respectively, over the total conductivity σ_{total}. The factor $\overline{-t_{el}t_{ion}\sigma_{total}}$ is the average of the product across the membrane thickness, L. Under mixed control, $\Delta\mu^{bulk}_{O_2} = \Delta\mu'_{O_2} + \Delta\mu''_{O_2}$. At steady-state and near equilibrium $j_{ex}^{0'} \approx j_{ex}^{0''}$ and $\Delta\mu'_{O_2} \approx \Delta\mu''_{O_2}$. combining the conditions for mixed control and the steady-state conditions gives the characteristic thickness L_c given in Equation 1.4.

$$L_c = \frac{RT}{8F^2}\frac{t_{el}t_{ion}\sigma_{total}}{j_{ex}^0} \tag{1.4}$$

Since the ionic conductivity in this case is much smaller than the electronic conductivity, the expression above depends only on the ionic and not the electronic conductivity. By using the Nernst-Einstein relationship and the relationship between the surface oxygen exchange rate, j_{ex}^0, and the surface exchange coefficient, k, the characteristic thickness can be expressed by the self-diffusion coefficient of oxygen ions, D_i, and the surface exchange coefficient, k. L_c is given in Equation 1.5.

$$L_c = \frac{D_i}{k} \tag{1.5}$$

L_c is a convenient way to distinguish between surface exchange and diffusion-controlled kinetics of oxygen permeation [9]. When $L > L_c$ bulk diffusion is the rate determining step, and when $L < L_c$ the oxygen permeation rate is controlled by the surface exchange reaction [6]. As can be seen by Equation 1.2, the oxygen flux is inversely proportional to the membrane thickness as long as bulk diffusion is rate-limiting. Thus, by decreasing the membrane thickness the oxygen flux will increase. When the kinetics of the surface exchange reactions become rate-limiting, further reduction of the thickness no longer increases the oxygen flux. It is therefore desirable to stay in the mixed control region, where bulk diffusion and surface exchange contribute equally to the oxygen permeation. Figure 1.3a shows a schematic illustration of how the oxygen flux depends on membrane thickness, L, and which mechanism is rate-limiting. Figure 1.3b shows how the oxygen flux varies with membrane thickness and the oxygen partial pressure on the feed side. With decreasing partial pressure of oxygen the characteristic thickness of the membrane increases and the oxygen permeation is increasingly controlled by surface kinetics.

1.2 Material demands

The usual operating temperatures for the perovskite-type membranes are in the range of 600–1000 °C [6, 7]. These temperatures require a large amount of energy and may cause chemical and structural degradation of the membrane [1]. The membranes need to be stable over a wide range of temperatures and oxygen partial pressures [6]. The oxygen chemical potential gradient across the membrane may cause structural failure in perovskite materials due to differential stress. This is a concomitant of the expansion of the unit cell when the transition metal ions are reduced to their larger, lower-valent forms as the oxygen partial pressure is lowered [11]. These operating conditions will lead to mechanical degradation and a short lifetime of the membrane. Hence, a reduction in operating temperature together with enhanced mechanical stability of the membrane would be beneficial.

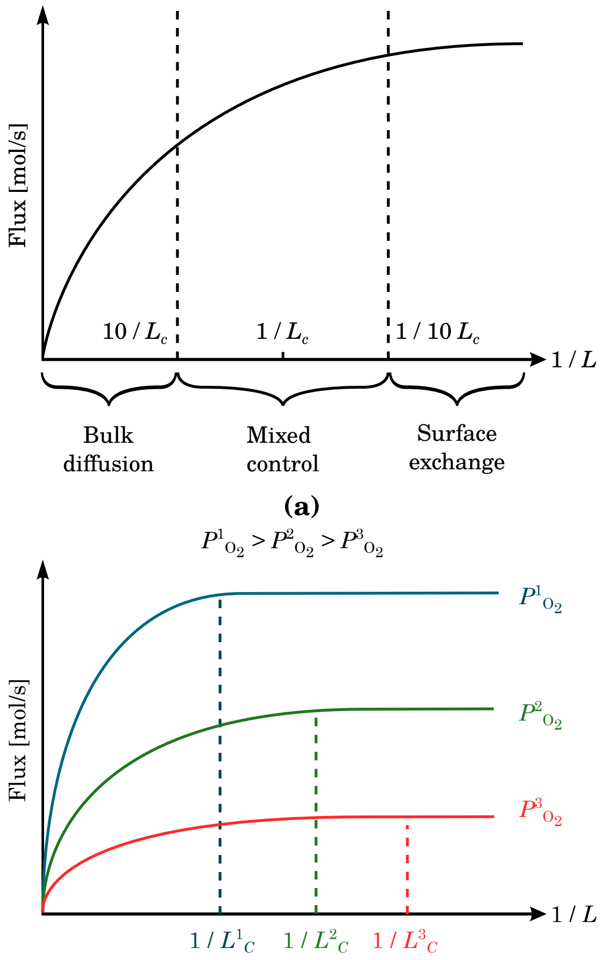

(a)

(b)

Figure 1.3: Schematic illustration of oxygen flux through the membrane as a function of (a) reciprocal membrane thickness, and (b) reciprocal membrane thickness and partial oxygen pressure on the feed side.

Since the oxygen permeation increases with decreasing membrane thickness, the membranes are currently made in the order of tens of micrometers thick [1]. When the thickness of the membrane decreases to below 150 µm, a support must be added for mechanical strength [12]. The oxygen permeation has been shown to increase with the use of an asymmetrical membrane compared to a symmetrical membrane, showing that the asymmetrical configuration is preferable [13].

The approach of making an asymmetrical membrane consisting of a thin, functional film on a porous support has many advantages as summarized by Athayde et al. [2]. This approach makes it possible to use very thin, dense layers (20–65 µm) while having enhanced mechanical stability due to the support. Surface modifications using a porous chemical catalyst can be made, and, most importantly, the membranes produced by this method give the highest reported oxygen fluxes to date. The disadvantages of this preparation method is that the expansion coefficients of the material must match in order to avoid cracking, and pores that are not interconnected in the support will decrease oxygen flux [2]. The support therefore has to be porous enough to allow adequate gas flow while providing sufficient mechanical strength.

1.3 State of the art

The most investigated materials for MIEC membranes are fluorite-type and perovskite-type materials due to their oxygen permeability [1]. The perovskites $Ba_{1-x}Sr_xCo_{1-y}Fe_yO_{3-\delta}$ (BSCF) and $La_{1-x}Sr_xCo_{1-y}Fe_yO_{3-\delta}$ (LSCF) have been most thoroughly studied [2]. The transport of oxygen ions through a perovskite membrane happens through the oxygen vacancies and the oxygen flux will therefore increase with increasing temperature [1].

The oxygen flux needed for economic feasibility is 10 $cm^3cm^{-2}min^{-1}$ [6]. For the perovskite-type materials the oxygen flux is usually in the range of 10^{-6} to 10^{-10} $mols^{-1}cm^{-2}$ between 800–1000 °C [7]. The flux values for BSCF have been reported to be up to 9.5 mL/cm^2min, with the highest values being for tubular membranes, while for disk shape membranes the values are in the range of a few mL/cm^2min [1, 14]. The BSCF membranes are often unstable at the required operating temperatures, leading to mechanical failures [6]. The LSCF with 40 % Sr and a surface activation layer have obtained an oxygen flux of 1 mL/cm^2min between 850-900 °C [12]. This type of membrane is often more stable than the BSCF, which is why it often is preferable despite its lower oxygen permeation [14]. Lemes-Rachadel et al. [15] list some asymmetrical perovskite membranes produced by different materials and processes. The thickness of the thin film varies from 10 µm to a few hundred µm. The best result was achieved by a tape casted BSFC membrane with a 70 µm thick functional layer. This membrane gave a flux of 5.04×10^{-5} $mols^{-1}cm^{-2}$ at 900 °C. The oxygen permeation fluxes reported today are still too low for practical application [1].

In a study performed by Remsen et al. [16] hexagonal $Dy_{1-x}Y_xMnO_{3+\delta}$ with space group $P6_3cm$ was synthesized. During heating, it was showed that hexagonal manganites have a fast and unusually large oxygen absorption (up to $\delta = 0.35$) at low temperatures around 200–300 °C and a rapid release of oxygen above 275–375 °C when it returns to its stoichiometric phase. During cooling the materials showed rapid uptakes of oxygen in the range of 200–350 °C. The hexagonal material also showed stability at elevated temperatures under reducing conditions [16].

Another study performed by Abughayada et al. [17], showed that the hexagonal $YMnO_{3+\delta}$ and $HoMnO_{3+\delta}$ can incorporate a large amount (up to $\delta = 0.3$) of excess oxygen at very low temperatures in the range of 190–325 °C. These results are shown in Figure 1.4. These unusually low temperatures for uptake of oxygen in hexagonal manganites occur due to the incorporation of highly mobile interstitial O_i as a defect, as opposed to oxygen vacancies in the more traditional perovskite materials. These low operating temperatures for large oxygen adsorption give the possibility of using hexagonal manganites as a membrane material for separating oxygen from air. This reduction in operating temperatures, from 800 °C to 200 °C will make oxygen separation much more environmentally friendly, and will also lessen the mechanical and chemical degradation of the membranes and increase their lifetime. These properties make hexagonal manganites good candidates for oxygen storage applications, enabling us to overcome the challenges associated with the state-of-the-art perovskites.

1.4 Aim of the study

The objective of this study is to fabricate an asymmetrical MIEC membrane for oxygen separation from air based on hexagonal manganites. The successful fabrication of this type of membrane could mean a breakthrough in the field of oxygen separation, as hexagonal manganites will lead to lower operating temperatures, a decrease in membrane degradation, longer lifetime of the membranes, and hence, will be much more environmentally friendly and economical than the current state-of-the-art perovskites.

The membrane will consist of a dense, functional thin film on a porous support. Both the thin film and the support will be made from hexagonal $YMnO_3$ for increased compatibility in order to avoid degradation and cracking of the membrane. The main goal is to obtain a dense thin film and produce a functioning membrane, as this has never before been achieved for hexagonal $YMnO_3$. Possible fabrication routes will be investigated, including deposition of the thin film by spray coating, dip coating, and drop casting, and the effect of different sintering temperatures on the density of the thin film. The $YMnO_3$ will be doped with 15% titanium at the Mn-site to avoid microcracking of the material, as Ti reduces the anisotropy of the thermal expansion coefficient in the material. The effect of yttrium deficiency on the crystal structure and sintering properties of the material will also be investigated. The oxygen adsorption and desorption of the materials will be examined by thermogravimetric analysis.

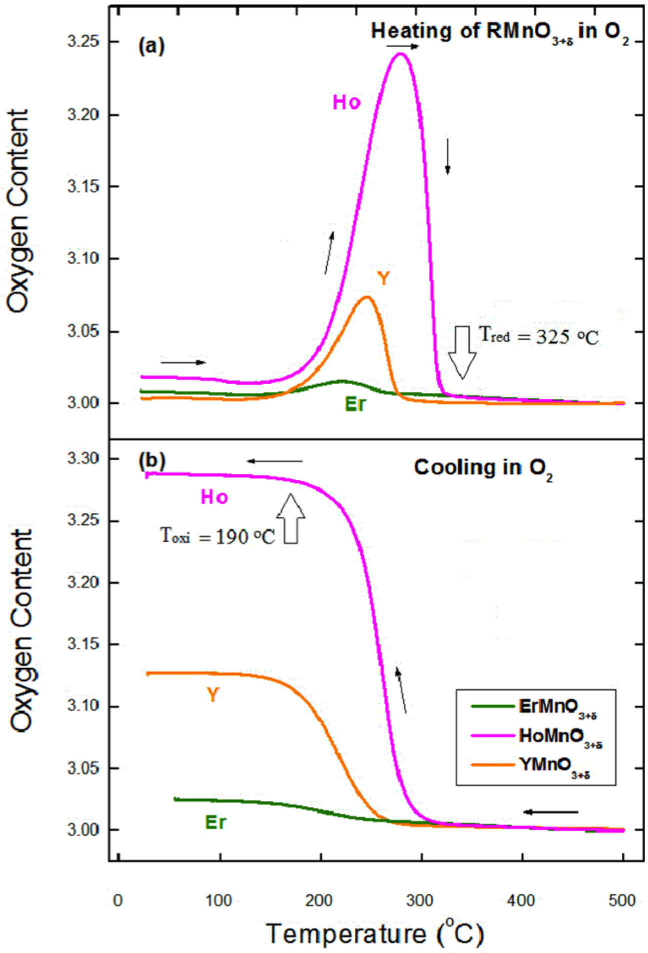

Figure 1.4: Oxygen content in $R\mathrm{MnO}_{3+\delta}$ (R =Er, Ho, and Y) upon heating (a) and cooling (b) with heating/cooling rates of 0.1 °C/min. Figure reprinted from Abughayada et al. [17].

Chapter 2

Literature review of $YMnO_3$

The hexagonal manganites RMnO$_3$, (R = Sc, Y, Eu-Lu) have received a lot of interest in the last years due to their multiferroic properties [18]. This class of hexagonal manganites can for instance be used in non-volatile memory materials, as gate ferroelectrics in field-effect transistors, as magnetic field sensors, and in ferroelectric domain walls [19, 20]. Recent research also shows promising results for use in mixed ionic-electronic conducting membranes for oxygen separation due to their large oxygen adsorption capacities [17].

2.1 Crystal structure of hexagonal $YMnO_3$

The ternary manganites RMnO$_3$, R = Sc, Y, Eu-Lu, can crystallize in either an orthorhombic perovskite structure with space group $Pbnm$, or a hexagonal structure with space group $P6_3cm$ [21]. The ground state of these manganites is the polar $P6_3cm$ symmetry [22].

The hexagonal YMnO$_3$ structure consists of Mn^{3+} that is five-coordinated by oxygen to form MnO$_5$ trigonal bipyramids that are corner-sharing in the ab-plane. The Y^{3+} is seven-coordinated by oxygen, and alternating layers of Y^{3+} and MnO$_5$ bipyramids form in the ab-plane. The MnO$_5$ bipyramids are tilted with respect to the polar c-axis and the ab-plane, by approximately 5° and 8°, respectively [22] The Y^{3+} ions are unevenly displaced along the c-axis, one third of the cations in one direction and two thirds in the opposite direction. Figure 2.1a shows the polar $P6_3cm$ phase of YMnO$_3$.

At temperatures higher than ~1250 K, hexagonal YMnO$_3$ exhibits a centrosymmetric, paraelectric state with the space group $P6_3/mmc$. This high-temperature phase has a higher degree of symmetry than the room temperature $P6_3cm$ phase, in which the Y^{3+} ions exist in centrosymmetric sites and the MnO$_5$ bipyramids are not tilted. The $P6_3/mmc$ phase with high-symmetry atomic positions in a basis of $P6_3cm$ is shown

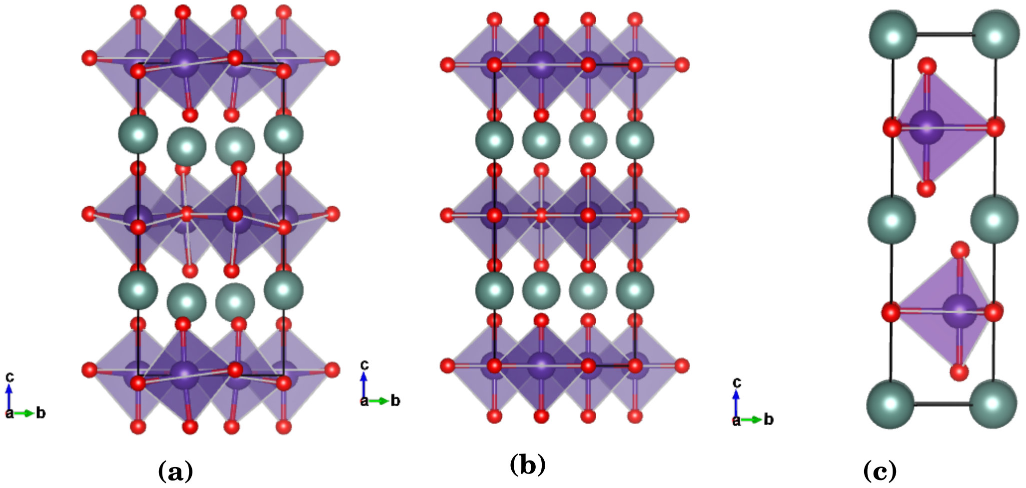

(a) (b) (c)

Figure 2.1: Hexagonal $YMnO_3$. Green spheres represent Y^{3+}, purple represent Mn^{3+}, and red represent O^{2-}. a) Room temperature phase with space group $P6_3cm$. b) High-temperature phase with space group $P6_3/mmc$, shown with high-symmetry atomic positions in a basis of $P6_3cm$. c) One unit cell of the high-temperature phase $P6_3/mmc$. All figures are made using the VESTA software [23] with atomic positions obtained from Gibbs et al. [18].

in Figure 2.1b, and one unit cell of the $P6_3/mmc$ space group is shown in Figure 2.1c. The transition between the high-temperature $P6_3/mmc$ space group and the low-temperature polar $P6_3cm$ results in a tripling of the unit cell volume. This tripling occurs due to tilting of the MnO_5 bipyramids and the displacement of the Y^{3+} ions. The correlation between the a lattice parameter in the two states is given in Equation 2.1 [18, 21].

$$a(P6_3cm) = \sqrt{3}a(P6_3/mmc) \tag{2.1}$$

There has been a lot of debate regarding the trimerization temperature of $YMnO_3$ and the onset of polarization, with a large range of reported Curie temperatures, T_C [18]. It was suggested that the transition from the low-temperature phase to the high-temperature phase involved an intermediate phase, but a recent study performed by Lilienblum et al. [24] has proven that only one transition exists. They concluded that the actual value for T_C is 1259 ± 24 K, and that it is connected to the temperature for tripling of the unit cell. The tilting of the octahedra and the displacement of the Y-ions are strongly coupled, and at room temperature they are observed together, giving a spontaneous polarization of $P_s = 5.6\ \mu C/cm^2$ [24].

2.2 Phase stability

It is possible for the hexagonal manganites $R\text{MnO}_3$ to crystallize into both the hexagonal structure with $P6_3cm$ space group and the orthorhombic perovskite structure with space group $Pbnm$. Which structure is favored is determined by the ionic radii in the material, and is expressed by the Goldschmidt tolerance factor t, shown in Equation 2.2.

$$t = \frac{r_{\text{R}^{3+}} + r_{\text{O}^{2-}}}{\sqrt{2}(r_{\text{Mn}^{3+}} + r_{\text{O}^{2-}})} \tag{2.2}$$

Here $r_{\text{R}^{3+}}$ is the ionic radius of the R cation, $r_{\text{Mn}^{3+}}$ is the ionic radius of Mn^{3+} and $r_{\text{O}^{2-}}$ is the ionic radius of O^{2-}. For a tolerance factor of 1, the structure favors an ideal cubic perovskite. The orthorhombic phase is favored for $t > 0.855$ and the hexagonal phase is favored for $t < 0.855$ [25]. The Shannon radius for seven coordinated Y^{3+} is $r_{\text{Y}^{3+}} = 0.96$ Å, for five coordinated Mn^{3+} it is $r_{\text{Mn}^{3+}} = 0.58$ Å, and for O^{2-} it is $r_{\text{O}^{2-}} = 1.42$ Å [26]. These coordination numbers are for the ions in the hexagonal phase. These radii give a tolerance factor of $t = 0.841$. Hence, the hexagonal phase is favored for YMnO_3. The tolerance factor for YMnO_3 is very close to the stability limit of the orthorhombic phase, and only a small increase would make the orthorhombic phase more stable.

Which of the two polymorphs of YMnO_3, the hexagonal or orthorhombic, is stable depends on the synthesis parameters. Oxidizing conditions and low synthesis temperature will favor the orthorhombic phase [27]. The Mn^{3+} ions can be reduced to the larger Mn^{2+} (0.83 Å for the high spin six-coordinated ion) or oxidized to the smaller Mn^{4+} (0.53 Å for six-coordinated ion). A small reduction in the size of the Mn-ions might stabilize the orthorhombic structure instead of the hexagonal structure, as the tolerance factor of the material will increase [22]. A calculated phase diagram for the $\text{MnO}_x\text{–YO}_{1.5}$ system is shown in Figure 2.2 [28]. The hexagonal phase is entropy-stabilized for temperatures above 1062 K while the orthorhombic phase is metastable for all temperatures. The hexagonal phase is considered metastable at room temperature towards Y_2O_3 and YMn_2O_5 and can be decomposed to orthorhombic YMnO_3 in oxidizing atmospheres [21].

2.3 Oxygen non-stoichiometry in YMnO_3

In a perfect crystal at 0 K, all ions are locked to their respective lattice sites. When the temperature increases, the ions start to vibrate and will cause defects in the crystal.

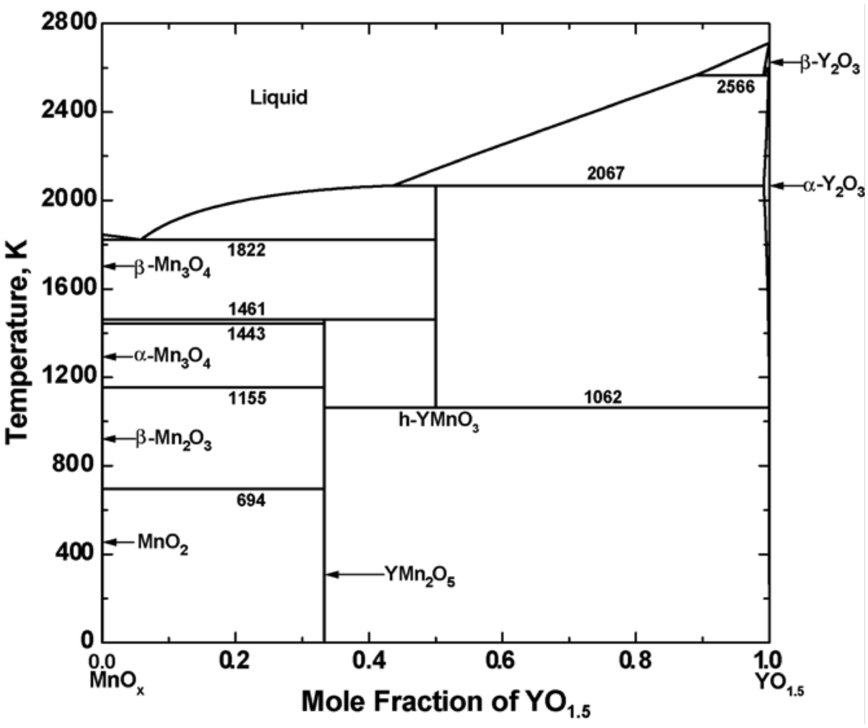

Figure 2.2: Calculated phase diagram of the MnO_x–$YO_{1.5}$ system in air. Reprinted from Chen et al. [28].

For a material to be used as a membrane, it must be able to incorporate static and moving defects. The ionic conductivity of a material is dependent on the mobility of such defects. Defects can be divided into stoichiometric defects and non-stoichiometric defects. Stoichiometric defects leave the crystal composition unchanged and is also referred to as intrinsic defects. Non-stoichiometric defects, or extrinsic defects, occur by introducing foreign atoms into the structure and consequently alters the composition of the crystal [29]. Point defects can be a cation or anion vacancy or interstitial, and must be charge compensated in some way. The intrinsic Schottky and Frenkel point defects involve a vacancy pair and a vacancy/interstitial pair, respectively, and are thus charge compensated. Extrinsic point defects can be introduced either by doping with a foreign ion, or by interaction between the crystal and its surroundings. For example, interstitial oxygen can be incorporated into the crystal from the atmosphere, and can be charge compensated by oxidation of the surrounding ions in the lattice.

Hexagonal $YMnO_3$ is 11% less densely packed than the perovskite structure, and can therefore incorporate highly mobile interstitial oxygen as a point defect without the creation of cation vacancies [30]. This can explain the low-temperature excess of oxygen reported in literature [16, 17]. The oxygen exchange between the lattice and the atmosphere can be described by Equation 2.3, and in Kröger-Vink notation by Equation 2.4, where $Mn_{Mn}^{\bullet}$ is Mn^{4+}. Incorporation of oxygen must be charge compensated, which can be done either by oxidation of surrounding ions, by the formation of oxygen vacancies, or by doping the material with a higher-valent ion. When charge compensation occurs by oxidizing surrounding ions, two Mn^{3+} ions will be oxidized to Mn^{4+} per interstitial oxygen. This results in p-type conductivity in the material as explained by Equation 2.5. The Seebeck coefficient of hexagonal $YMnO_3$ has been measured to be positive due to mobile holes, which suggests interstitial oxygen as the main point defect and oxidation of Mn^{3+} as the charge compensating reaction [30].

$$\mathrm{YMnO_3} + \delta/2\mathrm{O_2(g)} \longrightarrow \mathrm{YMnO_{3+\delta}} \tag{2.3}$$

$$\delta/2\,\mathrm{O_2(g)} + 2\,\delta\,\mathrm{Mn_{Mn}^{\times}} \xrightleftharpoons{\mathrm{YMnO_3}} \delta\,\mathrm{O_i''} + 2\,\delta\,\mathrm{Mn_{Mn}^{\bullet}} \tag{2.4}$$

$$\mathrm{Mn_{Mn}^{\bullet}} \rightleftharpoons \mathrm{h^{\bullet}} + \mathrm{Mn_{Mn}^{\times}} \tag{2.5}$$

The concentration of interstitial oxygen is favored up to a certain temperature. This can be explained by the Gibbs free energy, ΔG, as shown in Equation 2.6.

$$\Delta G = \Delta H - T\Delta S \tag{2.6}$$

The incorporation of oxygen from the atmosphere to the lattice, as shown in Equation 2.3, will lead to a negative entropy, ΔS. The contribution of ΔS to Gibbs energy is therefore positive. DFT calculations of the enthalpy, ΔH, at 0 K have shown that the enthalpy of the reaction in Equation 2.3 is negative [30], and hence ΔG will be negative. This means that the reaction occurs spontaneously towards the right at low temperatures. As the temperature increases, the $-T\Delta S$ part of the equation will become more dominant and ΔG will become less negative and eventually positive. This shifts the reaction in Equation 2.3 towards the left hand side, making the interstitial ions leave the lattice at high temperatures [30].

The formation of oxygen vacancies in $YMnO_3$ can be described by Equation 2.7, and by Kröger-Vink notation in Equation 2.8, where Mn_{Mn}' is Mn^{2+} and high spin d^5. Equation 2.9 shows the reduction of Mn^{3+} which occurs when the oxygen content in the lattice decreases. This reduction fills the highest energy orbital $3d_{z^2}$ which is located along the *c*-axis, and leads to an increase in electrostatic repulsion along this axis and a concomitant chemical expansion of the lattice.

$$YMnO_3 \longrightarrow YMnO_{3-\delta} + \delta/2O_2(g) \tag{2.7}$$

$$2\,\delta\,Mn_{Mn}^{\times} + \delta O_O^{\times} \xrightleftharpoons{YMnO3} 2\,\delta\,Mn_{Mn}' + \delta V_O^{\bullet\bullet} + \delta/2\,O_2(g) \tag{2.8}$$

$$Mn_{Mn}' \rightleftharpoons e' + Mn_{Mn}^{\times} \tag{2.9}$$

2.4 Microcracking in $YMnO_3$

The fabrication temperature for $YMnO_3$ is above the temperature for unit cell tripling, and during cooling the material undergoes a transition from the high-temperature $P6_3/mmc$ phase to the low-temperature $P6_3cm$ phase. This phase change can result in microcracking and mechanical weakening of the material.

Microcracking in a ceramic mainly occurs due to internal stresses in the material caused by either a structural phase transition involving large changes in unit cell volume, large isotropic or anisotropic thermal expansion coefficients in the material, or chemical expansion, where the unit cell volume changes due to valence state changes in the transition metal [31, 32]. Thermal expansion is a linear change in dimensions due to an increase in temperature, and a ceramic with large isotropic or anisotropic thermal expansion coefficients can obtain microcracks during heating or cooling [31]. Microcracking can cause the material to lose its mechanical integrity and become frail.

The lattice parameters in hexagonal $YMnO_3$ have large anisotropic thermal and chemical expansion coefficients [21, 32]. In a study performed by Selbach et al. [21], the changes in lattice parameters in $HoMnO_3$ and $YMnO_3$ were investigated as a function of temperature in air and nitrogen atmospheres, and also in oxygen for $YMnO_3$. These results are shown in Figure 2.3 for $HoMnO_3$ to the left and for $YMnO_3$ to the right. For $HoMnO_3$, the *c* parameter decreases until it reaches the temperature for unit cell tripling at approximately 1400 K, where it is stable for about 100 K and then starts to increase. This trend is the same in both air and nitrogen atmosphere, but for nitrogen the decrease and subsequent increase is shifted to slightly lower temperatures.

For $YMnO_3$ the same trend can be observed up to between 1300–1400 K, where the measurements stop. The a parameter increases linearly with temperature for both $HoMnO_3$ and $YMnO_3$, and is slightly larger in nitrogen atmosphere than in air. Since the processing temperatures for $YMnO_3$ for use in an MIEC membrane are from 1300 °C and above, the anisotropic expansion of the lattice parameters can cause microcracking in the material during cooling. A method for decreasing the anisotropy of the material is therefore necessary in order to ensure that the mechanical strength of the material is sufficient for use as an oxygen permeable membrane.

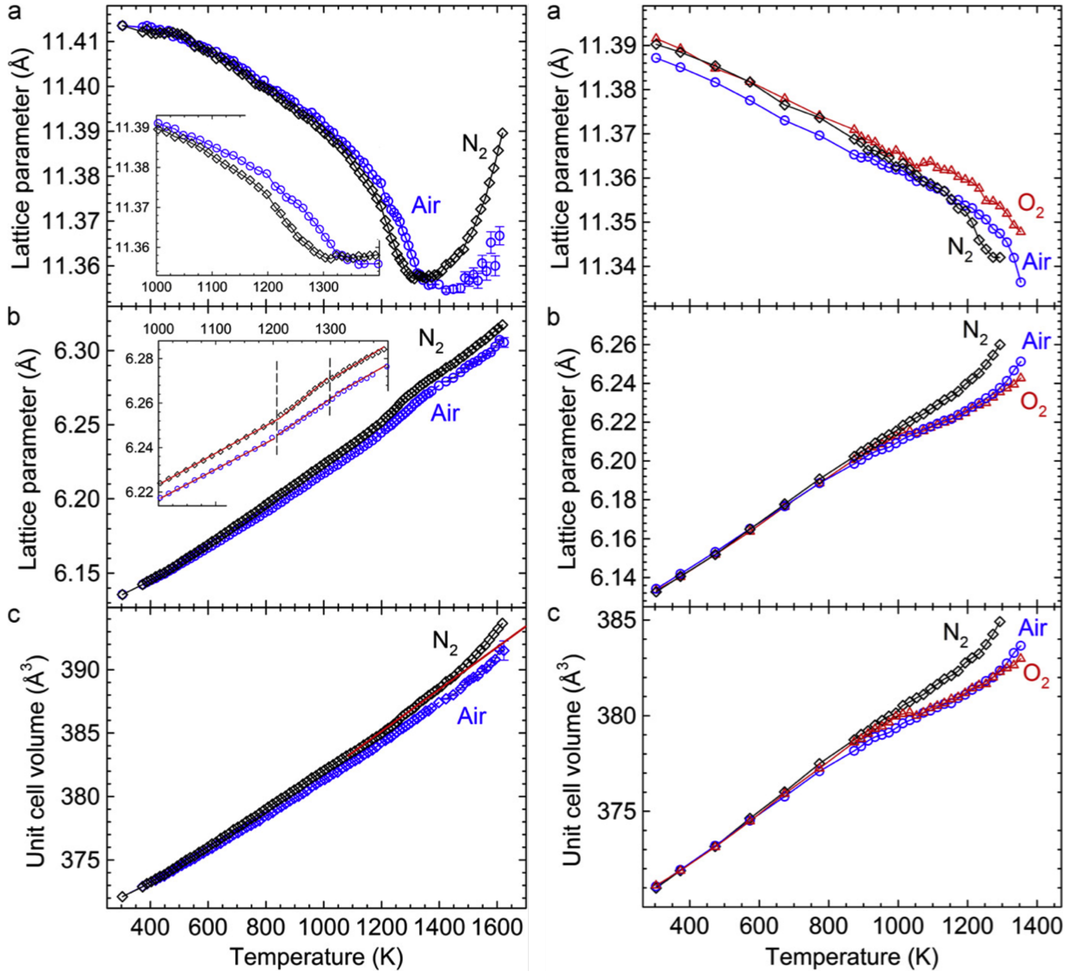

Figure 2.3: Changes in lattice parameter c (a), lattice parameter a (b), and unit cell volume (c), for $HoMnO_3$ (left) in air and N_2 atmosphere and $YMnO_3$ (right) in air, O_2 and N_2 atmosphere. Reprinted from Selbach et al. [21].

2.5 Ti-doping of $YMnO_3$

Reducing the stresses that cause microcracking in a ceramic can be obtained by doping the material. Tomczyk et al. [33] investigated the effect of Ti-doping on the expansion of the lattice parameters in $YMnO_3$. The amount of titanium varied in the range of $x = 0.00 - 0.25$, resulting in $YMn_{1-x}Ti_xO_3$. Ti-doping will eventually cause a hexagonal-to-rhombohedral phase transition. Figure 2.4a shows the results from X-ray diffraction of $YMn_{1-x}Ti_xO_3$ obtained by Tomczyk. For Ti concentrations between $0 < x < 0.175$ the structure exhibits a hexagonal structure, while for $x > 0.175$ superstructure reflections are observed that correspond to the rhombohedral space group $R3c$. For $x = 0.15$ the Ti has stabilized the high-temperature $P6_3/mmc$ structure, as can be seen by the disappearance of the reflections at 23° 2θ and 36° 2θ. These results are in accordance with results reported by Asaka et al. [34]. The stabilization of the $P6_3/mmc$ phase at room temperature will prevent the unit cell tripling that normally occurs during cooling and causes microcracking.

The effect of the various titanium doping concentrations on the a and c hexagonal lattice parameters found by Tomczyk et al. can be seen in Figure 2.4b. The c parameter decreases with increasing Ti content, and the a parameter increases, meaning that the anisotropy of the lattice parameters and the c/a ratio decreases. This is thought to decrease the internal stresses in the material during phase transition, and reduce the thermal expansion hysteresis during heating and cooling [33]. Based on these results, a doping concentration of 15% Ti on Mn-site was chosen for this work.

2.6 Synthesis method

In this study, several techniques were used in order to fabricate the asymmetrical membrane. Solid state synthesis was chosen to produce the porous membrane, citric acid synthesis was used to produce nanoparticles, and spray coating, dip coating and drop casting were used to apply the dense thin film of nanoparticles on top of the substrate. The sintering properties of the material were also investigated.

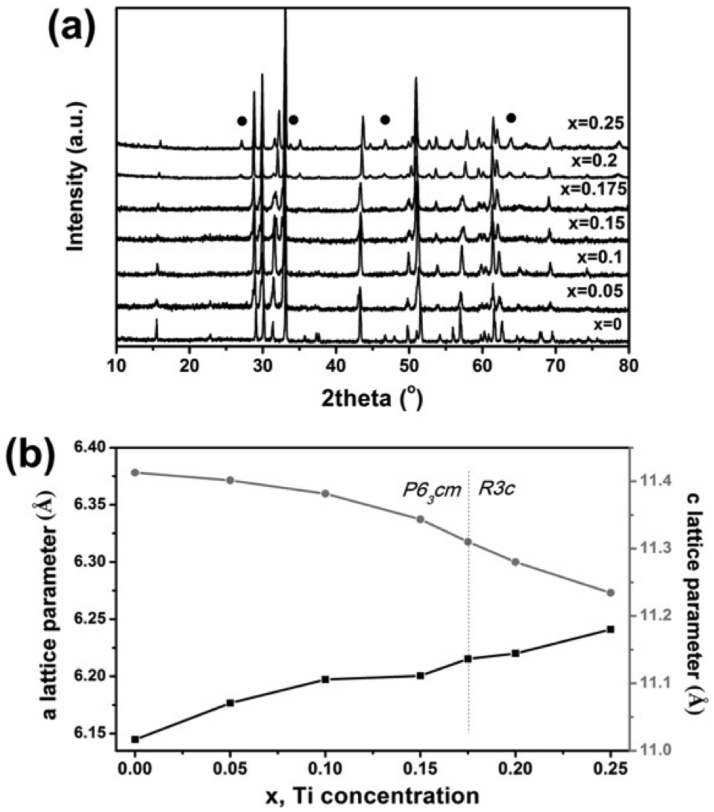

Figure 2.4: (a) The X-ray diffraction patterns of $YMn_{1\text{-}x}Ti_xO_3$. The dots mark the peaks associated with the rhombohedral $R3c$ phase. (b) The dependence of lattice parameters a and c on Ti-concentration in $YMn_{1\text{-}x}Ti_xO_3$. Reprinted from Tomczyk et al. [33].

2.6.1 Solid state synthesis

Solid state synthesis is one of the most common and simplest ways of producing ceramic materials. It was chosen as fabrication method for the porous support in this study due to its simplicity and easy control of stoichiometry. It is also ideal for making a porous microstructure. The solid state method involves mixing binary, non-volatile oxides in stoichiometric amounts and mixing them together in a mortar and pestle. The precursors have to be mixed thoroughly to achieve a uniform and small particle size, before they are heated at high temperature for several hours [35]. The reaction to form the product occurs by the diffusion of ions through the bulk and to the interface between particles where the ions react to form the product [2]. A schematic of the solid state reaction is shown in Figure 2.5.

The diffusion of ions in the bulk is normally slow, and high temperatures, usually in the range of 500–2000 °C, are therefore required. The temperatures need to be high enough

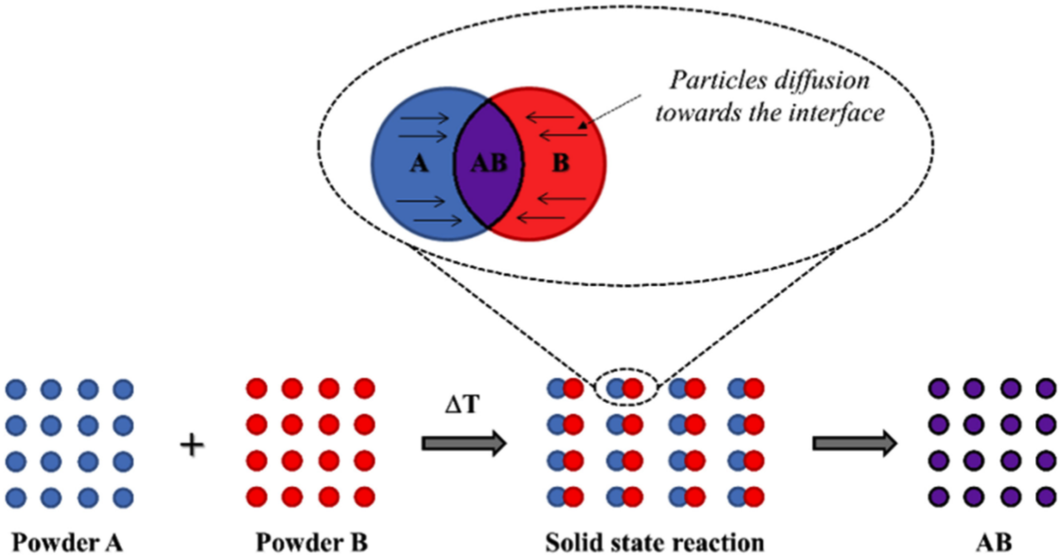

Figure 2.5: An illustration of the solid state reaction. The figure is reprinted from Athayde et al. [2].

to overcome the lattice energy and allow the ions to move to different lattice sites [35]. Since the reaction between the precursors only happens at the interface between the particles, it is important to increase the surface area as much as possible to minimize the diffusion distance of the ions [29]. Increasing the temperature will also increase the diffusion rate and make the reaction faster. The firing step is usually between 8–24 hours long at high temperatures [2]. Prior to firing of the precursors, the powders are often pressed together to increase contact area between the particles.

Despite its widespread use, the solid state method has its limitations. One common problem is that the product is often not homogeneous after just one firing, and the sample has to be ground and fired again. Another problem is contamination from containers during heating. Al_2O_3 is a suitable container material, as it is inert, however, contamination might still occur [29]. To avoid contamination, the prepared samples are often placed on top of some sacrificial powder prior to firing. Applying a special atmosphere during firing might also affect the product. Inert gas atmospheres, such as argon and nitrogen, will prevent oxidation to higher valency, while oxygen atmosphere will favor higher oxidation states [35].

2.6.2 Citric acid method

In order to produce nanocrystalline $YMn_{0.85}Ti_{0.15}O_3$, the citric acid method was chosen as the best process for obtaining a correct composition and stoichiometry. The resulting powder usually has a small particle size in the nanometer range. The citric acid method is a wet-chemical, sol-gel process, where a precursor solution containing all the reactant cations is dried and transformed into a homogeneous, amorphous gel. The gel is then calcined to form the crystalline powders [29]. Citric acid is added to the precursor solution as a chelating agent to prevent the metal cations from partially segregating in the final product. The ratio between metal ions and chelating agent must be precisely controlled. Ethylene glycol is added as a polymerization agent, and, together with heating to 150–250 °C, causes polyesterification of the chelates [2]. Further heating to 400 °C removes excess water and chars the resin. The temperature is increased to 500–900 °C and crystalline powder in the range 20–50 nm forms and clusters into agglomerates [36]. The synthesis parameters used in this study were obtained from Bergum et al. [22] who successfully produced nanocrystalline $YMnO_3$.

2.6.3 Sintering

In order to form a dense film from deposited nanoparticles, the particles must be sintered. Solid state sintering is a densification method that removes the pores in a material through volume diffusion when high temperatures are applied. The diffusion can occur due to movement of atoms or vacancies along the particle surfaces. The sintering process occurs in three main stages. In the first stage, the particles rearrange and start to join together, a process called necking. The second stage involves neck growth and grain growth, a process which usually leads to the reduction in pore size and shrinking of the material. During this phase of sintering, the pores are continuous. Finally, if sintering is allowed to continue, the grains become even larger, the pores become closed, and eventually the grain boundary pores will be eliminated [36]. The driving force for sintering is reduction of the total surface area and the related surface energy [37]. The mechanism of material transport by lattice diffusion can be described by Equation 2.10.

$$\frac{\Delta L}{L_0} = \left(\frac{K \gamma a^3 D^* t}{k T d^n} \right)^m \tag{2.10}$$

Here $\Delta L / L_0$ is the linear shrinkage of the material, which is equivalent to the rate of sintering. γ is the surface energy, a^3 is the atomic volume of the diffusing vacancy, D^* is the self diffusion coefficient, k is the Boltzmann constant, T is temperature, d is particle diameter, t is time, and K is a geometry-dependent constant. The exponents n and m are usually close to 3 and between 0.3–0.5, respectively [36]. From this equation it is clear that the sintering of a material is dependent on many parameters. For example, the temperature at which sintering occurs, is very important to control, but the time spent at the sintering temperature is less important.

Finer-sized material will lead to an increased sintering rate and is very important to control. Small particles can also be sintered at lower temperatures than larger-sized particles. The material should also have a narrow particle size distribution, since a closer packing of the material will increase the contact between particles and make the diffusion distance shorter. Particles of very different sizes will lead to pores being trapped in the material. In order to achieve maximum removal of pores, the grain growth must also be controlled. If grains grow too rapidly, pores can be trapped along grain boundaries, since the diffusion mechanism occurs along the surface of the particles. Too rapid shrinkage can occur when the heating/cooling rate is too large. This might cause cracking in the material and it can lose its mechanical integrity. [36]

Chapter 3

Experimental

In this chapter, the experimental procedures used in this study are described. The methods used for analysis are also presented as well as information about the chemicals that were used.

3.1 Chemicals

Table 3.1 presents a complete list of all the chemicals that have been used in the experimental procedure of this study.

Table 3.1: The chemicals used for fabrication of the asymmetrical membrane.

Chemical	Molecular formula	Purity	Supplier
Yttrium(III) oxide	Y_2O_3	99.99%	Aldrich
Manganese(III) oxide	Mn_2O_3	99%	Aldrich
Titanium(IV) oxide	TiO_2, (anatase)	99.8%	Aldrich
Holmium(III) oxide	Ho_2O_3	99.9%	Aldrich
Yttrium(III) acetate hydrate	$Y(CH_3CO_2)_3 \cdot xH_2O$	99.9%	Aldrich
Manganese(II) carbonate, hygroscopic	$Mn(CO_3)$	≥99.9%	Aldrich
Titanium(IV) isopropoxide	$Ti(OCH(CH_3)_2)_4$	97%	Aldrich
Citric acid	$C_6H_8O_7$	99%	Sigma-Aldrich
Ethanol absolute	C_2H_6O	99.8%	VWR Chemicals
Ethylene glycol	$C_2H_6O_2$	≥99.5%	Merck

3.2 Preparation of porous supports

The solid state method was used to manufacture the porous support for the asymmetrical membrane. $YMnO_3$ doped with 15% Ti was chosen as the optimal composition for the intended application, due to the advantages of Ti-doping described in Section 2.5. 5% of the yttrium was replaced by holmium to distinguish the support from the film by energy-dispersive X-ray spectroscopy (EDS), without changing the crystal structure of the support. In addition, samples with varying amount of Y-deficiency were made in order to determine the effect of Y-deficiency on the sintering properties and on oxygen adsorption and desorption of the material. The composition and abbreviation of all the samples produced by the solid state method are given in Table 3.2.

Table 3.2: Composition and abbreviation of the samples prepared by solid state synthesis.

Composition	**Abbreviation**
$Y_{0.95}Ho_{0.05}Mn_{0.85}Ti_{0.15}O_3$	YHMTO
$YMn_{0.85}Ti_{0.15}O_3$	YMTO
$Y_{0.95}Mn_{0.85}Ti_{0.15}O_3$	Y95MTO
$Y_{0.90}Mn_{0.85}Ti_{0.15}O_3$	Y90MTO
$Y_{0.85}Mn_{0.85}Ti_{0.15}O_3$	Y85MTO

The precursors for the solid state synthesis were the binary oxides Y_2O_3, Mn_2O_3, TiO_2, and Ho_2O_3. Stoichiometric amounts of precursors were mixed together with a small amount of ethanol using a mortar and pestle until a homogeneous mix was reached. Pellets were pressed from the resulting mixture using a double action uniaxial pressing tool and a pressure of approximately 40 MPa. The pellets were placed on an alumina disk on top of sacrificial powder to avoid direct contact with the alumina disk. The pellets were fired in a clean oven for 12 hours using the temperature program shown in Figure 3.1.

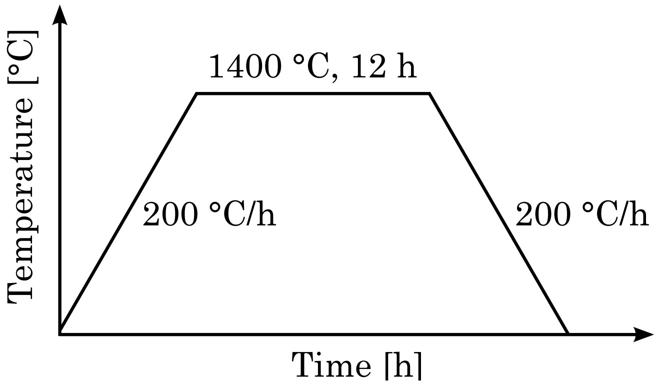

Figure 3.1: The temperature program used for annealing the $Y_{0.95}Ho_{0.05}Mn_{0.85}Ti_{0.15}O_3$ pellets and the $Y_{1\text{-}x}Mn_{0.85}Ti_{0.15}O_3$ pellets, where x=0, 0.05, 0.10 and 0.15.

3.3 Preparation of nanocrystalline powder for the thin film

3.3.1 Preparation of precursors

Prior to fabrication of the nanocrystalline $YMn_{0.85}Ti_{0.15}O_3$ needed for the thin film, precursors containing the ions Y^{3+}, Mn^{3+}, and Ti^{4+} had to be prepared. The precursors were made by dissolving each of the salts yttrium(III)acetate hydrate, manganese(III)carbonate hydrate, and titanium(IV) isopropoxide (TTIP) in distilled water mixed with different amounts of citric acid. The molar ratios between the citric acid and the ions were chosen based on the work done by Bergum et al. [22] and Frydenlund [38].

The precursor containing Y^{3+} was made by mixing $Y(O_2C_2H_3)_3 \cdot xH_2O$, citric acid and 0.7 L distilled water in an Erlenmeyer flask and heating the mixture on a hotplate at 150 °C. The solution was stirred by a magnet at 440 rpm for 4 hours until the solution was completely transparent. The molar ratio between the Y^{3+} and the citric acid was 1:15.

The Mn^{3+} precursor was made by adding $Mn(CO_3) \cdot xH_2O$ and citric acid to an Erlenmeyer flask along with 0.7 L distilled water. The solution was stirred on a hotplate for 3 hours at 150 °C and 480 rpm until the solution was transparent. The molar ratio between the Mn^{3+} ions and the citric acid was 1:22.

The Ti^{4+} precursor was prepared by mixing 6.661 g citric acid and 0.14 L distilled water in an Erlenmeyer flask. The solution was heated on a hotplate to 60 °C and stirred at 440 rpm. TTIP was added to the solution by extracting 1.56 mL from its bottle using a 5 mL syringe. A tight rubber tube connected a glass tube to the syringe and argon was flushed on to the syringe in order to avoid hydrolization of TTIP. Argon was flushed to the tip of the syringe continuously during transfer from the TTIP bottle to the solution. Some of the TTIP hydrolyzed when it came in contact with the solution, but after being heated and stirred for 24 hours the solution became transparent. The molar ratio between the Ti^{4+} and the citric acid was 1:6.3.

The precursors had to be standardized in order to find the molality of the solutions. Porcelain crucibles with Kaowool as lid were fired prior to standardization in order to burn off any organic material and impurities that might be attached to them. They were fired at 1000 °C for one hour and then weighed. The precursor solutions were added to the crucibles and weighed. Four crucibles were used for each of the precursors, and they were transported and stored in a dessicator between each weighing. The crucibles were fired at temperatures that would produce the oxides Y_2O_3, Mn_2O_3, and TiO_2 from each precursor, and the crucibles were weighed again after being fired. The temperature programs for standardization of the Y^{3+}, Mn^{3+}, and Ti^{4+} precursors are shown in Figure 3.2, Figure 3.3, and Figure 3.4, respectively. The oxides were analyzed with X-ray diffraction in order to ensure that the correct oxides had been formed.

The molalities of the solutions were calculated based on the amount of oxide produced during firing. The crucible with the largest deviation was excluded from the calculations for all three precursors. Molality calculations based on the three best crucibles are shown in Appendix A. The molalities of the precursors with standard deviations are shown in Table 3.3. The coefficient of variation is less than 4% for all three precursors.

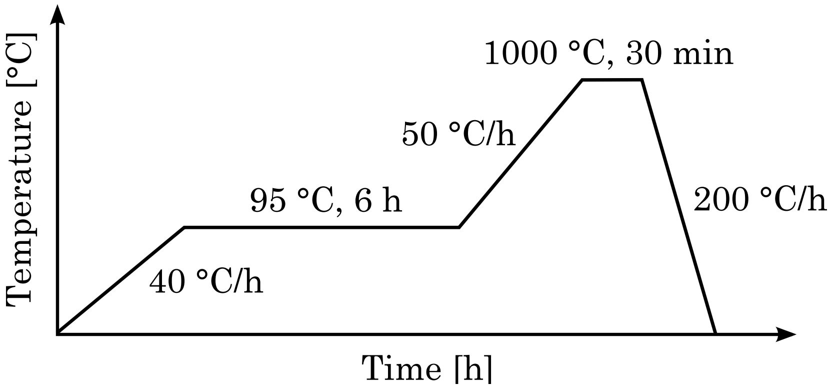

Figure 3.2: The temperature program used for standardization of the Y^{3+} precursor.

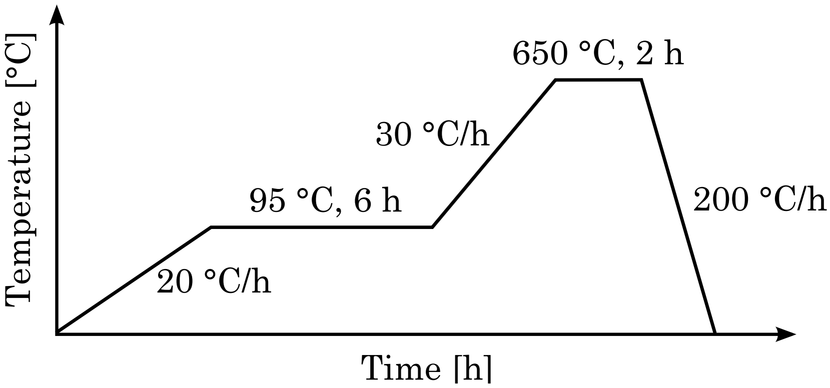

Figure 3.3: The temperature program used for standardization of the Mn^{3+} precursor.

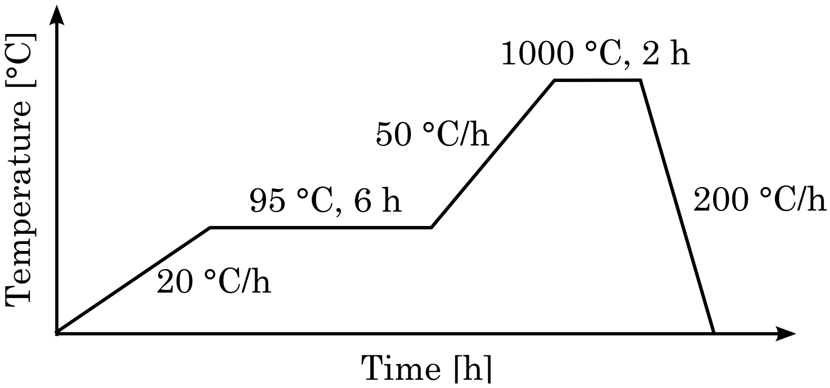

Figure 3.4: The temperature program used for standardization of the Ti^{4+} precursor.

Table 3.3: Calculated molality of the precursors used for making nanocrystalline $YMn_{0.85}Ti_{0.15}O_3$ with the corresponding standard deviation.

Precursor	**Molality [mmol/g]**
Y^{3+}	0.0417 ± 0.0013
Mn^{3+}	0.0328 ± 0.0006
Ti^{4+}	0.0761 ± 0.0029

3.3.2 Citric acid synthesis

The nanocrystalline powder used for the thin film of the membrane was made by a modified citric acid method. Figure 3.5 shows a flow chart of the synthesis route. The precursors containing the Y^{3+}, Mn^{3+}, and Ti^{4+} ions were mixed in a beaker in stoichiometric amounts along with ethylene glycol. The molar ratio between ethylene glycol and citric acid in the precursors was 1:1. The solution was heated on a hotplate at 150 °C for 24 hours and stirred by a magnet at approximately 400 rpm. The solution turned into a gel and was placed in a drying cabinet for one day at 115 °C. The contents of the solution forming the gel is shown in Table 3.4. The gel was calcined in order to make the raw powder for nanocrystalline $YMn_{0.85}Ti_{0.15}O_3$. The temperature programs for the calcination and the subsequent heat treatment to obtain $YMn_{0.85}Ti_{0.15}O_3$ is shown in Figure 3.6 and Figure 3.7, respectively. After the heat treatment the powder was mortared and sieved to < 150 µm.

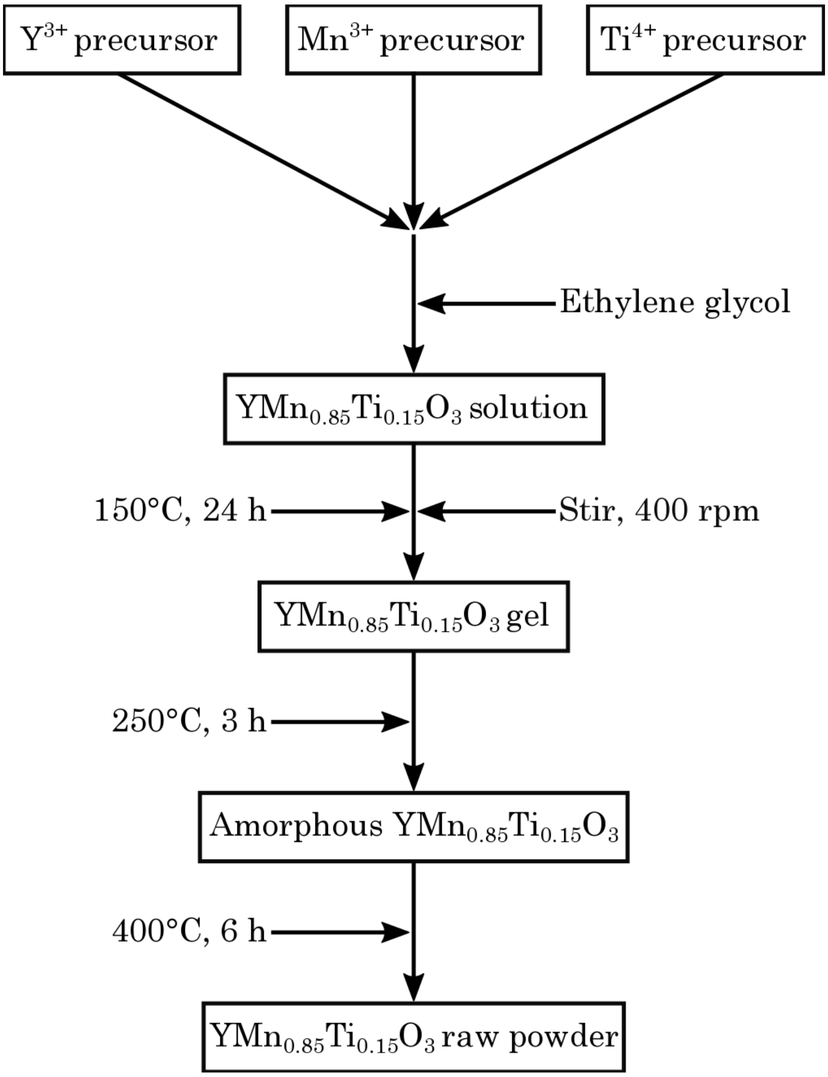

Figure 3.5: The citric acid synthesis route to obtain the raw powder for nanocrystalline $YMn_{0.85}Ti_{0.15}O_3$.

Some nanocrystalline powder produced for previous work [39] was used for analysis of sintering properties and oxygen adsorption and desorption in $YMn_{0.85}Ti_{0.15}O_3$. The fabrication procedure was the same as the one described above. This powder was also used to make the first four suspensions for deposition of the thin film onto porous

Table 3.4: Contents of solution forming 5 g of nanocrystalline $YMn_{0.85}Ti_{0.15}O_3$ powder. The amount of citric acid given is the total amount of citric acid in the precursors. The first row give the contents in moles, and the second row in grams.

Y^{3+} precursor	Mn^{3+} precursor	Ti^{4+} precursor	Citric acid	Ethylene glycol	Amount of $YMn_{0.85}Ti_{0.15}O_3$
0.0262 mol	0.0223 mol	0.0039 mol	0.9080 mol	0.9080 mol	0.0262 mol
628.489 g	679.171 g	51.658 g	174.443 g	56.356 g	5 g

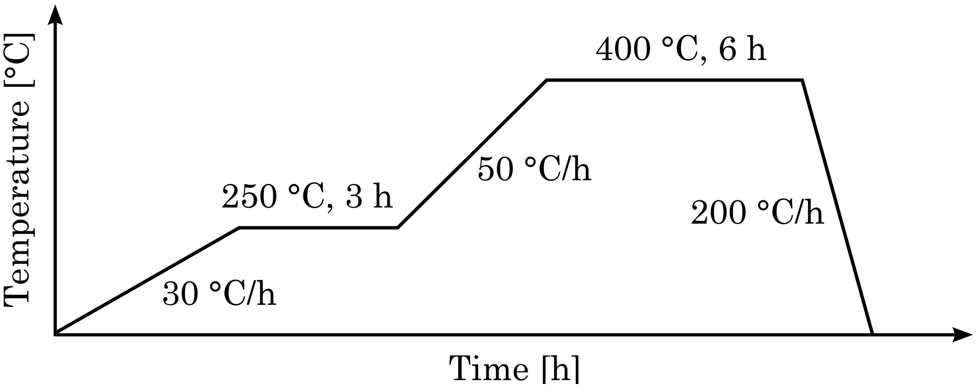

Figure 3.6: The temperature program for calcining of the gel to obtain the raw powder for nanocrystalline $YMn_{0.85}Ti_{0.15}O_3$.

substrates. Before the powder was used and analyzed it was fired a second time at 900 °C in order to make it more crystalline. It was heated and cooled rapidly at 200 °C/min and held at 900 °C for just one minute in order to minimize particle growth. The particles agglomerated during heat treatment, and the powder was therefore mortared and sieved to < 150 µm. For simplicity, the nanocrystalline powder produced in this work will be named N1(800), while the powder from previous work will be named N2(800) and N2(900) for firing at 800 and 900 °C, respectively.

3.4 Preparation of the asymmetrical membrane

In order to get a functioning membrane, the nanoparticles had to be suspended in a solution and deposited onto the porous support in a manner that would result in a dense thin film. Various deposition methods were tested. These were spray coating, dip coating and drop casting. The effect of the solid load in the suspension and sintering temperature was also investigated.

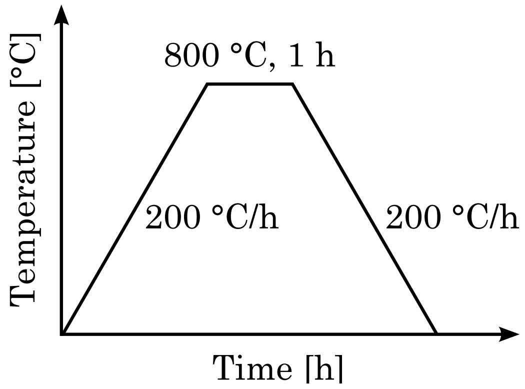

Figure 3.7: The temperature program for heat treatment of the $YMn_{0.85}Ti_{0.15}O_3$ raw powder in order to obtain hexagonal $YMn_{0.85}Ti_{0.15}O_3$.

All of the deposition methods that were tested were chosen due to their simple deposition process. In addition, spray coating gives a good control of layer thickness and a large area coverage. Dip coating also gives a large area coverage and the ability to make very thin layers. Drop casting can also control the layer thickness.

The pellets produced by the solid state method were prepared for deposition of the thin film by grinding and polishing in order to achieve a smooth and even surface. Grinding was done by wet grinding on a Struers LaboPol-21 with SiC paper of grades #320, #500, #800, and #1200 at 250 rpm. Polishing was done on a Struers Tegramin-20 with polishing disks of 9 µm and 3 µm polishing grade.

3.4.1 Suspensions

Suspensions of nanoparticles in ethanol were made for deposition of a thin film onto the porous substrates. Several suspensions were made in order to test the effect of the suspension on the resulting thin film. The first four suspensions were made using the $YMn_{0.85}Ti_{0.15}O_3$ nanoparticles fired at 900 °C, N2(900), and the rest was made using the $YMn_{0.85}Ti_{0.15}O_3$ nanoparticles N1(800). The particles were weighed out and added to a glass bottle along with reagent grade ethanol. The amount of solid load in each suspension was chosen so that the amount of finished suspension would be enough for the relevant deposition method. The contents of the different suspensions can be seen in Table 3.5. The suspensions were agitated in an ultrasonic bath for one hour in order to get an even distribution of particles throughout the liquid. Approximately two minutes after agitation, the larger particles started to settle at the bottom of the sample container.

Table 3.5: Contents of suspensions made from nanocrystalline $YMn_{0.85}Ti_{0.15}O_3$.

Suspension	Solid content [g]	Ethanol [mL]	Solid load [vol%]
1	0.5	5.59	2.0
2	0.2	4.52	1.0
3	0.2	9.08	0.5
4	0.2	13.00	0.35
5	0.2	18.21	0.25
6	0.5	15.10	0.75
7	0.1	15.19	0.15

3.4.2 Spray coating

For fabrication of the thin film by spray coating, suspension 1 with 2 vol% solid load was deposited on a pellet with the composition $Y_{0.95}Ho_{0.05}Mn_{0.85}Ti_{0.15}O_3$. The suspension was ultrasonified for one hour directly prior to spraying to ensure an even distribution of particles. Since the particles settled quickly, the suspension was also ultrasonified continuously during deposition.

An Aztek air brush was used for deposition with a 0.7 mm nozzle and an argon flow of 0.7 bar. The pellet was sprayed from a distance of approximately 10 cm, and was allowed to dry for 10 seconds between each layer. During this time, freshly ultrasonified suspension was added to the airbrush. A total of 20 layers and 6 mL suspension was sprayed onto the pellet. The pellet was left to dry for 30 minutes before it was sintered at 1300 °C for one hour.

3.4.3 Dip coating

Dip coating was used to deposit a thin film onto two YHMTO pellets and one Y090MTO pellet. One YHMTO pellet was dipped in the suspension with 1.0 vol% solid load, and the other YHMTO pellet was dipped in the 0.25 vol% suspension. The Y090MTO pellet was dipped in the 0.5 vol% suspension. The suspensions were ultrasonified for one hour prior to deposition. Liquid latex was used to glue the pellets onto glass plates, and also to cover the sides of the pellets so that only the top surface would be exposed to the suspension. Once the latex was dry, the pellets were dipped in the suspensions for 10 seconds, and left to dry for one hour. The membranes dipped in 1.0 vol% and 0.5 vol%

suspensions, respectively, were sintered in a clean oven at 1300 °C for one hour, while the membrane dipped in the 0.25 vol% suspension was sintered at 1400 °C for one hour.

3.4.4 Drop casting

Drop casting was used to deposit a thin film onto five YHMTO pellets, one Y095MTO pellet, and one Y085MTO pellet. The suspension with 0.35 vol% solid load was deposited on one YHMTO pellet, the 0.75 vol% suspension was deposited on two YHMTO pellets, and the remaining two YHMTO pellets were drop casted with the 0.15 vol% suspension. The suspension with 0.25 vol% was deposited on both the Y095MTO and Y085MTO pellets. Prior to deposition, the pellets were immersed in reagent grade ethanol and put in the ultrasonic bath for 15 minutes. This was done in order to fill the pores with ethanol prior to drop casting to prevent the suspensions from entering the substrates during deposition.

Directly before deposition, the suspensions were shaken for one minute and left to settle. After some time, the largest agglomerates had settled to the bottom of the sample container. The 0.35 vol% suspension was left to settle for two minutes, and the 0.15, 0.25 and 0.75 vol% suspensions were left for 5 minutes. The top of each suspension was transferred to a separate container, leaving the largest agglomerates at the bottom. This procedure of settling and transferring was repeated twice in order to exclude the largest agglomerates from the suspensions and achieve a denser packing of the deposited particles. After transferring, the 0.15, 0.35 and 0.75 vol% suspensions had a dark brown color. The 0.25 vol% suspension was visibly lighter than the rest, with a light brown color, suggesting that more particles had been left out of the final suspension.

The pellets were placed on a hotplate at 100 °C and the respective suspension were dripped on top of the pellets using a pipette as soon as the surfaces of the pellets were dry. After approximately five seconds, as soon as the surfaces started to dry again, another drop was added. The pellets were rotated between each drop in order to prevent directional drying. The suspensions were agitated throughout the procedure to ensure an even distribution of particles. Approximately 11 mL of the 0.35 vol% suspension was deposited on one YHMTO pellet, 6 mL of the 0.25 vol% suspension was deposited on each of the Y095MTO and Y085MTO pellets, and 1 mL of the 0.15 and 0.75 vol% was used on each of the remaining YHMTO pellets. When depositing the 0.15 and the 0.75 vol% suspensions, a thick, uneven layer could be seen forming at an early stage, which is why only 1 mL was deposited on these pellets. After the final deposition, the thin film on the Y095MTO pellet was compressed with a uniaxial pressing tool and a pressure of approximately 2 MPa for 30 seconds. This was done to try to obtain a denser packing of the particles prior to sintering. All pellets were left to dry for 30 minutes before they were sintered. The pellet drop casted with 0.35 vol% suspension was sintered at 1300 °C. Both of the pellets drop casted with the 0.25 vol% suspension, one of the pellets drop casted with the 0.15 vol% suspension, and one of the pellets drop casted with the 0.75 vol% suspension were sintered at 1400 °C. The two other pellets drop casted with the 0.15 and 0.75 vol% suspension, respectively, were sintered at 1450 °C. The sintering time for all pellets was one hour.

3.4.5 Effect of the sintering temperature

In order to investigate the effect of the sintering temperature on the densification of the thin films, the membranes were sintered at different temperatures. These temperatures were 1300, 1400 and 1450 °C. The spray coated membrane and the membrane drop casted with the 0.35 vol% suspension were sintered two times, first at 1300 °C for one hour, and then the spray coated membrane was sintered at 1400 °C for one hour, and the drop casted membrane at 1450 °C for one hour. The heating and cooling rate was 200 °C/min for all temperature programs.

3.4.6 Overview of membranes

An overview of all the finished membranes and their fabrication method can be found in Table 3.6.

3.5 Characterization of samples

3.5.1 Structure and composition

Identification of the product structure and composition was done by X-ray diffraction (XRD). The phase purity of each sample was examined by rapid scans of about 30 minutes, and longer scans of approximately five hours were used to investigate lattice parameters and space group. The measurements were obtained by a Bruker D8 Focus

Table 3.6: Fabrication details of the finished membranes.

Deposition method	Substrate composition	Suspension	Amount of suspension	Sintering temperature
Spray coating	YHMTO	2 vol%	6 mL	1300 °C, 1400 °C
Dip coating	YHMTO	1 vol%	-	1300 °C
Dip coating	Y090MTO	0.5 vol%	-	1300 °C
Dip coating	YHMTO	0.25 vol%	-	1400 °C
Drop casting	YHMTO	0.35 vol%	11 mL	1300 °C, 1450 °C
Drop casting	Y095MTO	0.25 vol%	6 mL	1400 °C
Drop casting	Y085MTO	0.25 vol%	6 mL	1400 °C
Drop casting	YHMTO	0.75 vol%	1 mL	1400 °C
Drop casting	YHMTO	0.75 vol%	1 mL	1450 °C
Drop casting	YHMTO	0.15 vol%	1 mL	1400 °C
Drop casting	YHMTO	0.15 vol%	1 mL	1450 °C

X-ray diffractometer with Cu Kα radiation, a voltage of 40 kV, 40 mA current, and 1.0 mm slit size. The short scans had a 2θ range of $10° - 75°$, while the longer scans had a 2θ range of $14° - 110°$. The obtained scans were analyzed by the program DIFFRAC.EVA v.4.1 and the results were matched to an existing PDF card which corresponded to the phase of the sample.

Pawley analysis was performed on XRD diffractograms from the produced powders in order to find the lattice parameters and crystallite sizes of the samples. The software Bruker AXS TOPAS v.5 was used with the instrument settings shown in Table 3.7. The initial starting points for the refinement of the lattice parameters were obtained from Gibbs et al. [18] for the hexagonal space groups, and were a = 6.14151(9) Å and c = 11.4013(2) Å for space group $P6_3cm$, and a = 3.618961(15) Å and c = 11.34090(9) Å for space group $P6_3/mmc$. For YMn_2O_5 with the orthorhombic space group $Pbam$ the lattice parameters were obtained from Noda et al. [40] and were a = 7.239(1) Å, b = 8.471(2) Å, and c = 5.664(3).

3.5.2 Microstructure

The microstructures of the samples were investigated in a Hitachi S-3400N scanning electron microscope (SEM). All of the micrographs were obtained using a secondary electron (SE) detector with an applied voltage of 15 kV and 40% probe current.

Table 3.7: Instrument and correction settings for the Bruker AXS TOPAS v.5 software for Pawley refinement on the X-ray diffraction data from nanocrystalline and bulk material.

Parameter	Value
Primary radius/Secondary radius	200.5 mm / 200.5 mm
LPSD angle range	4.1°
FSD angle	1/2 slit size
Linear PSD	yes
Source length	12 mm
Sample length	15 mm
Receiving slit length	12 mm
Primary/Secondary soller	2.5°
N Beta	30
LP factor	0
Background order	3 (nano), 6 (bulk)

The particle sizes of the powders made from the solid state synthesis were investigated by placing a small amount of powder on a double-sided carbon tape on a sample holder. The porosity of the substrates were investigated by polishing the surface of the support according to the method described in Section 3.4. The supports were then cleaned in ethanol and attached to a sample holder using a double-sided carbon tape with the polished surface pointing upwards. The porosity of one YHMTO substrate and one Y085MTO substrate was examined.

The thin film surfaces of the finished membranes were investigated with SEM. In order to examine the cross sections of the membranes, the pellets were cut in half and the cross sections were polished using the same polishing method as for the substrates. The fracture surfaces were then investigated by attaching the membrane to a sample holder with the fraction surface pointing upwards.

3.5.3 Sintering properties

Dilatometry measurements were performed on the different samples in order to determine how the chemical composition of the material influences the sintering properties. The measurements were carried out in a Netzsch DIL402C dilatometer. The bulk samples YMTO and Y095MTO prepared by the solid state synthesis were crushed and pressed into pellets of 5 mm diameter in a double action uniaxial pressing tool prior to testing. The nanocrystalline powder fired at 900 °C, N2(900), was also pressed into a 5 mm diameter pellet and tested. The temperature program for dilatometry testing is shown in Table B.1 in Appendix B. All dilatometry measurements were performed in synthetic air and heated to 1400 °C. The relative shrinkage of the pellets was measured and the optimal sintering temperature for each sample was found.

3.5.4 Oxygen adsorption and desorption

In order to determine the oxygen adsorption and desorption of the material and how this is affected by composition, thermogravimetric analysis was performed on the samples. A small amount of powder from each sample was weighed and heated in an alumina crucible in a Netzsch STA 449C thermal analysis system. Temperature programs and atmosphere are presented in Table B.2 in Appendix B. A background measurement was obtained for each temperature program prior to sample testing. Measurements were performed on bulk $YMn_{0.85}Ti_{0.15}O_3$ and $Y_{0.95}Mn_{0.85}Ti_{0.15}O_3$, and nanocrystalline $YMn_{0.85}Ti_{0.15}O_3$, N2(900).

Chapter 4

Results

4.1 Crystal structure and phase purity

4.1.1 Porous support and bulk powders

The results from the X-ray diffraction (XRD) analysis of the bulk samples produced by the solid state synthesis are presented in Figure 4.1, for $Y_{1\text{-}x}Mn_{0.85}Ti_{0.15}O_3$, where $x = 0$ (YMTO), $x = 0.05$ (Y095MTO), $x = 0.10$ (Y090MTO), and $x = 0.15$ (Y085MTO). The results from bulk $Y_{0.95}Ho_{0.05}Mn_{0.85}Ti_{0.15}O_3$ (YHMTO) are presented in Figure 4.2. The diffractograms in Figure 4.1 have been standardized to show the same maximum intensity, due to different amounts of powder being used for the measurements. The software DIFFRAC.EVA v4.1 was used to identify the phases in the samples, and the results were matched with the PDF card 04-011-9577, corresponding to hexagonal $YMnO_3$ and the space group $P6_3cm$. The positions of the characteristic diffraction lines from the PDF are included as black bars in the figures.

In both figures there are some discrepancies between the 2θ positions of the characteristic diffraction lines and the measured peaks. It can be seen that the (012) diffraction line is absent from the measured peaks, and the (004) peak is shifted towards a higher 2θ. These changes are consistent with a transition to the higher symmetry space group $P6_3/mmc$ as expected for Ti-doping. The absence of the (012) diffraction line is characteristic for a trimerization distortion, which occurs for the transition from $P6_3cm$ to $P63_{/}mmc$ [32]. In Figure 4.1 the (014) diffraction line is also missing, and this is also an indication of the space group $P6_3/mmc$ [32]. In Figure 4.2 the (014) reflection shows a small peak, but it has shifted slightly toward lower 2θ angles. This might also be a reflection from orthorhombic YMn_2O_5, which would indicate that the material has a small amount of impurities.

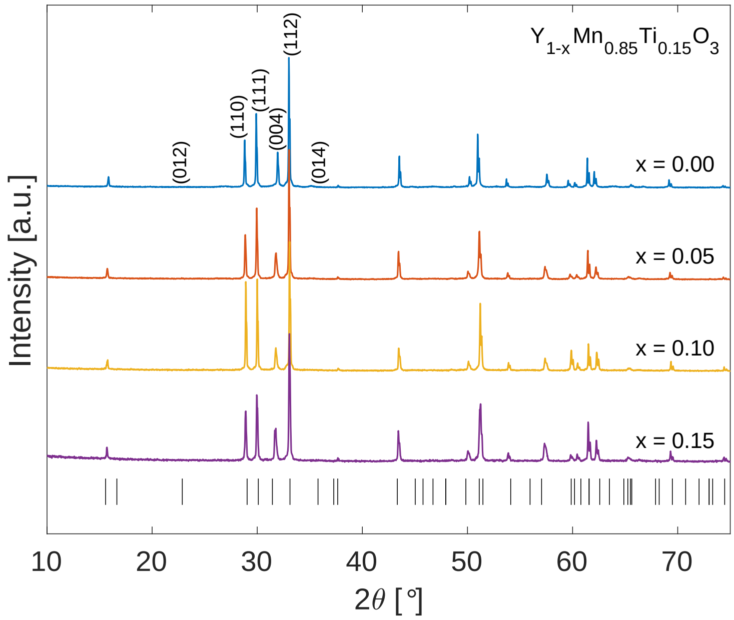

Figure 4.1: The X-ray diffractograms from analysis of the bulk $Y_{1-x}Mn_{0.85}Ti_{0.15}O_3$, where x = 0, 0.05, 0.10, and 0.15. The measurements have been standardized to show the same hight of the highest peak. The positions of the characteristic diffraction lines for hexagonal $YMnO_3$ are shown as black bars.

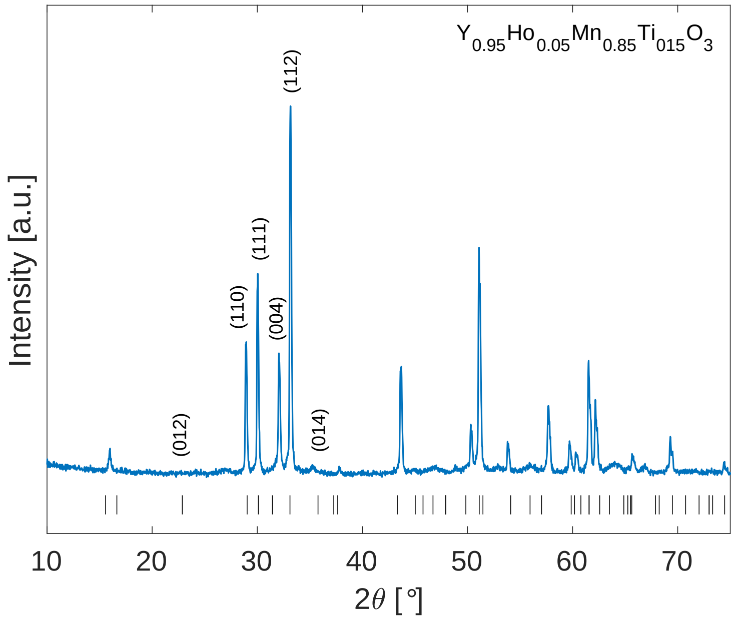

Figure 4.2: The X-ray diffractogram from the analysis of bulk $Y_{0.95}Ho_{0.05}Mn_{0.85}Ti_{0.15}O_3$. The positions of the characteristic diffraction lines for hexagonal $YMnO_3$ are shown as black bars.

Pawley refinement was used to calculate the lattice parameters of the samples from the XRD results, which can be seen in Table 4.1. The calculated lattice parameter in the a and c directions are denoted a and c, respectively, and are given in Ångström. R_{wp} is the goodness of fit, where a lower number means a better fit. The refinements were performed for all bulk samples for both space groups $P6_3cm$ and $P6_3/mmc$. The latter was included due to the absence of the (012) reflection, which is an indication of higher symmetry.

The refinements in Table 4.1 show how the lattice parameters are affected by Y-deficiency. The space group $P6_3/mmc$ has the best fit for YHMTO, YMTO, and Y095MTO. For Y090MTO and Y085MTO space group $P6_3cm$ fits best. The calculated lattice parameter c decreases with increasing Y-deficiency for space group $P6_3cm$, while the opposite trend is observed for the space group $P6_3/mmc$. For the a parameter, no obvious trend can be seen with increasing Y-deficiency. The values for the lattice parameters of $Y_{0.95}Ho_{0.05}Mn_{0.85}Ti_{0.15}O_3$ are very close to those of $YMn_{0.85}Ti_{0.15}O_3$, as both of these samples have no deficiency on the A-site. The values of the a parameter cannot be compared directly between the space groups. It has to be multiplied by $\sqrt{3}$ for space group $P6_3/mmc$ due to the unit cell tripling that occurs during the transition from lower to higher symmetry as shown in Equation 2.1.

Table 4.1: Results from the Pawley analysis of the X-ray diffraction data from bulk $Y_{1\text{-}x}Mn_{0.85}Ti_{0.15}O_3$ (Y(1-x)MTO), where x = 0, 0.05, 0.10, and 0.15, and bulk $Y_{0.95}Ho_{0.05}Mn_{0.85}Ti_{0.15}O_3$ (YHMTO) for the hexagonal space groups $P6_3cm$ and $P6_3/mmc$. The hexagonal lattice parameters, a and c, and goodness of fit, R_{wp}, are listed.

Sample	**Space group**	***a* [Å]**	***c* [Å]**	R_{wp}
YHMTO	$P6_3cm$	6.1558(13)	11.3843(16)	28.867
	$P6_3/mmc$	3.58358(12)	11.2178(5)	**11.220**
YMTO	$P6_3cm$	6.1615(7)	11.3974(9)	36.704
	$P6_3/mmc$	3.58386(6)	11.2182(3)	**12.967**
Y095MTO	$P6_3cm$	6.1578(10)	11.3476(12)	30.523
	$P6_3/mmc$	3.57086(7)	11.2632(3)	**11.671**
Y090MTO	$P6_3cm$	6.1569(5)	11.3368(6)	**27.201**
	$P6_3/mmc$	3.6226(3)	11.3190(9)	28.931
Y085MTO	$P6_3cm$	6.17930(18)	11.2743(4)	**10.502**
	$P6_3/mmc$	3.6395(3)	11.3315(11)	25.457

4.1.2 Nanocrystalline powder

The X-ray diffraction results for Y_2O_3, Mn_2O_3 and TiO_2 from standardization of the citric acid method precursors are presented in Appendix C.

The X-ray diffractogram from analysis of the nanocrystalline $YMn_{0.85}Ti_{0.15}O_3$ powder N1(800) produced by the citric acid method is presented in Figure 4.3. The results were matched to the PDF card 04-011-9577 for hexagonal $YMnO_3$ with space group $P6_3cm$, which is shown as black bars in the figure. The results also showed a small signal from a secondary phase, which was found to be orthorhombic YMn_2O_5 with space group $Pbam$. This was matched to the PDF card 00-034-0667 which is shown as red bars in the figure.

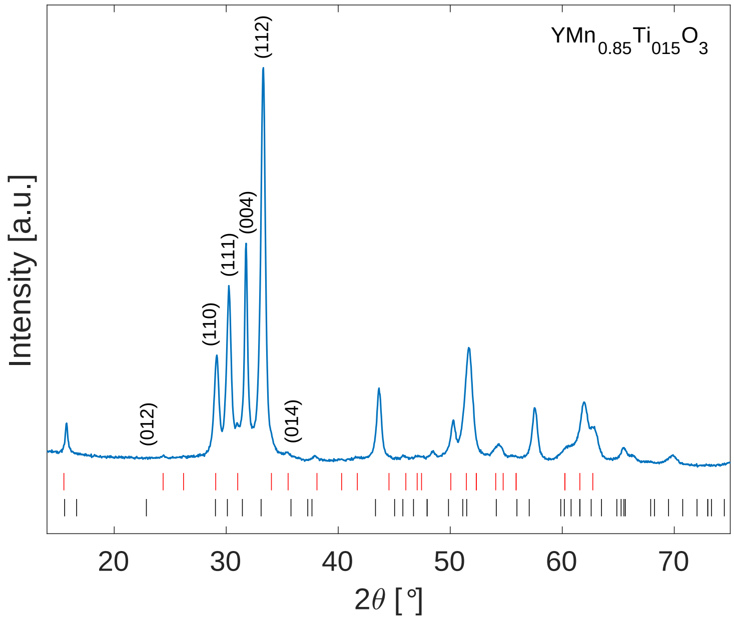

Figure 4.3: The X-ray diffractogram from the analysis of nanocrystalline $YMn_{0.85}Ti_{0.15}O_3$ produced by the citric acid method. The positions of the characteristic diffraction lines are shown as black and red bars for hexagonal $YMnO_3$ and orthorhombic YMn_2O_5, respectively.

Some differences can be seen between the measured results and the characteristic diffraction lines from $YMnO_3$. The (012) reflection is lost and the (004) has shifted to higher 2θ. As stated earlier, this indicates a trimerization and a transition from $P6_3cm$ to $P6_3/mmc$. In addition to this, the (014) reflection appears to have disappeared, which is also an indication of space group $P6_3/mmc$. However, due to the proximity of this reflection to the orthorhombic (112) reflection of YMn_2O_5 it is hard to distinguish them.

The sample has a very small crystallite size, evident by the wide peaks. It is also slightly amorphous, which can be seen by the widening of the peaks towards baseline of the measured values.

The X-ray diffraction results from analysis of the nanocrystalline powder from previous work are presented in Figure 4.4. The figure shows the results from the first firing at 800 °C, N2(800), obtained by Hoggen [39], as well as the results after the second firing at 900 °C, N2(900). The results were matched to hexagonal $YMnO_3$, which is shown as black bars in the figure. For both measurements, the (012) and (014) reflections are absent, while (004) has shifted slightly to a higher 2θ. All of this indicates the space group $P6_3/mmc$ associated with Ti-doping. The powder fired at 800 °C has a very small crystallite size, as revealed by the wide peaks, and is slightly amorphous. The powder fired at 900 °C shows slightly narrower peaks, indicating an increase in crystallite size. The peaks are also less rounded, suggesting that the sample is more crystalline than the one fired at 800 °C.

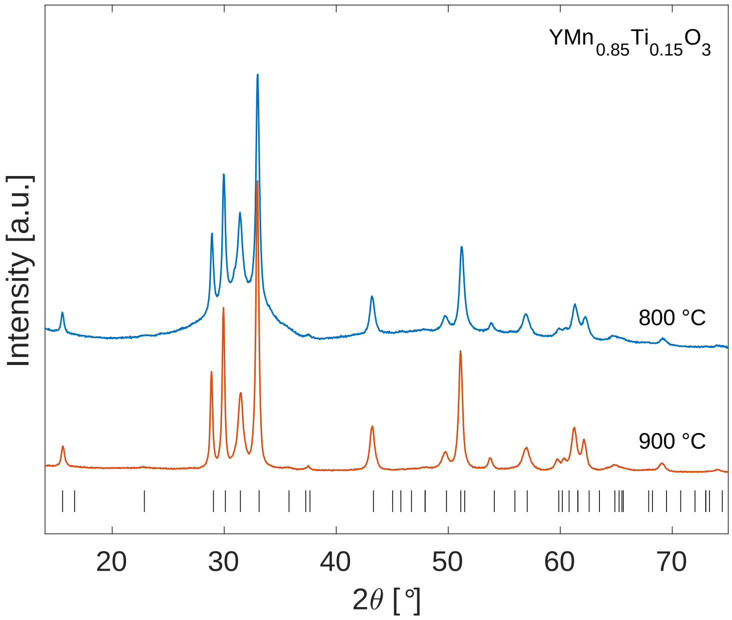

Figure 4.4: The X-ray diffractogram from the analysis of nanocrystalline $YMn_{0.85}Ti_{0.15}O_3$ produced for previous work [39] fired at 800 °C and 900 °C. The black bars indicate the positions of the characteristic diffraction lines for hexagonal $YMnO_3$. The diffraction results for the powder fired at 800 °C were obtained by Hoggen [39].

Pawley refinement was used to obtain lattice parameters and crystallite sizes for the nanocrystalline powder produced in this work, N1(800), for the nanocrystalline powder produced in previous work fired at 800 °C, N2(800), and for the powder fired a second time at 900 °C, N2(900). The refinements were done for both the hexagonal space groups $P6_3cm$ and $P6_3/mmc$. The lattice parameters a and c were calculated along with the crystallite sizes of the powders, and the results are presented in Table 4.2. All powders show a slightly better fit with space group $P6_3cm$. Comparison of the a values shows that the space groups have approximately the same lattice parameters for all samples. After firing the powder a second time at higher temperature, the crystallite size increased.

Table 4.2: Results from the Pawley analysis of the X-ray diffraction data from nanocrystalline $YMn_{0.85}Ti_{0.15}O_3$ for the hexagonal space groups $P6_3cm$ and $P6_3/mmc$. a and c are the hexagonal lattice parameters, and R_{wp} is the goodness of fit.

Sample	**Space group**	**a [Å]**	**c [Å]**	**Crystallite size [nm]**	**R_{wp}**
N1(800)	$P6_3cm$	6.1311(8)	11.2776(15)	23.2(2)	6.277
	$P6_3/mmc$	3.5401(3)	11.2764(13)	23.36(18)	6.502
N2(800)	$P6_3cm$	6.1789(18)	11.398(3)	16.15(19)	6.379
	$P6_3/mmc$	3.5682(6)	11.401(3)	16.27(18)	6.729
N2(900)	$P6_3cm$	6.1959(4)	11.3852(11)	33.4(3)	7.549
	$P6_3/mmc$	3.5774(2)	11.3859(10)	33.6(3)	7.745

Since the nanocrystalline sample, N1(800), showed a small signal from the orthorhombic YMn_2O_5, another Pawley refinement was performed that combined the hexagonal space group $P6_3cm$ with the orthorhombic space group $Pbam$. The results are presented in Appendix C. A better refinement was achieved when the orthorhombic phase was included, with R_{wp} = 3.033.

4.2 Microstructure

4.2.1 Porous support

The porosities of the supports were determined from SEM images of the polished pellet surfaces. The surfaces of one YHMTO pellet and one Y085MTO pellet are presented in Figure 4.5. It can be seen that the YHMTO pellet made from $Y_{0.95}Ho_{0.05}Mn_{0.85}Ti_{0.15}O_3$ has a quite porous microstructure and large pore sizes, while the Y085MTO pellet has a very low porosity. Since the support should allow for adequate flow of oxygen gas through the membrane, its porosity should be continuous. The porosity in the YHMTO pellet is sufficient and appears to be continuous. However, the pellet with Y-deficiency has a very low porosity and is too dense to allow for oxygen permeation.

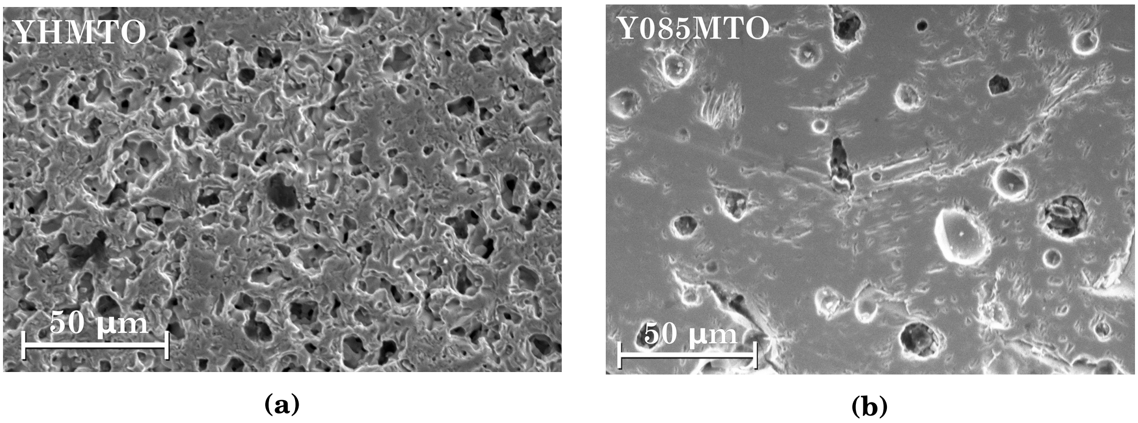

(a) (b)

Figure 4.5: The surfaces of the porous supports after firing at 1400 °C and polishing to 3 µm. (a) $Y_{0.95}Ho_{0.05}Mn_{0.85}Ti_{0.15}O_3$ support and (b) $Y_{0.85}Mn_{0.85}Ti_{0.15}O_3$ support.

The powders from the crushed samples were also investigated in SEM, and the resulting images are presented in Appendix D. The $Y_{0.90}Mn_{0.85}Ti_{0.15}O_3$ and $Y_{0.85}Mn_{0.85}Ti_{0.15}O_3$ powders had grain sizes larger than 20 µm, and were therefore too coarse to be processed further. TGA and dilatometry analysis were therefore not performed on these samples. The sieved nanocrystalline $YMn_{0.85}Ti_{0.15}O_3$ powder in Figure D.1f appeared to be agglomerated.

4.2.2 Asymmetrical membrane

The results from deposition of the functional layer onto the support by various deposition techniques are presented in this section. The effect of sintering temperature on the density of the thin film is also presented here.

Spray coating

In the first attempt to achieve a dense thin film, spray coating was used as deposition method. An YHMTO pellet was sprayed with a 2 vol% suspension and sintered at 1300 °C. SEM images of the surface of the membrane, which is the thin, functional layer, can be seen in Figure 4.6a. The polished cross-section of the membrane can be seen in Figure 4.6b. The surface of the membrane shows that the film is porous and quite uneven. However, some densification has occurred, as can be seen by the necking between particles on the surface. The cross-section of the membrane in Figure 4.6b shows the thin film to the left in the image, on top of the support. The porosity of the thin film is verified by the cross-section, where small pores are clearly visible. The film is approximately 14 μm thick. The support has maintained most of its porosity, and the pores still appear to be continuous.

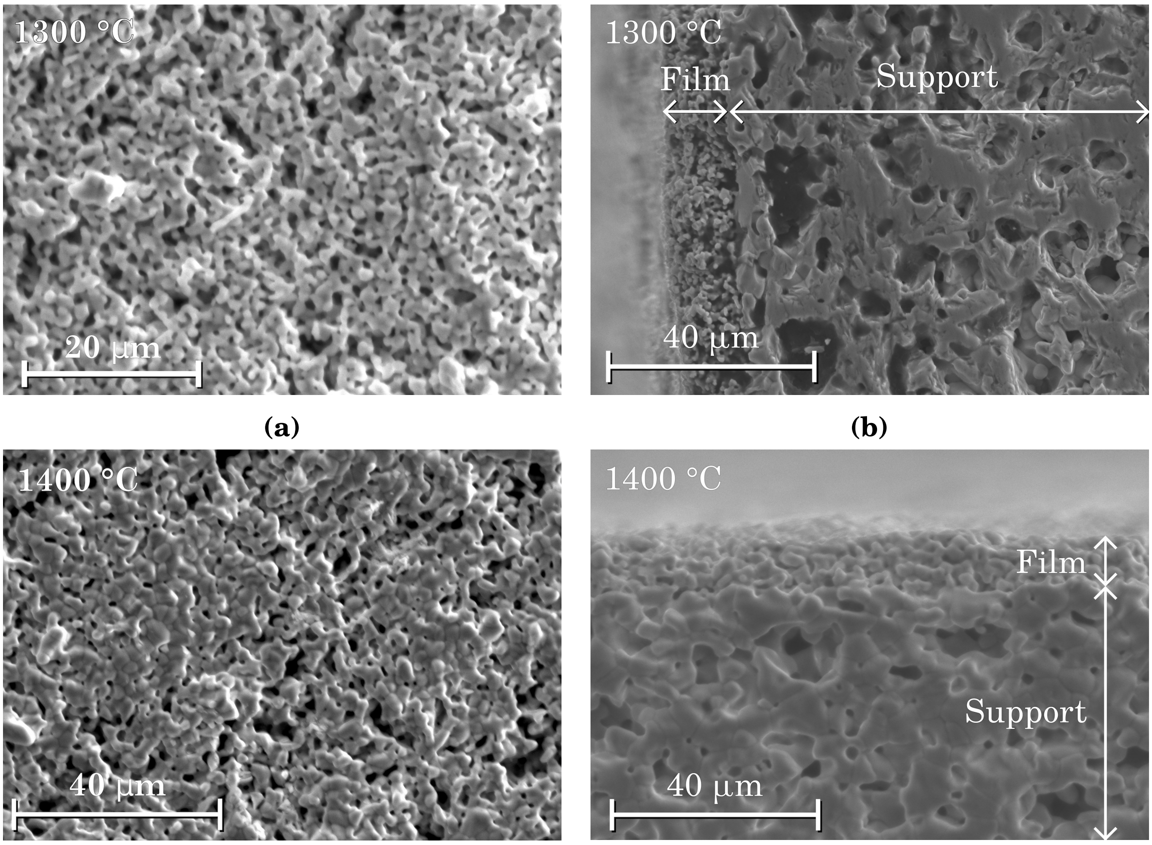

(a) **(b)**

(c) **(d)**

Figure 4.6: The surface of the functional layer (a) and the cross-section (b) of the asymmetrical membrane prepared by spray coating with a 2 vol% suspension and sintered at 1300 °C. (c) and (d) show the surface and cross-section of the same membrane sintered at 1400 °C.

In order to test the effect of the sintering temperature on the density of the asymmetrical membrane, the spray coated pellet was sintered a second time at 1400 °C for one hour. Figures 4.6c and 4.6d show the surface and cross-section of the spray coated membrane after it was sintered a second time. The image of the surface shows that the particles have grown compared to the first sintering at 1300 °C shown in Figure 4.6b, and the film has become denser. This is also verified by the cross-section, where the porosity has decreased. The thickness of the film has also decreased as a result of the increased densification of the film. The thin film after the second sintering is approximately 10 µm thick, compared to 14 µm after the first sintering. The support seen in the cross-section has also become denser after the second sintering, but appears porous enough to allow an adequate flow of gas.

Dip coating

Dip coating was used as another deposition technique in order to try to achieve a dense thin film. SEM images of the resulting asymmetrical membranes are shown in Figure 4.7. The surface of the membrane made by dipping an YHMTO pellet in a 1 vol% suspension and sintering at 1300 °C is shown in Figure 4.7a. The polished cross-section of the same membrane is shown in Figure 4.7b. The image of the surface shows that full coverage of nanoparticles on the substrate was not achieved, as the substrate is clearly visible in the left half of the image. In the right half of the image, the particles of the thin film can be seen. However, this is a very thin and porous layer and the substrate is visible through the film. This is also confirmed by the image of the cross-section, where a very thin layer of approximately 2 µm can be seen on top of the substrate. The deposited layer is porous, although some sintering of the particles has occurred, which can be seen by the necking of particles on the surface.

The pellet made from Y090MTO was dipped in a 0.5 vol% suspension and sintered at 1300 °C. The surface of the membrane is shown in Figure 4.7c and the polished cross-section in Figure 4.7d. The deposition of nanocrystalline particles was unsuccessful as no film can be seen on the substrate. The surface is very dense and has visible cracks. The surface is also very similar to that of the Y085MTO support in Figure 4.5b. Both Y090MTO and Y085MTO have quite large Y-deficiencies, and are expected to be quite dense. Due to this similarity between the surface of the dipped Y090MTO pellet and the undipped Y085MTO substrate, it is safe to say that no film was deposited. The image of the cross-section confirms that there is no film on top of the support, as the microstructure looks the same throughout the membrane. This cross-section also shows the density of the support and verifies that it is too dense for gas permeation.

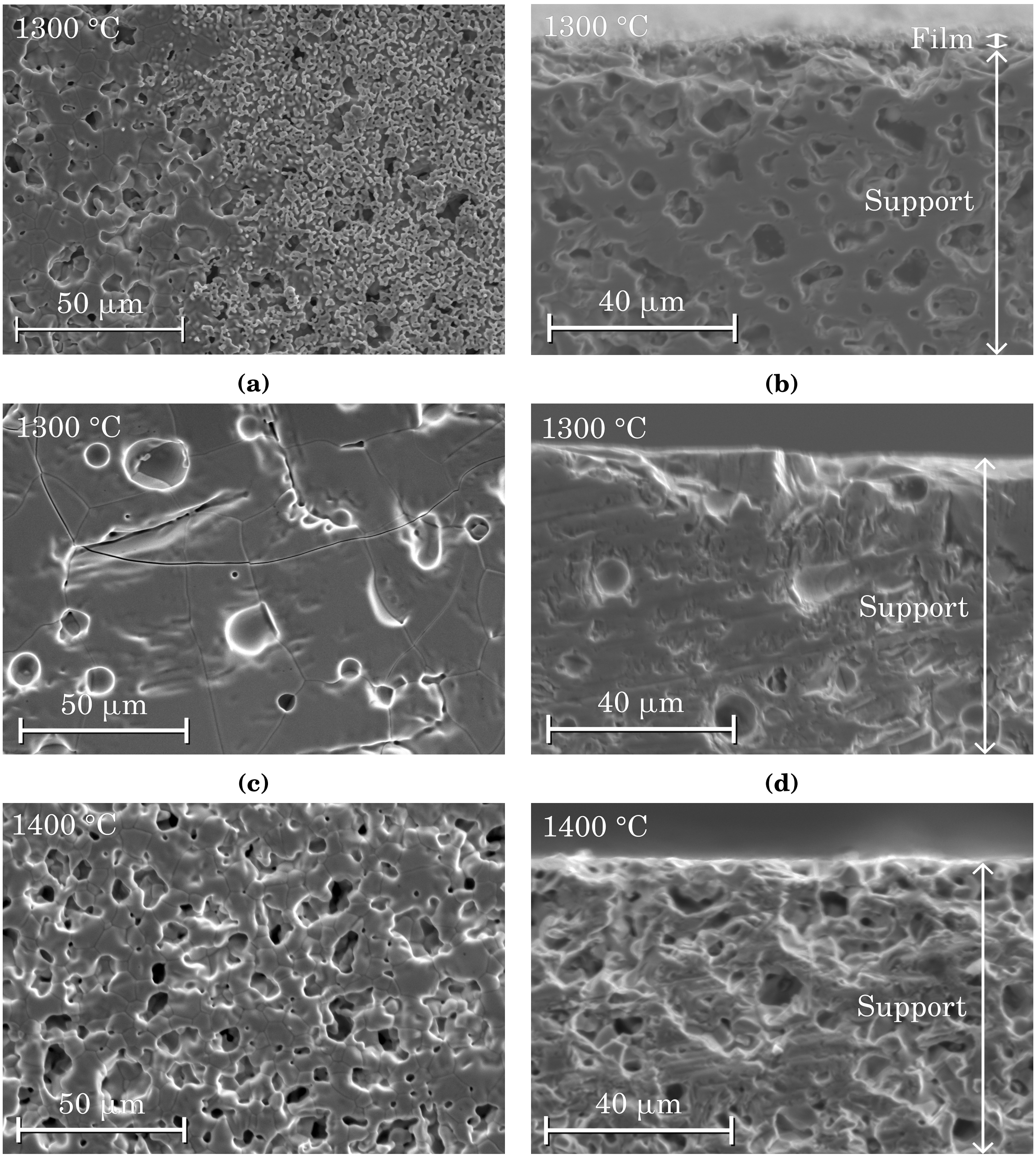

(a) (b)

(c) (d)

(e) (f)

Figure 4.7: The surface (a), (c), and (e), and the cross-section (b), (d), and (f) of the membranes prepared by dip coating. The $Y_{0.95}Ho_{0.05}Mn_{0.85}Ti_{0.15}O_3$ membrane in (a) and (b) was dipped in a 1 vol% suspension and sintered at 1300 °C, the $Y_{0.90}Mn_{0.85}Ti_{0.15}O_3$ membrane in (c) and (d) was dipped in a 0.5 vol% suspension and sintered at 1300 °C, and the $Y_{0.95}Ho_{0.05}Mn_{0.85}Ti_{0.15}O_3$ membrane in (e) and (f) was dipped in a 0.25 vol% suspension and sintered at 1400 °C.

An $Y_{0.95}Ho_{0.05}Mn_{0.85}Ti_{0.15}O_3$ pellet was dipped in a 0.25 vol% suspension and sintered at 1400 °C for one hour. Figure 4.7e shows the surface of the membrane, and Figure 4.7f shows the cross-section. As for the dip coated Y090MTO pellet, the dipping of this substrate did not yield a thin film. The surface of the pellet is very similar to the substrate prior to dipping, as shown in Figure 4.5a. The only visible difference between the surface before and after dipping is a slight increase in density, which is to be expected after sintering at 1400 °C. The cross-section also shows no sign of a film, and the microstructure in the cross-section appears to be homogeneous and similar to that of the support.

Drop casting

An $Y_{0.95}Ho_{0.05}Mn_{0.85}Ti_{0.15}O_3$ pellet was drop casted with a 0.35 vol% suspension and sintered at 1300 °C. Its surface is shown in Figure 4.8a and its cross-section in Figure 4.8b. The film is porous, which is clear from both the surface and the cross-section of the membrane. The thickness of the film varies from approximately 30 µm near the edges of the film, to around 15 µm around the center of the membrane. This thickness is overall too thick for the desired application, meaning that less suspension is needed for deposition. Figure 4.8a shows that the film has not undergone much densification, but the particles have started necking together. This suggests that a higher sintering temperature is needed for further densification of the film.

Figures 4.8c and 4.8d shows the surface and cross-section, respectively, of the pellet drop casted with a 0.35 vol% suspension after being sintered a second time at 1450 °C for one hour. The functional layer has become much more dense after the second sintering than after sintering at 1300 °C, as can be seen by clear necking and particle growth on the surface. The cross-section of the membrane verifies this densification, as almost no pores can be seen in the cross-section of the film. The film is approximately 14 µm thick across the entire film, which is also a sign of larger shrinkage and simultaneous densification, since the film after sintering at 1300 °C was up to 30 µm thick. This film shows even further densification after the second sintering than was observed for the spray coated membrane sintered at 1400 °C, where the difference in film thickness before and after the second sintering was only 4 µm. The support has also become more dense. It appears to have a porosity that borders on being closed, and the substrate should therefore be made somewhat more porous prior to sintering at 1450 °C.

Figure 4.9 shows the Y095MTO pellet drop casted with a suspension with 0.25 vol%

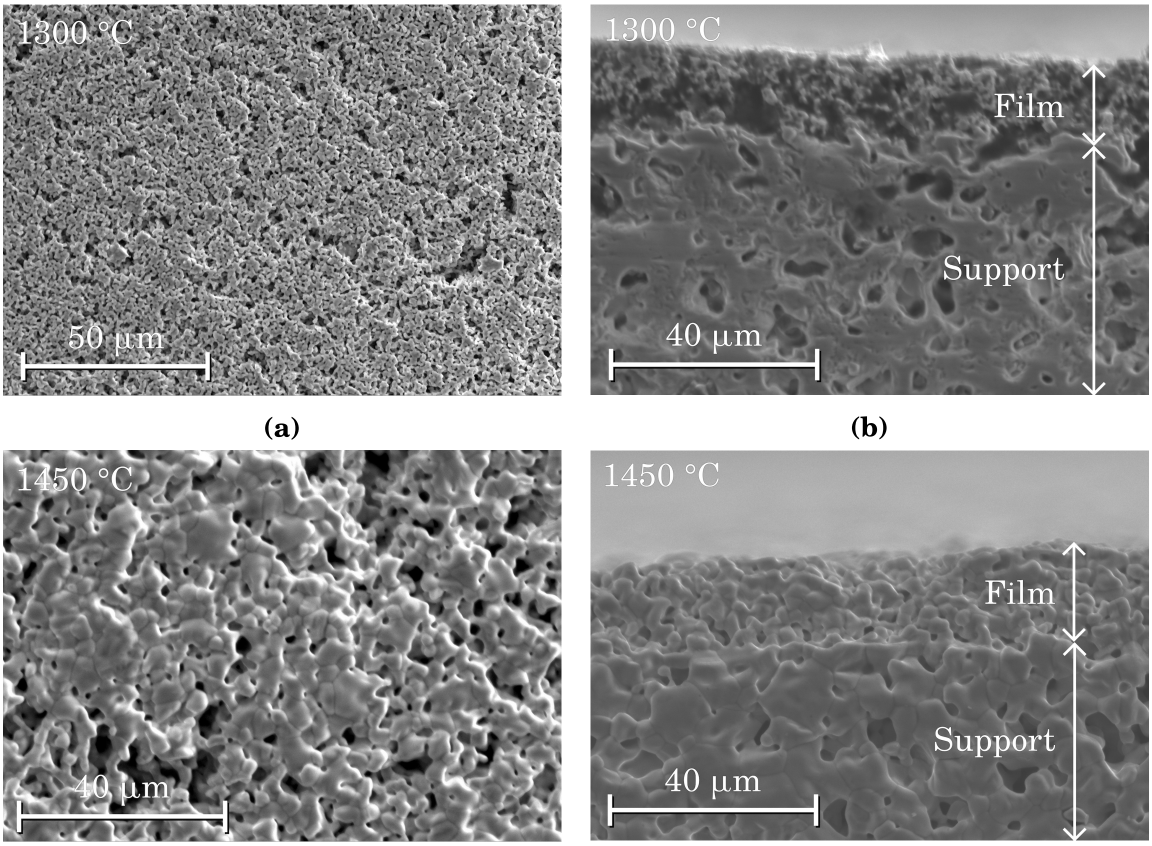

(a) **(b)**

(c) **(d)**

Figure 4.8: The surface (a) and cross-section (b) of the asymmetrical $Y_{0.95}Ho_{0.05}Mn_{0.85}Ti_{0.15}O_3$ membrane prepared by drop casting with a 0.35 vol% suspension and sintered at 1300 °C. (c) and (d) show the surface and cross-section, respectively, of the same membrane sintered a second time at 1450 °C.

solid load and sintered at 1400 °C. The film was compressed by uniaxial pressing prior to sintering in order to try to increase the packing of the particles. The surface in Figure 4.9a, shows very good necking between the particles and a quite dense film. It still has some porosity, but much less than the membrane drop casted with a 0.35 vol% suspension and sintered at 1300 °C, as shown in Figure 4.8a. The particles are considerably larger compared to those in Figure 4.8a, which is to be expected from the higher sintering temperature. The film also shows some cracking on the surface, which is shown by the red arrow in Figure 4.9a.

The cross-section in Figure 4.9b does not show a film. However, as can be seen from Figures 4.9c and 4.9d, the film has broken off in some places. The film has most likely been broken off the substrate at the fracture site during cutting and polishing of the cross-section. Figure 4.9c shows a large rift in the membrane and cracking of the film, separating it from the substrate. Some of the broken film pieces are marked by red arrows. The cracking of the thin film has occurred in a circular fashion, suggesting it cracked as a result of the uniaxial pressing. The fragmented pieces of the thin film have achieved a greater density than the parts still attached to the substrate, and have shrunk noticeably. Figure 4.9d shows the edge of the membrane, and also here it can be seen that the film is flaking off the substrate. The difference between the substrate and the thin film can be seen in this image, as the film has smaller particles and smaller pores. The boundary where the film has broken off is marked by a red arrow. Also in this image, a large rift in the membrane can be seen in the top left corner of the image. It is likely that this crack also comes from the applied pressure.

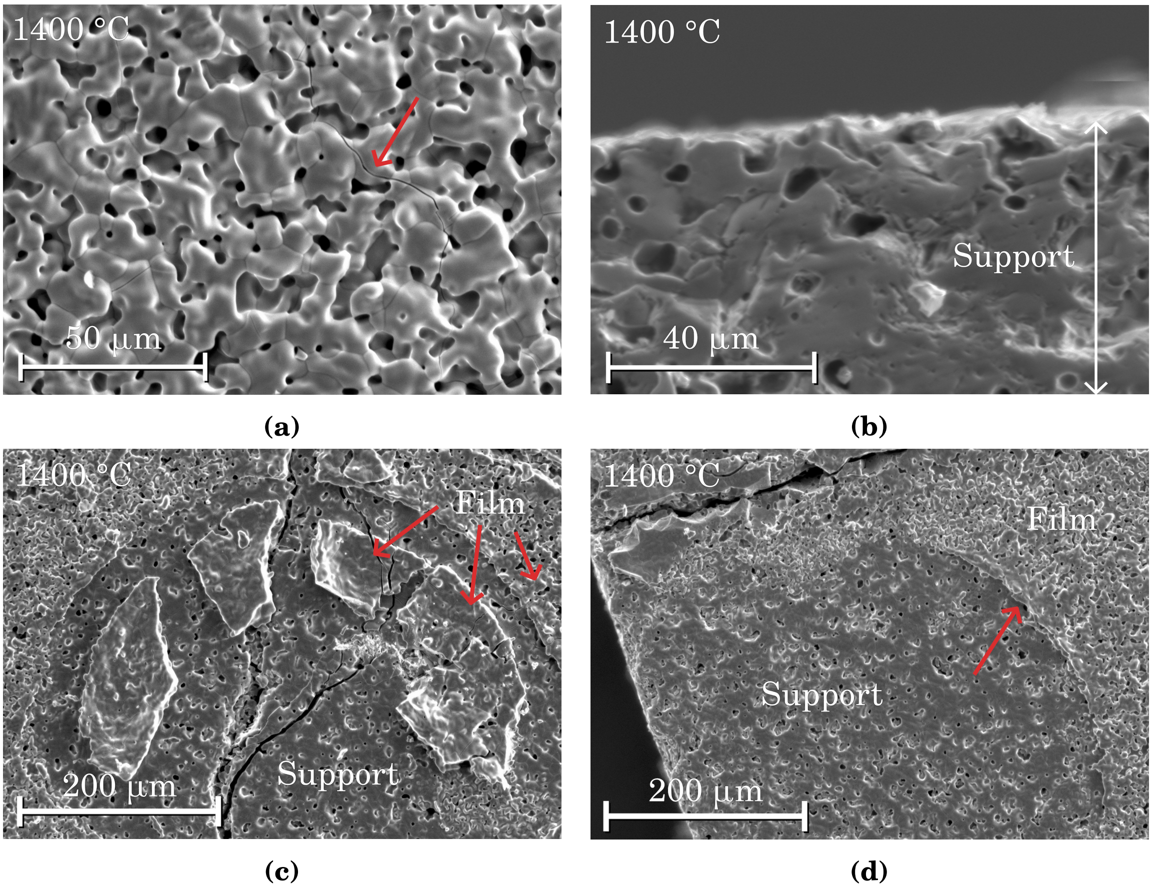

(a) **(b)**

(c) **(d)**

Figure 4.9: The surface (a) and cross-section (b) of the asymmetrical $Y_{0.95}Mn_{0.85}Ti_{0.15}O_3$ membrane prepared by drop casting with a 0.25 vol% suspension, compressed with uniaxial pressing, and sintered at 1400 °C. (c) The surface of the membrane showing cracking of the membrane. (d) The surface of the membrane at its edge, showing a large crack and flaking of the membrane.

The Y085MTO pellet drop casted with a 0.25 vol% suspension and sintered at 1400 °C can be seen in Figure 4.10. The only difference in deposition method between this membrane and the Y095MTO membrane presented in Figure 4.9, is that no pressure was applied to the functional layer of the Y085MTO membrane after deposition. From Figure 4.10a it can be seen that a dense film was achieved. The nanoparticles have sintered together and created a continuous, dense thin film. The cross-section in Figure 4.10b shows a very thin, smooth surface on top of the substrate. This suggests that the film is very thin, in the range of a few microns. As can be seen in Figure 4.10c, cracking of the functional layer occurs at the edge of the membrane suggesting that the film is quite brittle. Some small cracks can also be seen in the thin film itself, but no large cracks like the ones in Figures 4.9c and 4.9d are visible.

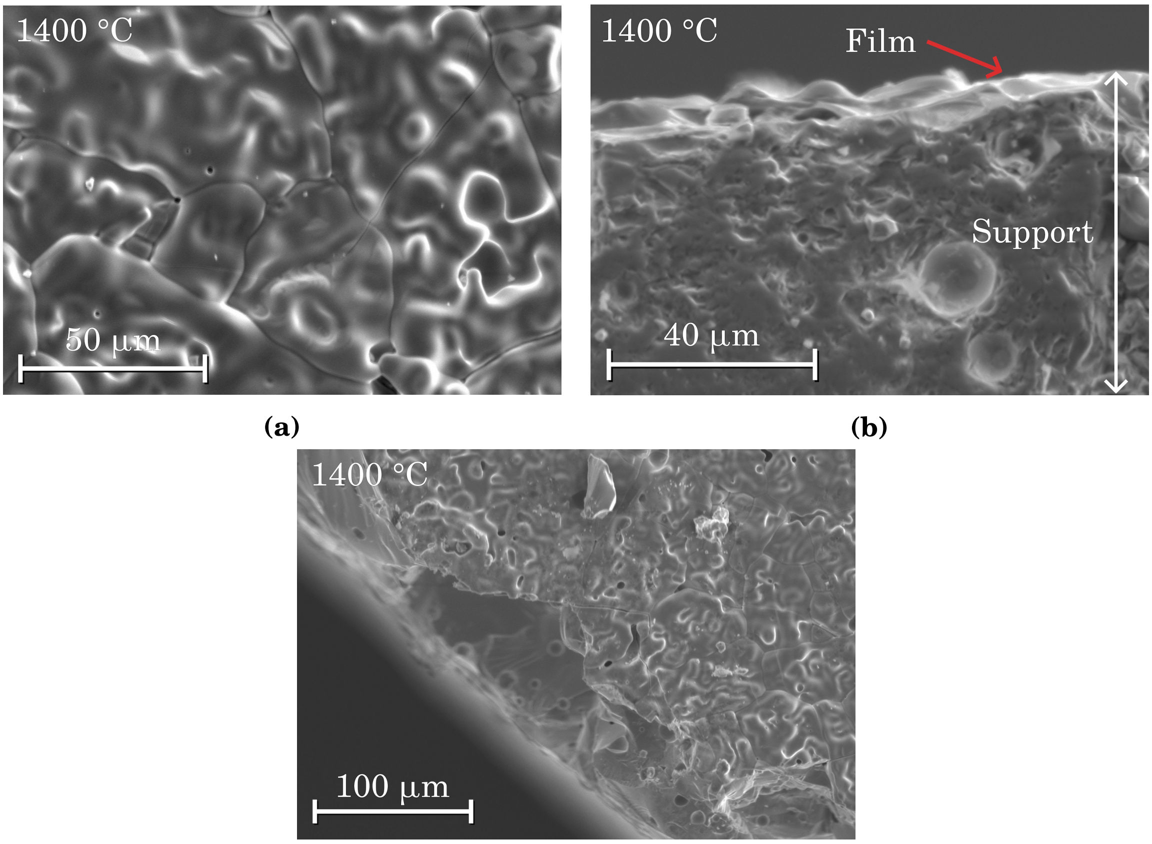

(a) **(b)**

(c)

Figure 4.10: The surface (a) and cross-section (b) of the asymmetrical membrane prepared by drop casting with a 0.25 vol% suspension and sintered at 1400 °C. (c) The edge of the membrane showing flaking of the thin film.

The two $Y_{0.95}Ho_{0.05}Mn_{0.85}Ti_{0.15}O_3$ membranes prepared by drop casting with a 0.75

vol% suspension are shown in Figure 4.11. The surface of the functional layer and the cross-section of the membrane sintered at 1400 °C is shown in Figure 4.11a and 4.11b, respectively. The surface and cross-section of the membrane sintered at 1450 °C can be seen in Figure 4.11c and 4.11d, respectively. None of these films are dense, and they have an irregular topography. The film has formed clusters, which could be seen already during deposition of the film. A very thin, porous film can be seen in the areas without clusters. Figure 4.11b shows the cross-section of the thin, porous film. Figure 4.11d shows the cross-section of one of the clusters. All of the clusters seem to be adequately dense, with only small, discontinuous pores, while the thin film covering the rest of the surface is too porous. The membrane sintered at 1450 °C shows a higher density than the one sintered at 1400 °C. This is true both for the clusters and the remaining thin film. The thickness of the film sintered at 1400 °C varies from 60 µm at the clusters to around 15 µm in the areas without clusters. The film sintered at 1450 °C varies from 50 µm at the clusters to around 10 µm in the areas without clusters.

Figure 4.12 shows the two membranes drop casted with a 0.15 vol% suspension. Figures 4.12a and 4.12b show the surface and cross-section, respectively, of the membrane sintered at 1400 °C. Figures 4.12c and 4.12d show the surface and cross-section of the membrane sintered at 1450 °C. The film has formed clusters of dense film in these membranes as well, while a porous, thin layer covers the rest of the surface. In Figure 4.12c a cluster covers half of the image, clearly showing the differences in density between the cluster and the rest of the film. All of the clusters are sufficiently dense, with the one sintered at 1450 °C being more dense than the one sintered at 1400 °C. The thin film covering the rest of the surface also has higher density when sintered at 1450 °C. Both of the cross-sections show the dense clusters. In Figure 4.12b the support is out of focus because the cluster lies further in on the support than the fracture surface. The thickness of the film sintered at 1400 °C varies from approximately 10 µm to 35 µm, while the one sintered at 1450 °C varies from around 7 µm to 60 µm at the clusters.

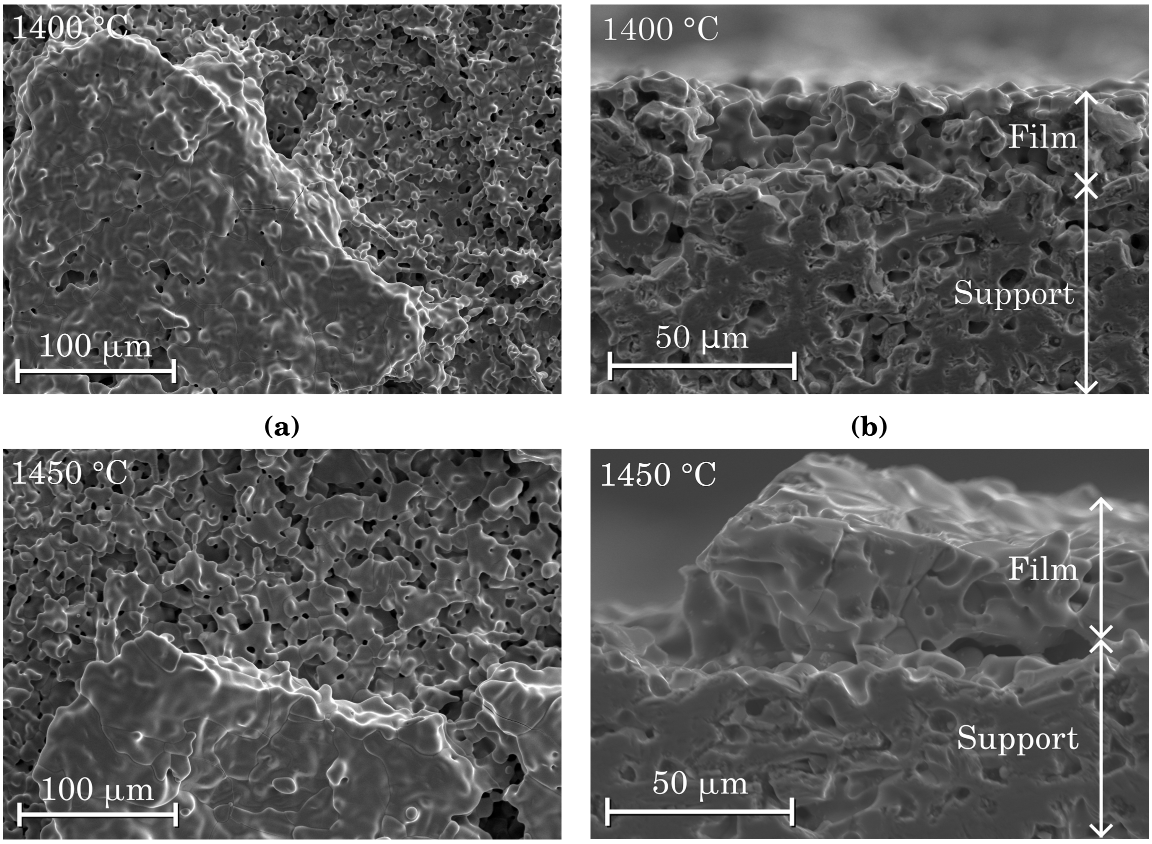

(a) **(b)**

(c) **(d)**

Figure 4.11: The surface, (a) and (c), of the functional layer and cross-section, (b) and (d), of the two asymmetrical membranes prepared by drop casting with a 0.75 vol% suspension. (a) and (b) shows the membrane sintered at 1400 °C, and (c) and (d) shows the membrane sintered at 1450 °C.

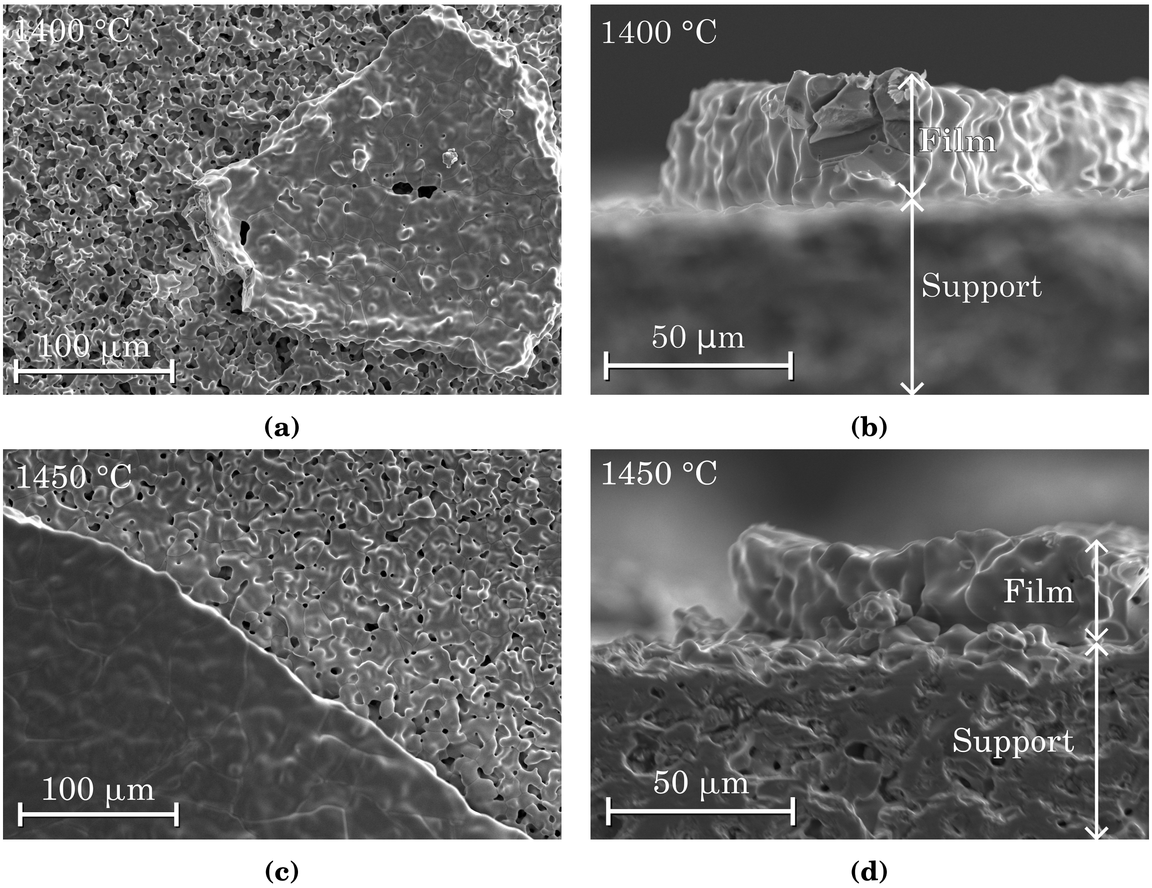

(a) **(b)** **(c)** **(d)**

Figure 4.12: The surface, (a) and (c), of the functional layer and cross-section, (b) and (d), of the two asymmetrical membranes prepared by drop casting with a 0.15 vol% suspension. (a) and (b) shows the membrane sintered at 1400 °C, and (c) and (d) shows the membrane sintered at 1450 °C.

4.3 Sintering properties

The sintering properties of the samples were tested by dilatometry according to the temperature program shown in Appendix B, Table B.1. The results are presented in Figure 4.13, where the data from nanocrystalline $YMn_{0.85}Ti_{0.15}O_3$ powder fired at 800 °C in Figure 4.13c was obtained in previous work [39]. The results are given in percentage as the change in length, dL, relative to the initial length, L_0.

For all samples, the length increases by approximately 2% before it starts to decrease around 1100 °C. The optimal sintering temperature can be found from the inflection point in the sintering graph. The bulk samples in Figure 4.13a and 4.13b do not show an inflection point, which means that the optimal sintering temperature is above 1400 °C and cannot be determined from these results. However, the sample with 5% Y-deficiency shows a much larger relative shrinkage at 1400 °C than the sample with no Y-deficiency. The shrinkage is approximately 2.5% and 0.3% for Y095MTO and YMTO, respectively, suggesting that Y-deficiency promotes sintering. The relative shrinkage is quite low for both samples, suggesting that some of the sintering capacity had already been used during earlier heat treatments.

The nanocrystalline sample shows a much higher sintering capacity than the bulk samples, with a shrinkage of almost 35% after firing at 800 °C, as shown in Figure 4.13c. After firing at 900 °C, as shown in Figure 4.13d, the shrinkage dropped to 30%, which is still much higher than for the bulk samples. The optimal sintering temperature is found from the inflection point, which is approximately 1300 °C for both samples. The weight of the dilatometry pellets made by nanocrystalline powder was about half of the bulk pellets, even though they had approximately the same dimensions. Since the nanocrystalline material had a lower green body density than the bulk samples, the sintering capacity was higher. Finer-sized material will also sinter faster and at lower temperatures as mentioned in Section 2.6.3. The results in Figure 4.13 are consistent with this, since the nanocrystalline samples show an inflection point lower than 1400 °C, while the bulk samples do not.

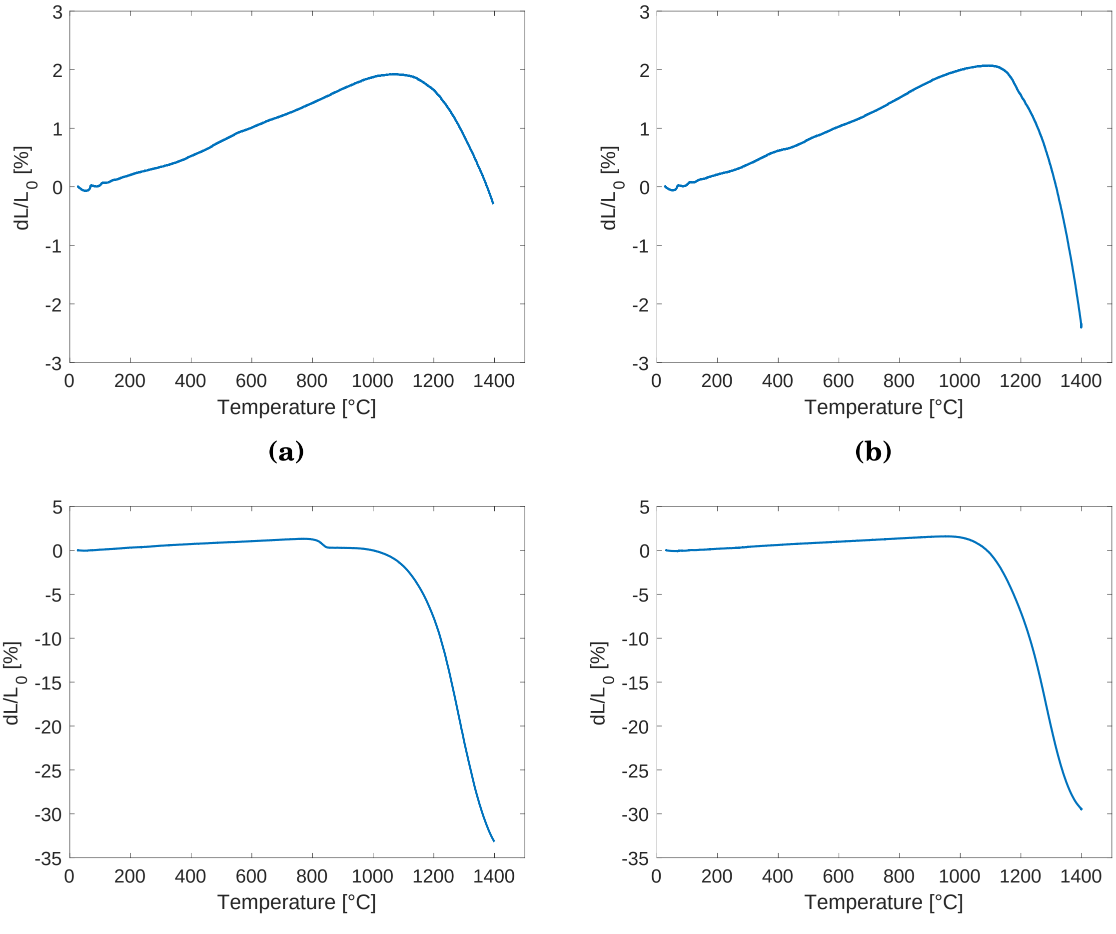

(a) **(b)** **(c)** **(d)**

Figure 4.13: Results from the dilatometry analysis of bulk $YMn_{0.85}Ti_{0.15}O_3$ (a) and $Y_{0.95}Mn_{0.85}Ti_{0.15}O_3$ (b) made by the solid state method, and nanocrystalline $YMn_{0.85}Ti_{0.15}O_3$ made by the citric acid method before (c) and after (d) firing at 900 °C. Figure (c) is reprinted from Hoggen [39]. dL is change in length, and L_0 is the initial length of the pellet.

4.4 Oxygen adsorption and desorption

Thermogravimetric analysis was used to measure the oxygen adsorption and desorption of the samples. The results from running the temperature program seen in Table B.2 can be seen in Figures 4.14a, 4.14b, and 4.14c, for samples $YMn_{0.85}Ti_{0.15}O_3$, $Y_{0.95}Mn_{0.85}Ti_{0.15}O_3$, and nanocrystalline $YMn_{0.85}Ti_{0.15}O_3$ fired at 900 °C, respectively. The first heating cycle was performed with a heating/cooling rate of 10 °C/min and can be seen as dashed lines in the figures. The second heating cycle had a slower heating/cooling rate of 1 °C/min and is shown with solid lines in the figures. The results obtained during heating are marked in red, while the results obtained during cooling are marked in blue.

In the first heating cycle for bulk $YMn_{0.85}Ti_{0.15}O_3$, shown in Figure 4.14a, an increase in mass starts at around 250 °C and peaks around 375 °C before it starts to decrease again. During cooling, the increase in mass is continuous until approximately 300 °C where it starts to level out. At 600 °C the mass has not yet reached equilibrium, which would be shown as a stabilization of the mass. The second heating cycle performed with a slow heating/cooling rate shows the most oxidation in the temperature range 175–425 °C with a peak around 325 °C. At 600 °C the mass is lower than during the first heating cycle, suggesting that some water or gases such as CO_2 was initially adsorbed to the material, which evaporated during the first heating cycle. The mass has not yet reached equilibrium at 600 °C even with the slow heating rate of 1 °C/min. During cooling, the oxidation reaches a higher mass than during the first cycle, and at the end of the measurement the material continues to oxidize slightly, suggesting that equilibrium has not yet been reached. This suggests that an even slower heating/cooling rate than 1 °C/min should be applied in order to reach equilibrium.

For bulk $Y_{0.95}Mn_{0.85}Ti_{0.15}O_3$, shown in Figure 4.14b, the oxidation during the rapid, first heating cycle occurs in the range 225–500 °C, with a peak around 375 °C. During the slow, second heating cycle, the most oxidation occurs in the range 190–475 °C with a peak at 315 °C. The mass reduces to a lower mass during the slow heating rate and oxidizes to a higher mass during the slow cooling rate, than during the rapid cycle. This shows that the material had more time to reach equilibrium in the second cycle. The rapid change in mass at the start of the second heating step is most likely noise in the background measurement.

The first heating step for nanocrystalline $YMn_{0.85}Ti_{0.15}O_3$, shown in Figure 4.14c, shows a steady decrease in mass throughout the heating step, with a convexity in the approximate temperature range 225 to 310 °C, suggesting oxidation. The cooling step results in an oxidation that occurs more rapidly in the range 300 to 200 °C, but still levels out at a lower mass than the start mass. This suggests that water or other impurities were initially adsorbed to the material. The slow, second heating step follows a trend similar to that of the rapid, first heating step, only with a lower initial mass and a slightly more defined oxidation convexity in the temperature range 175 to 275 °C. This shape of the heating step suggests that there is still some excess water or gases attached to the material. At 600 °C, the mass is almost stable, suggesting that the material has nearly reached equilibrium. The slow cooling step results in an oxidation that occurs most rapidly in the range from 300–200 °C. The material continues to oxidize all the way down to room temperature, suggesting that it has not yet reached equilibrium at the end of the measurement. The final mass is lower than the mass after the first, rapid cooling step, which supports the assumption that water was initially adsorbed in the material. The rapid increase in mass at the start of the second heating step is most likely background noise.

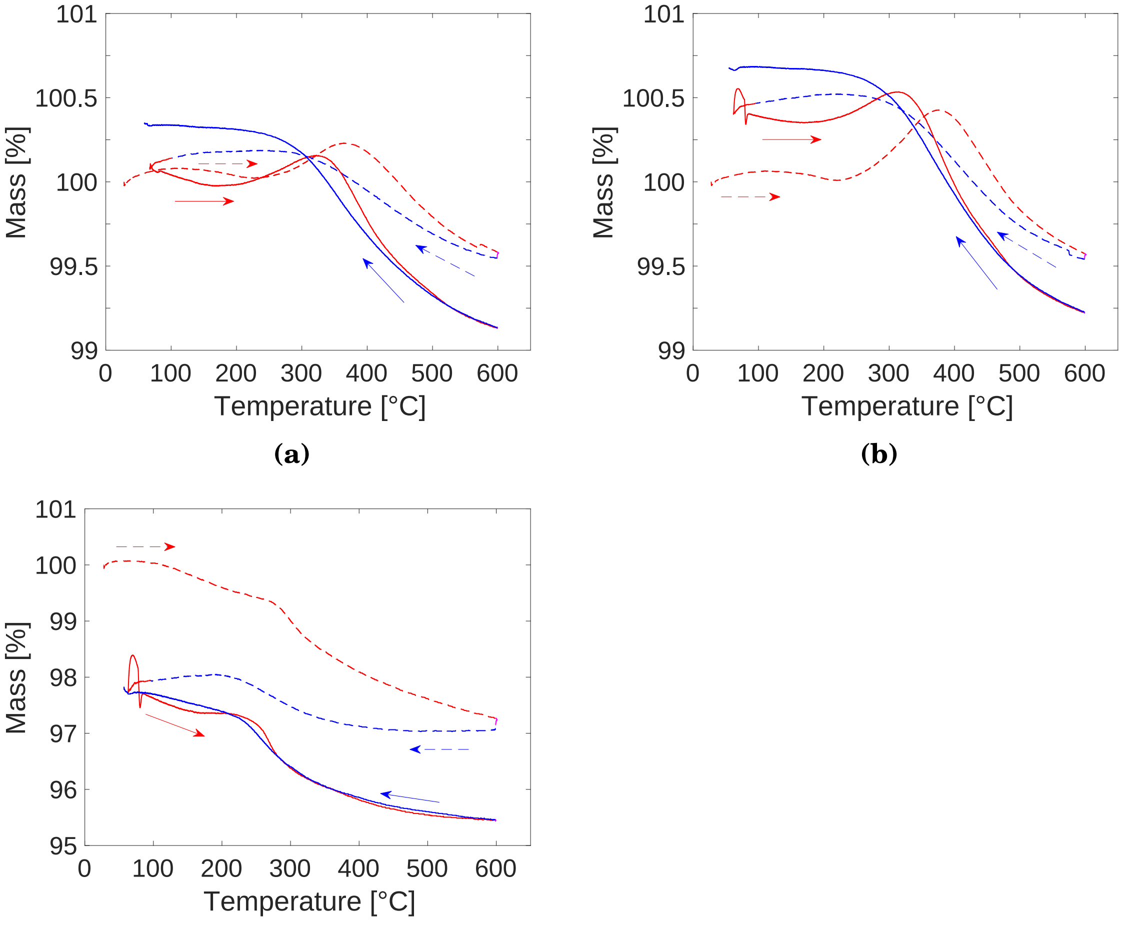

(a)

(b)

(c)

Figure 4.14: Results from thermogravimetric analysis. The change in mass is given in percentage, where 100% is the initial mass. The red lines indicate heating and the blue lines indicate cooling. Dashed lines mark the first loop with a heating/cooling rate of 10 °C/min, while the solid line indicated a heating/cooling rate of 1 °C/min. (a) bulk $YMn_{0.85}Ti_{0.15}O_3$, (b) bulk $Y_{0.95}Mn_{0.85}Ti_{0.15}O_3$, and (c) nanocrystalline $YMn_{0.85}Ti_{0.15}O_3$ fired at 900 °C.

Chapter 5

Discussion

The fabrication route of the porous support and the dense thin film will be discussed in this section, with the deposition and sintering temperature of the thin film being the most critical steps. The effect of titanium doping and yttrium deficiency on the crystal structure will be discussed, as well as the oxygen adsorption of the material.

5.1 Processing of the asymmetrical membrane

5.1.1 Porosity of support

The fabrication of the support by the solid state method is a fairly simple process that allows control over stoichiometry and porosity. As explained in Section 1.2 the pores in the support are required to be large enough to accommodate sufficient gas flow, and at the same time provide the mechanical strength for the thin film to withstand the partial pressure difference across the membrane. The supports made from $Y_{0.95}Ho_{0.05}Mn_{0.85}Ti_{0.15}O_3$ (YHMTO) presented in Figure 4.5a, show a satisfactory porosity that appears to be continuous when investigated by scanning electron microscopy (SEM). The support of composition $Y_{0.85}Mn_{0.85}Ti_{0.15}O_3$ (Y085MTO) shown in Figure 4.5b displays a closed porosity and will be too dense to allow an oxygen flow, suggesting that full occupancy of the A-site is beneficial for porosity.

The porosity of the supports decreased after sintering of the deposited thin film. The porosity still appears to be continuous for the YHMTO membranes after sintering at 1300 °C, but after sintering at higher temperatures the membranes seem to be too dense to allow an adequate flow of oxygen gas. Therefore, pore formers should be added to the support when sintering the membrane above 1300 °C to ensure the support remains porous enough during the entire membrane processing.

5.1.2 Deposition of thin film

Suspension stability

Pawley analysis of the nanocrystalline material presented in Table 4.2 shows that the crystallite size of the powder is nanosized, ranging from 16 to 33 nm. Even though the crystallite size of the powder was found to be sufficiently small, the particles were agglomerated as a result of being produced by the citric acid method. Due to this, the particles were mortared and sieved prior to further processing, but they were still agglomerated when dispersed in the suspension. Due to the agglomerated particles, the suspensions were not stable and the particles started to settle right away. This means that the suspensions were not stable when deposition occurred, which could affect the homogeneity and smoothness of the deposited films.

The agglomerated particles could lead to a less dense packing of the deposited particles, thus prohibiting proper sintering of the film. The deposition of just one larger particle could be detrimental to the density of the thin film. Therefore, the particles should have a very small particle size, a narrow particle size distribution, and not be agglomerated.

Spray coating

Spray coating of the membranes resulted in a layer with an even thickness, but porous microstructure, as shown in Figure 4.6. The thickness of the film is easily controlled by spray coating, but it did not yield a dense film in this study. Some densification occurred, as can be seen by the necking between particles at 1300 °C, and after sintering at 1400 °C even more densification had occurred, suggesting that not all of the sintering capacity had been used during the first sintering. Even after the second sintering, the film was not dense, suggesting that a closer initial packing of particles is required than can be achieved by spray coating. Therefore, spray coating is not the most suitable deposition method for producing a dense thin film of this material.

Dip coating

Dip coating did not result in a dense thin film for any of the membranes in this study presented in Figure 4.7. Only one of the dip coated supports obtained a surface partly covered by particles. This film was only a few microns thick, which means that if a completely covered surface were to be obtained and properly densified, this would lead to a very thin diffusion distance for oxygen ions and a larger oxygen flux. The reason why particles did not attach very well to the dipped supports, could be due to the unstable suspension. Previous research performed by Østli [41], which included dip coating, did result in a deposited film. The suspensions used by Østli were stabilized by a surfactant and ball milled directly prior to dipping, which could lead to both smaller particles and a narrower particle size distribution.

Only the suspension with 1 vol% solid load resulted in particles attached to the support, while the ones with 0.5 and 0.35 vol% did not. This suggests that more particles in the suspension is better for use with dip coating, and it is not recommended that suspensions of less than 1 vol% is used for dip coating.

A study performed by Wagner [42] resulted in a successful production of dense thin film on a porous support by use of dip coating. These membranes were made from $La_{0.2}Sr_{0.8}Fe_{0.8}Al_{0.2}O_{3-\delta}$ and were triply dip coated and sintered at 1230 °C for two hours. The support was made using 30 wt% carbon black as pore former mixed with the precursors in the solid state method. The suspensions were stabilized using DOLACOL D 1003 as a surfactant, same as Østli used. The $La_{0.2}Sr_{0.8}Fe_{0.8}Al_{0.2}O_{3-\delta}$ asymmetrical membranes reached oxygen fluxes up to 15.33 $mLmin^{-1}cm^{-2}$. These results show that it is possible to prepare a functioning asymmetrical membrane by dip coating.

If dip coating is to be used as a deposition method for $YMn_{0.85}Ti_{0.15}O_3$ membranes, adjustments need to be made that will increase the stability of the suspension and ensure that the deposited particles are packed closely enough to form a dense thin film. The use of a surfactant in the suspension appears to be a promising measure.

Drop casting

Drop casting of the films gave the highest density of all the fabrication methods in this study. As can be seen in Figure 4.10, a dense film was achieved when the deposited suspension had settled for five minutes and contained only small particles, which could be seen by the light brown color and stability of the suspension. The sintering temperature that resulted in the dense film was 1400 °C. The functional layer of the membrane has some small microcracks and appears to be quite brittle, probably due to the small thickness of the film. The support of this membrane was Y085MTO and the different compositions of the suport and film can be the reason for the microcraking.

The microcracking most likely occurred during cooling of the membrane after sintering.

Applying a pressure on the deposited functional layer did not result in improved densification of the film. The two membranes drop casted with 0.25 vol% suspension presented in Figures 4.9 and 4.10 were prepared by the same method, the only difference being that the former membrane had a pressure applied to the thin film after deposition while the latter membrane did not. Applying a pressure on the film after deposition did not lead to a more dense film and instead yielded cracking of the membrane. The membrane without the applied pressure did yield a dense functional layer, which shows that the packing of the particles in the deposited layer was already close enough to sinter into a dense layer. The applied pressure only caused more internal stresses in the membrane, which led to cracking and prevented the particles from sintering together.

The initial solid load in the suspensions did not make any difference in the deposited film. However, the color of the suspensions and the amount of settled powders did make a difference. The exclusion of the largest settled particles from the deposition means that the solid load in the deposited suspension is different from the initial solid load. The suspension with the lightest color, and smallest particles was the most stable suspension and yielded the most dense film. This suggests that the packing of the particles was closer, resulting in improved sintering. The amount of suspension deposited should depend on the fineness of the particles in the suspension. For the final four membranes in Table 3.6, only 1 mL of suspension was used, however, the suspensions were dark in color and settled quickly, and all of the membranes ended up with a clustered film. Therefore, a larger amount of a lighter and more stable suspension should be deposited rather than a small amount of a darker suspension.

Clustering of the film occurred in four of the prepared membranes, shown in Figures 4.11 and 4.12, where the clusters are dense and the rest of the film is porous. The clustering of the film could have occurred due to large particles in the suspensions, since the deposited suspensions were unstable and settled easily. Too large particles or agglomerates in the suspensions could have caused the deposited drops to accumulate around the large particles during drying, and therefore added more particles to the agglomerates. Alternatively, the polished support on which the dropping occurred could have had an irregular surface that caused the particles to cluster. The clusters are dense enough, which implies that if the whole surface of the supports could be covered evenly, the deposited films would be dense.

5.2 Effect of sintering temperature

5.2.1 Sintering of the membranes

The effect of sintering temperature on the density of the membranes was investigated by sintering the deposited thin films at different temperatures, all for one hour. The spray coated membrane and the membrane drop casted with the 35 vol% suspension were sintered twice. In both cases, the density was increased after the second firing. The second firing at 1450 °C resulted in a more dense film than the second firing at 1400 °C, even though the original densities of the films were approximately the same. The thickness of the film also decreased in both cases after the second firing, with the film sintered at 1450 °C shrinking more than the film sintered at 1400 °C. This shows that densification increases with increasing temperature, in compliance with Equation 2.10.

All the films sintered at 1300 °C are too porous, and the only sintering step that has occurred is necking between particles. After sintering at 1400 °C, the second sintering step, particle growth, can be seen clearly. The particles are larger and more closely together, forming a denser film. In the case where a stable suspension with small particles was added, a sintering temperature of 1400 °C was enough to densify the film completely. After sintering at 1450 °C even more particle growth occurred. Large grains are detrimental to the mechanical stability, as cracking can occur more easily in materials with large grains. Significant grain growth during sintering should therefore be avoided.

From the cross-section of the dense clusters, it can be seen that the densification has resulted in some enclosed pores in the film. Too rapid densification can entrap pores along the grain boundaries, which in turn can decrease the oxygen flux through the membrane.

The sintering of the functional layer, will also result in densification of the porous support, as can be seen from the cross-sections of the membranes. When sintering at 1300 °C this densification is insignificant. However, sintering at higher temperatures reduces the porosity of the support significantly, and measures to ensure sufficient porosity should be taken.

5.2.2 Sintering properties

The dilatometry measurements presented in Figure 4.13 indicate the temperature region that is the optimal for sintering. The optimal sintering temperature for nanocrystalline powder was found to be 1300 °C and somewhere above 1400 °C for bulk samples. Since the bulk results did not show an inflection point, the measurements should have gone further up in temperature to get an accurate reading of optimal sintering temperature. However, at temperatures above 1400 °C there is a chance of melting the material, especially the yttrium deficient samples, which is why the measurement stopped at 1400 °C. All samples show an initial increase in length of approximately 2% prior to densification, which can most likely be attributed to thermal expansion in the material.

The sample with yttrium deficiency shows a higher densification than the stoichiometric $YMn_{0.85}Ti_{0.15}O_3$ (YMTO) sample. Sintering capacity is limited by the least mobile species, which in this case is Y^{3+}. The Y-vacancies that accompany the Y-deficiency will give more available sites for the Y^{3+} ions to move between and make them more mobile. Y_2O_3 is also a refractory, so reducing the yttrium content in the sample is expected to increase the densification capability of the material. Even though Y-deficiency increases sintering, the formation of Y-vacancies can promote O-vacancies, as will be discussed in Section 5.3.2. As explained in Section 2.3, Frenkel defects involve vacancy/interstitial pairs. For oxygen defects, yttrium deficiency in the material will shift the Frenkel defect equilibrium away from the desired interstitial oxygen and towards the formation of oxygen vacancies. This will counteract the ability of the material to adsorb excess oxygen.

The nanocrystalline powder displays a higher sintering capacity than bulk material. This is as expected due to the smaller particles and higher surface area in nanocrystalline material compared to bulk. As shown in Equation 2.10, a smaller particle diameter leads to faster lattice diffusion and a higher sintering rate. The initial packing density of the nanocrystalline sample was also lower than in the bulk sample, which means that the shrinking capacity of the sample was higher.

The results from sintering the membranes at different temperatures show that when sintering the deposited nanocrystalline particles at 1300 °C, which is the optimal sintering temperature for nanoparticles according to the dilatometry measurements, the particles did not produce a dense film. Using a sintering temperature of 1400 or 1450 °C resulted in more densification and concomitant particle growth. Due to this, a sintering temperature of 1400 °C should be used to sinter the thin film. This will ensure proper densification while minimizing the grain growth compared to sintering at 1450 °C.

5.3 Crystal structure and material properties

5.3.1 Effect of Ti-doping

The processing temperature of $YMnO_3$ is usually around 1400 °C, while the temperature for unit cell tripling is around 980 °C. During cooling, the material undergoes a transition from the high-temperature $P6_3/mmc$ phase to the low-temperature $P6_3cm$ phase, which induces internal stresses in the material and can cause microcracking. The main reason for doping $YMnO_3$ with 15% titanium was to stabilize the high-temperature $P6_3/mmc$ phase at room temperature to avoid the phase transition causing unit cell tripling. The $P6_3/mmc$ phase has a higher symmetry than $P6_3cm$ and the Y-ions are in high-symmetry positions. This causes a reduction of the hexagonal c-axis. The relationship between the distance between the (hkl) planes and the 2θ angle can be seen from Bragg's law in Equation 5.1 [29].

$$d_{hkl} = \frac{n\lambda}{2\sin\theta} \tag{5.1}$$

Here d_{hkl} is the distance between the (hkl) planes, λ is the wavelength of the X-rays, θ is the incident angle of the X-rays, or Bragg angle, and n is an integer. According to Bragg's law, when the distance between planes decreases, the Bragg angle increases. The results from X-ray diffraction show that the (004) reflection has shifted to higher 2θ values for all the prepared samples. Since the (004) plane is perpendicular to the c-axis, this shift toward higher angles corresponds a decrease in the interplanar distances in the c-direction. This decrease in the c lattice parameter indicates that the samples have the high-symmetry $P6_3/mmc$ space group. The disappearance of the (012) reflection and the (014) reflection is also a characteristic sign of a trimerization and that the high-symmetry $P6_3/mmc$ phase is achieved.

The anisotropy of the thermal expansion in the material decreases with titanium doping due to a decrease in the c/a ratio of the lattice parameters, as explained in Section 2.5. The Pawley results from bulk $Y_{0.95}Ho_{0.05}Mn_{0.85}Ti_{0.15}O_3$ used in the support and the nanocrystalline $YMn_{0.85}Ti_{0.15}O_3$ (N1(800)) are compared in Table 5.1. For the space group $P6_3/mmc$ the a lattice parameter has been multiplied by $\sqrt{3}$ according to Equation 2.1 to account for the tripling of the unit cell. Results from Rietveld analysis of bulk $YMnO_3$ obtained by Frydenlund [38] are included for comparison to a stoichiometric sample. The c/a ratio for the bulk sample doped with titanium has decreased to 1.8073, compared to 1.856 for undoped $YMnO_3$. This means that the anisotropy of the thermal expansion decreases when doping the material with titanium. A decrease in the anisotropic thermal expansion is thought to decrease the amount of microcracking in the material during processing. For both the nanocrystalline and bulk material the c lattice parameter has decreased compared to the stoichiometric $YMnO_3$ sample. This is consistent with the stabilization of $P6_c/mmc$ space group.

The c/a ratios of the bulk material and nanocrystalline material should be as similar as possible in order to improve the compatibility of the support and film during heating. If the difference is too large, this can cause the support and film to expand at different rates and induce cracking of the film. The ratios shown in Table 5.1 are quite different and could cause cracking of the thin films. From the SEM images of the membranes in Section 4.2 it can be seen that most films did not have any microcracks after sintering. However, some microcracking occurred in the functional layer when the film was very thin and dense.

Table 5.1: Comparison of the results from Pawley analysis of bulk $Y_{0.95}Ho_{0.05}Mn_{0.85}Ti_{0.15}O_3$ (YHMTO) used in the support and nanocrystalline $YMn_{0.85}Ti_{0.15}O_3$ (YMTO) used in the thin film for the hexagonal space group $P6_3/mmc$. Results for stoichiometric $YMnO_3$ with space group $P6_3cm$ obtained by Frydenlund [38] are included. The hexagonal lattice parameters, a and c, and goodness of fit, R_{wp}, are listed. For space group $P6_3/mmc$ the a lattice parameter has been multiplied by $\sqrt{3}$ for direct comparison to $P6_3cm$.

Sample	**Space group**	***a* [Å]**	***c* [Å]**	**R_{wp}**	***c/a* ratio**
$Y_{0.95}Ho_{0.05}Mn_{0.85}Ti_{0.15}O_3$ bulk	$P6_3/mmc$	6.2069	11.2178	11.220	1.8073
$YMn_{0.85}Ti_{0.15}O_3$ nanocrystalline N1(800)	$P6_3/mmc$	6.1316	11.2764	6.502	1.8391
$YMnO_3$ [38] bulk	$P6_3cm$	6.1398	11.3990	8.162	1.856

Doping with Ti^{4+} on Mn^{3+}-site will require a charge compensation to make up for the extra positive charge. The charge compensation can happen either by introducing interstitial oxygen in the lattice, as described by Equation 5.2, or by reducing Mn^{3+} to Mn^{2+}, as described by Equation 5.3.

$$2\,\mathrm{TiO_2} \xrightarrow{\mathrm{YMnO_3}} 2\,\mathrm{Ti}^{\bullet}_{\mathrm{Mn}} + 3\,\mathrm{O}^{\times}_{\mathrm{O}} + \mathrm{O}''_{\mathrm{i}} \tag{5.2}$$

$$\mathrm{Mn}^{\times}_{\mathrm{Mn}} + \mathrm{TiO_2} \xrightarrow{\mathrm{YMnO_3}} \mathrm{Ti}^{\bullet}_{\mathrm{Mn}} + 2\,\mathrm{O}^{\times}_{\mathrm{O}} + \mathrm{Mn}'_{\mathrm{Mn}} \tag{5.3}$$

If the first mechanism is dominating, the composition for 15% titanium is shown in Equation 5.4, and Ti-doping aids in the incorporation of interstitial oxygen in the lattice. If the second mechanism is dominating, the resulting composition is shown in Equation 5.5 for 15% titanium.

$$\mathrm{YMn}^{3+}_{0.85}\mathrm{Ti}^{4+}_{0.15}\mathrm{O}_{3.075} \tag{5.4}$$

$$\mathrm{YMn}^{3+}_{0.70}\mathrm{Mn}^{2+}_{0.15}\mathrm{Ti}^{4+}_{0.15}\mathrm{O}_{3} \tag{5.5}$$

The amount of interstitial oxygen in a material depends on how much room there is for it in the crystal lattice. When incorporating oxygen ions into an undoped $YMnO_3$ lattice, they can take one of two interstitial sites, either the (1/3,1/3,0) site, or the (2/3,2/3,1/2) as shown in Figure 5.1. When an oxygen ion goes into a site, it is surrounded by three Mn-ions and will oxidize two of these to Mn^{4+}. For another oxygen ion to go into one of the neighboring sites, it would have to oxidize one of the already oxidized Mn^{4+} ions to Mn^{5+}. This is not very likely to occur, and the oxygen ions will most likely go into the adjacent Mn-O plane. This gives a maximum of $\delta = 0.33$. [41]

When one of the Mn^{3+} ions is substituted with Ti^{4+}, another Mn^{3+} is reduced to Mn^{2+}, as shown in Figure 5.2a. This means that if an interstitial oxygen is introduced to the Ti-doped lattice, as shown in Figure 5.2b, the interstitial oxygen could oxidize one Mn^{3+} to Mn^{4+} and one Mn^{2+} to Mn^{3+}. This can in turn lead to the possibility of another oxygen interstitial going into a neighboring site and oxidizing two Mn^{3+} to Mn^{4+}, thus increasing the ability of the material to accommodate oxygen.[41]

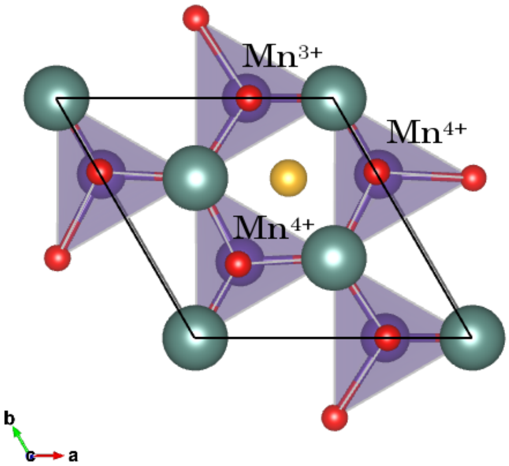

Figure 5.1: Hexagonal $YMnO_3$ with space group $P6_3cm$ with interstitial oxygen ion (yellow). Green spheres represent Y^{3+}, purple represent Mn^{3+}, and red represent O^{2-}. The figure is made using the VESTA software [23] using lattice sites obtained from Gibbs et al. [18].

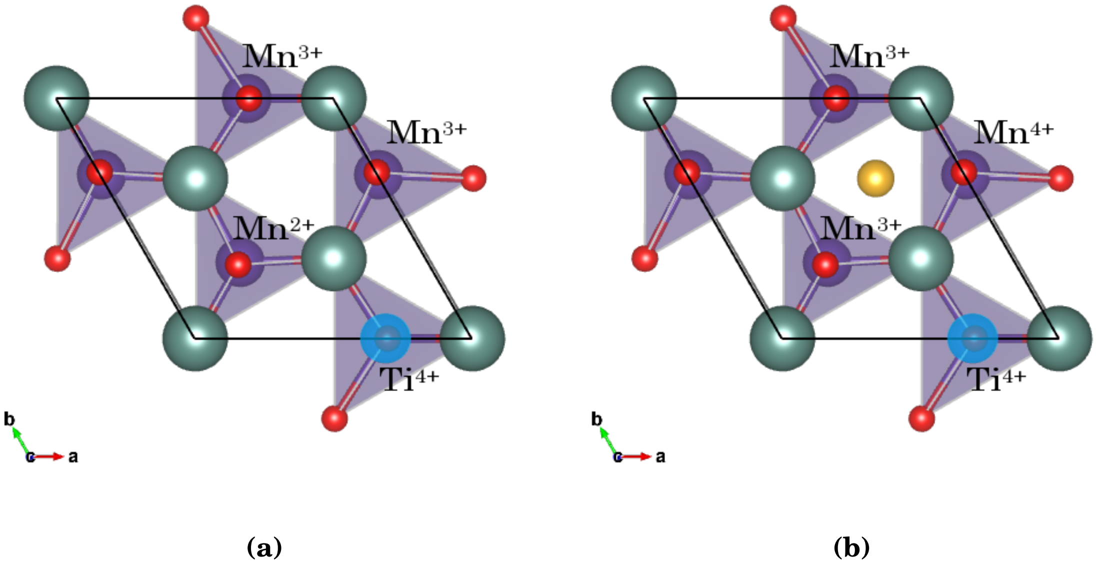

(a) **(b)**

Figure 5.2: Hexagonal $YMnO_3$ with space group $P6_3cm$ doped with Ti^{4+} (blue) on Mn-site. (a) Ti-doped $YMnO_3$, (b)Ti-doped $YMnO_3$ with interstitial oxygen ion (yellow). Green spheres represent Y^{3+}, purple represent Mn^{3+}, and red represent O^{2-}. The figure is made using the VESTA software [23] using lattice sites obtained from Gibbs et al. [18].

5.3.2 Effect of Y-deficiency

When introducing yttrium deficiency in the material, each Y-vacancy will have to be charge compensated by three positive charges. This can be done in three ways: i) by the formation of oxygen vacancies, ii) by the oxidation of some Mn^{3+} to Mn^{4+}, or iii) by some of the Mn ions going into Y-sites, either by Mn^{3+} going into Y^{3+}-sites or by reduced Mn^{2+} going into Y^{3+}-sites and forming oxygen vacancies. Combining these charge compensating reactions with the possible charge compensating reactions from Ti-doping, will give a lot of possible compositions, so for simplicity it is assumed that the titanium charge compensation shown in Equation 5.3 is dominating. If this is the case, the charge compensation for 15% Y-deficiency and 15% Ti-doping will give the compositions shown in Equations 5.6 and 5.7 for i) and ii), respectively.

$$Y^{3+}_{0.85}Mn^{3+}_{0.70}Mn^{2+}_{0.15}Ti^{4+}_{0.15}O_{3-0.225} \tag{5.6}$$

$$Y^{3+}_{0.85}Mn^{3+}_{0.55}Mn^{4+}_{0.30}Ti^{4+}_{0.15}O_{3} \tag{5.7}$$

If only 5% Y-deficiency is introduced, the excess positive charge caused by 15% Ti-doping will be all the charge compensation needed to compensate for the yttrium deficiency. The resulting composition will be $Y^{3+}_{0.95}Mn^{3+}_{0.85}Ti^{4+}_{0.15}O_3$.

For the final possible charge compensation, Mn ions can go into vacant Y-sites, either as Mn^{3+} or as reduced Mn^{2+}, which in turn will create oxygen vacancies. The latter will result in the mechanism presented in Equation 5.8.

$$Mn_2O_3 \xrightarrow{YMnO_3} 2\,Mn'_Y + 2\,O^{\times}_O + V^{\bullet\bullet}_O + \frac{1}{2}\,O_2(g) \tag{5.8}$$

Introducing yttrium deficiency in the material yields no apparent changes in the X-ray diffraction, as shown in Figure 4.1. The results from Pawley analysis presented in Table 4.1 show that the high-symmetry space group $P6_3/mmc$ gives the best fit for $YMn_{0.85}Ti_{0.15}O_3$ (YMTO) and $Y_{0.95}Mn_{0.85}Ti_{0.15}O_3$ (Y095MTO), while the $P6_3cm$ space group gives the best fit for $Y_{0.90}Mn_{0.85}Ti_{0.15}O_3$ (Y090MTO) and $Y_{0.85}Mn_{0.85}Ti_{0.15}O_3$ (Y085MTO). There is no apparent reason for this shift in stability for the Pawley analysis. When looking at the XRD results in Figure 4.1, it can be seen that the (012) reflection is missing for all samples, suggesting that all samples have the high-symmetry $P6_3/mmc$ phase, and not the $P6_3cm$ phase. This means that the lattice parameters calculated for the space group $P6_3/mmc$ are most likely to give a better indication on the effect of Y-deficiency on the lattice. From these values it can be seen that the *c* lattice parameter increases with increasing Y-deficiency and thus counteracts the decrease in the *c*-direction caused by Ti-doping. An increase in *c* parameter will cause an increase in the *c/a* ratio and consequently an increase in the anisotropy in thermal expansion as well as a larger chance of microcracking.

5.3.3 Oxygen non-stoichiometry

The incorporation of interstitial oxygen into the lattice can be charge compensated either by the oxidation of Mn^{3+} to Mn^{4+}, by the formation of oxygen vacancies, or by doping the material with a higher-valent ion, as explained in Section 2.3. The positive Seebeck coefficient of the material [30] suggests that interstitial oxygen is the main defect, which makes it possible to assume that oxidation of Mn^{3+} to Mn^{4+} is the main charge compensating reaction and not the formation of oxygen vacancies. The incorporation of oxygen ions by oxidation of Mn^{3+} is revisited in Equation 5.9.

$$\delta/2\,\mathrm{O_2(g)} + 2\,\delta\,\mathrm{Mn}_{\mathrm{Mn}}^{\times} \xrightleftharpoons{\mathrm{YMnO_3}} \delta\,\mathrm{O}_{\mathrm{i}}'' + 2\,\delta\,\mathrm{Mn}_{\mathrm{Mn}}^{\bullet} \tag{5.9}$$

As explained in Section 2.3, the concentration of interstitial oxygen is favored up to a certain temperature, due to the negative entropy accompanying the incorporation of oxygen from the atmosphere into the lattice. At higher temperatures, the Gibbs free energy becomes positive, forcing the above reaction to go to the left, and interstitial ions to leave the lattice. This can be seen experimentally by the results from thermogravimetric analysis (TGA), where the material is oxidized up to a temperature around 350 °C at which point reduction starts. From this temperature, the adsorbed oxygen leaves the material. This result further supports the assumption that the oxidation of Mn^{3+} is the main charge compensating reaction.

To determine if titanium doped hexagonal $YMnO_3$ is a suitable material for use in an oxygen permeable membrane, the ability of the material to adsorb oxygen must be investigated. This can be done by interpreting the mass change in the TGA results shown in Figure 4.14 in terms of oxygen stoichiometry, $3+\delta$, where δ is excess interstitial oxygen. In order to calculate the $3+\delta$ values for oxygen stoichiometry in the material, a starting value where $\delta = 0$ must be determined. The amount of adsorbed oxygen and water or other gases in the samples at room temperature is unknown. However, at 600 °C it is reasonable to assume that most of the impurities and adsorbed oxygen has left the sample, as long as the curve has flattened. In the results in Figure 4.14, the curve still has a negative slope, but this was still determined to be the best assumption to make in order to determine oxygen stoichiometry. Based on this assumption the value of $\delta = 0$ was assumed to be the mass at 600 °C during the slow heating cycle. However, the true value of $\delta = 0$ is most likely at a lower mass. The resulting oxygen stoichiometry is presented in Figure 5.3.

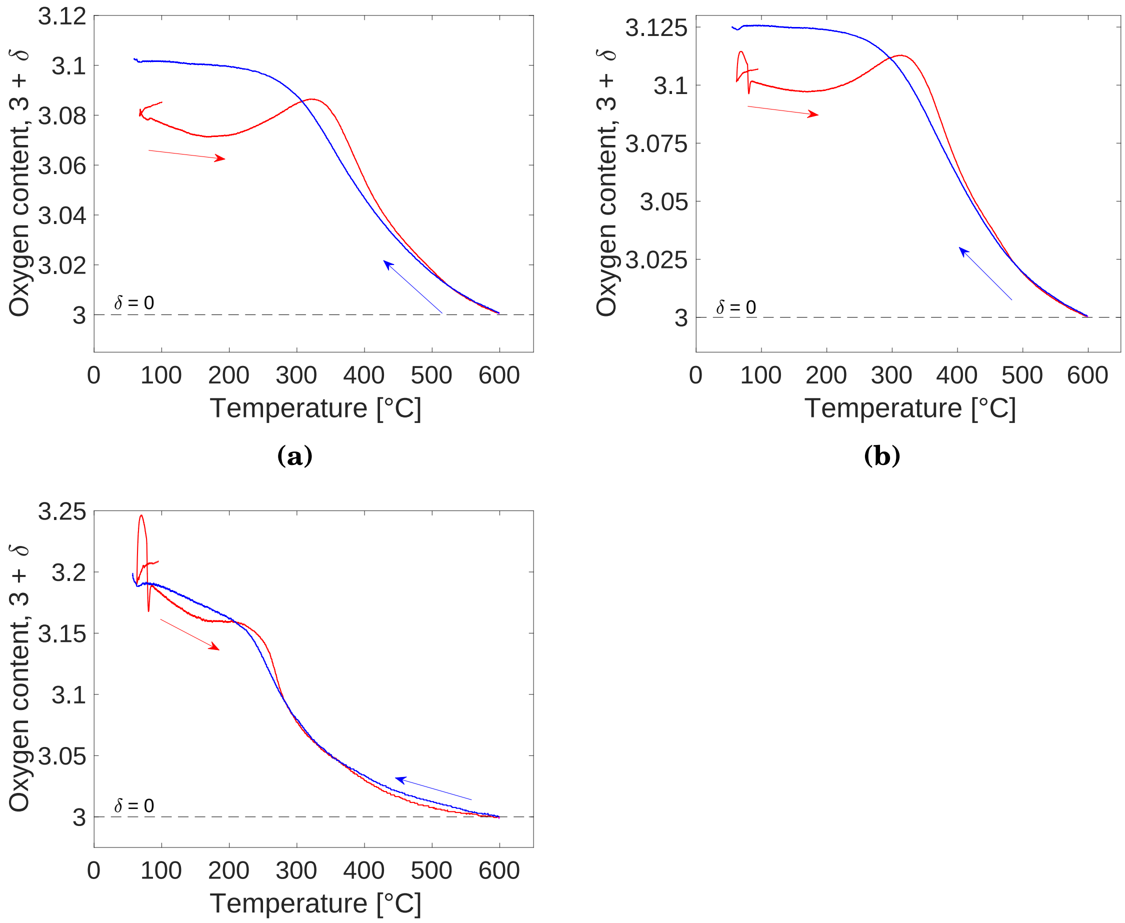

(a)

(b)

(c)

Figure 5.3: Results from thermogravimetric analysis with heating and cooling rate of 1 °C/min. The change in oxygen content is given as $3+\delta$ where the mass at 600 °C was chosen as $\delta = 0$. The red lines indicate heating and the blue lines indicate cooling. (a) bulk $YMn_{0.85}Ti_{0.15}O_3$, (b) bulk $Y_{0.95}Mn_{0.85}Ti_{0.15}O_3$, and (c) nanocrystalline $YMn_{0.85}Ti_{0.15}O_3$ fired at 900 °C.

The second heating cycle was conducted with a slower heating and cooling rate (1 °C/min) than the initial heating cycle, thus having more time to reach equilibrium. Therefore, the oxygen contents in the samples have been calculated only for the second heating cycles. The oxygen stoichiometry can be seen in Figures 5.3a and 5.3b, for bulk $YMn_{0.85}Ti_{0.15}O_3$ (YMTO) and $Y_{0.95}Mn_{0.85}Ti_{0.15}O_3$ (Y095MTO), respectively, and in Figure 5.3c for nanocrystalline $YMn_{0.85}Ti_{0.15}O_3$. The cooling rate of the second cycle gives the most accurate indication to the ability of $YMn_{0.85}Ti_{0.15}O_3$ to adsorb oxygen, as impurities will have evaporated and the cooling rate is slow enough to almost reach equilibrium.

The oxygen uptake for bulk YMTO was up to $\delta = 0.10$, for bulk Y095MTO $\delta = 0.125$, and for nanocrystalline YMTO $\delta = 0.20$. Since the thermogravimetric curves did not reach equilibrium at the higher temperatures, where $\delta = 0$ was defined, the true δ values are probably somewhat higher than stated. These δ values are quite low compared to the ones found for $YMnO_3$ by Abughayada et al. [17], where the excess oxygen content was found to be up to $\delta = 0.3$. However, in those measurements the heating and cooling rate was 0.1 °C/min, so the values cannot be compared directly. The calculated values of δ are in the same range as the values for bulk $YMn_{0.85}Ti_{0.15}O_3$ found by Østli [41], where $\delta \approx 0.17$ and the heating and cooling rate was 1 °C/min. Østli also found that nanocrystalline $YMn_{0.85}Ti_{0.15}O_3$ could incorporate oxygen up to $\delta = 0.45$, but these results were not reproduced in this study. For the thermogravimetric measurements to reach equilibrium, slower heating and cooling rates are needed. Alternately, to ensure that $\delta = 0$ has been reached, the measurements could go to higher temperatures.

The oxygen uptake of $Y_{0.95}Mn_{0.85}Ti_{0.15}O_3$ is larger than that of the stoichiometric $YMn_{0.85}Ti_{0.15}O_3$, which is unexpected due to the possible charge compensating reactions presented in Section 5.3.2. If these results are correct, 5% Y-deficiency could lead to both increased sintering properties and increased oxygen adsorption and would be very beneficial for the intended application. The oxygen uptake of Y-deficiency in Ti-doped material should therefore be investigated further.

The temperature range where the most oxygen is incorporated into the lattice is where the change in oxidation, $\Delta\delta$, is the largest. This temperature range will give an indication to the optimal operating temperature for use in an oxygen permeable membrane. $\Delta\delta$ was largest in the temperature range 200–400 °C for bulk material, and in the range 150–300 °C for nanocrystalline material. This suggests possible operating temperatures much lower than for the state-of-the-art perovskites, which usually require operating temperatures above 600 °C [7]. Ti-doped $YMnO_3$ is therefore a very promising material for oxygen permeable membranes used at low temperatures, and will be much more environmentally friendly.

Kinetics of oxygen adsorption

The rate of oxygen exchange with the atmosphere can be controlled by either surface exchange or bulk diffusion, as explained in Section 1.1. Therefore, reducing the necessary bulk diffusion of the oxygen ions will increase the exchange rate. The particle sizes in the sample will therefore affect the kinetics of oxygen adsorption. The oxygen uptake in the nanocrystalline material is larger than in the bulk samples, with an oxygen stoichiometry up to $\delta = 0.2$, compared to $\delta = 0.1$ for bulk YMTO. The nanocrystalline material has more surface area available for the dissociation and adsorption of oxygen, and it is therefore reasonable to assume that it will be able to adsorb more oxygen and at a higher rate than bulk material. The results in Figure 5.3 are in agreement with this.

The effects of temperature on the thermodynamics of the oxygen uptake in the samples was explained previously, where the defect concentration is favored up to a certain temperature. Temperature can also affect the kinetics of the the oxygen uptake. The conductivity, σ, of a material is given by Equation 5.10, where n is the number of current carriers, e is the charge of the current carriers, and μ is their mobility [29].

$$\sigma = ne\mu \tag{5.10}$$

In hexagonal $YMnO_3$, interstitial oxygen is the main charge carrier. The mobility, μ, of the interstitial oxygen is dependent of temperature as explained by the Arrhenius equation given in Equation 5.11 [29].

$$\mu = \mu_0 \exp\left(-\frac{E}{RT}\right) \tag{5.11}$$

Here E is the activation energy for the ion migration, R is the gas constant and T is temperature. From this equation it can be seen that when the temperature increases, so does the mobility of the interstitial oxygen. Thus, the rate of oxygen incorporation in the lattice increases with temperature.

Doping with titanium will affect the stability of the $P6_3/mmc$ phase of the material, which will give a more open and symmetric structure than the $P6_3cm$ phase. According to Equation 5.2, introducing Ti^{4+} in the lattice can lead to interstitial oxygen as a charge compensating reaction. It is therefore possible that titanium doping can facilitate a higher incorporation of oxygen than undoped $YMnO_3$.

5.4 Further work

The production parameters of the asymmetrical membrane should be further investigated to optimize the fabrication route and produce a functioning membrane. The most crucial step is densification of the thin film, and controlling the porosity and mechanical strength of the support.

5.4.1 Production of porous support

Due to the densification of the support during sintering of the thin film, a pore former should be added during the production of the support to ensure sufficient porosity through the entire fabrication route of the membrane. The mechanical integrity of the support should be maintained, but this involves a trade-off with increased porosity. The use of 30 wt% pore former is suggested, based on the work performed by Wagner [42]. The porosity of the support should be investigated by the Archimedes method in order to have a better control of the degree of porosity in the support and to be able to make reproducible results.

5.4.2 Preparation of stable suspensions

The suspension used for deposition of the thin film should be stable and contain only small particles with a narrow particle distribution. This should be done in order to achieve a closer packing of the deposited particles and an increased sintering of the thin film. This is believed to be the most critical step in the fabrication process. To achieve small particles the nanocrystalline material produced by the citric acid method should be ball milled prior to being dispersed in the suspension. The particle size distribution should also be tested to ensure a narrow size distribution. The stability of the suspensions could also be increased by adding a surfactant. Stability testing of the suspensions could be performed, and the effect of depositing a stable suspension on the resulting thin film could be investigated.

5.4.3 Preparation of the asymmetrical membrane

Drop casting proved to be the most promising deposition method, and should be investigated further. The amount of suspension needed is dependent on the size of the particles in the suspension, and should be investigated. The surfaces of the supports should be carefully polished to make sure an even and smooth surface is achieved. Dip coating is the simplest deposition method. However, if dip coating is to be used for deposition, the stability of the suspension must be increased. A good starting point would be to use the preparation method applied by Østli, using a surfactant and ball milling of the suspension [41]. The most promising sintering temperature of the deposited thin films appears to be 1400 °C, as much densification occurs at this temperature, while the grain growth is limited compared to higher temperatures.

5.4.4 Chemical composition

The doping of hexagonal $YMnO_3$ with 15% titanium resulted in a successful stabilization of the $P6_3/mmc$ phase, and should be included in both the functional layer and the support in further work. 5% Y-deficiency can also be introduced in the lattice to improve the sintering properties of the material, and possibly also to increase the oxygen uptake of the sample. Y-deficiency should only be introduced in the nanocrystalline powder used in the functional layer, and not in the support, since further sintering of the support is not desired. Another possibility is adding 1-2% Y-deficiency, which will be charge compensated by 3-6% of the titanium, with respect to the Frenkel equilibrium between oxygen vacancies and interstitials. Adding 5% holmium to the support is not necessary unless there is a problem with distinguishing the film from the support however, this has not been a problem in the present work.

5.4.5 Investigation of oxygen adsorption

The accommodation of interstitial oxygen in the lattice should be further investigated by TGA measurements. They should be performed with a slower heating and cooling rate and a longer dwell time in order to achieve equilibrium. Also, the measurements could go to a higher temperature to reach equilibrium at an increased rate. The oxygen uptake of yttrium deficient material should be examined further. The reversibility of the oxygen uptake in the material can be investigated by TGA measurements in changing atmosphere between O_2 and N_2. In order to determine the oxygen stoichiometry of the samples and the value of δ more accurately and the, coulometric titration can be performed to find the absolute oxygen content in the material.

If a dense, crack-free film is achieved and the porosity of the support is sufficient for gas flow, the oxygen flux through the membrane should be investigated.

Chapter 6

Conclusion

A fabrication route for an asymmetrical mixed ionic-electronic conducting membrane based on hexagonal $YMnO_3$ doped with 15% titanium was investigated. Yttrium deficiency was also introduced in the material to investigate its effect on sintering properties and oxygen adsorption. The solid state method was used to produce the porous support, and the citric acid method was used to make the nanocrystalline material. The nanoparticles were dispersed in a suspension and deposited onto the support by spray coating, dip coating and drop casting. The membranes were then sintered and the resulting microstructures investigated. The most critical processing step was achieving a dense thin film on top of a porous support.

A dense thin film was achieved by drop casting a support with a suspension with small particles and sintering at 1400 °C for one hour. The film had some microcracks and flaking at the edges of the membrane. Spray coating and dip coating did not yield dense films. Overall, drop casting was found to give the most promising results.

The produced samples were found to have the desired hexagonal $P6_3/mmc$ space group. Doping with titanium decreased the lattice parameter in the c-direction, reducing the anisotropy of the thermal expansion in the material. This will in turn reduce the internal stresses in the material during processing, which leads to microcracking. Y-deficiency was found to improve the sintering properties of the material, with an optimal sintering temperature of 1400 °C. The excess oxygen in the lattice was measured and found to be largest in the temperature range 150–300 °C for nanocrystalline material, with an oxygen uptake of $\delta = 0.20$. Based on these findings, titanium doped hexagonal $YMnO_3$ is a very promising material for use in membranes for oxygen separation from air.

Bibliography

[1] S. M. Hashim, A. R. Mohamed, and S. Bhatia. “Current status of ceramic-based membranes for oxygen separation from air”. *Adv. Colloid Interface Sci.* 160 (2010), 88–100.

[2] D. D. Athayde, D. F. Souza, A. M. Silva, D. Vasconcelos, E. H. Nunes, J. C. Diniz da Costa, and W. L. Vasconcelos. “Review of perovskite ceramic synthesis and membrane preparation methods”. *Ceram. Int.* 42 (2016), 6555–6571.

[3] P. V. Hendriksen, P. H. Larsen, M. Mogensen, F. W. Poulsen, and K. Wiik. “Prospects and problems of dense oxygen permeable membranes”. *Catal. Today* 56 (2000), 283–295.

[4] R. Stanger, T. Wall, R. Spörl, M. Paneru, S. Grathwohl, M. Weidmann, G. Scheffknecht, D. McDonald, K. Myöhänen, J. Ritvanen, S. Rahiala, T. Hyppänen, J. Mletzko, A. Kather, and S. Santos. “Oxyfuel combustion for CO_2 capture in power plants”. *Int. J. Greenh. Gas Control* 40 (2015), 55–125.

[5] B. S. P. S. Badwal and F. T. Ciacchi. “Ceramic membranes for oxygen separation”. *Membr. Technol.* 2001 (2001), 16.

[6] K. Zhang, J. Sunarso, Z. Shao, W. Zhou, C. Sun, S. Wang, and S. Liu. “Research progress and materials selection guidelines on mixed conducting perovskite-type ceramic membranes for oxygen production”. *RSC Adv.* 1 (Nov. 2011), 1661.

[7] J. Sunarso, S. Baumann, J. Serra, W. Meulenberg, S. Liu, Y. Lin, and J. Diniz da Costa. “Mixed ionic–electronic conducting (MIEC) ceramic-based membranes for oxygen separation”. *J. Memb. Sci.* 320 (July 2008), 13–41.

[8] A. Thursfield and I. S. Metcalfe. “The use of dense mixed ionic and electronic conducting membranes for chemical production”. *J. Mater. Chem.* 14 (2004), 2475–2485.

[9] H. J. M. Bouwmeester, H. Kruidhof, and A. J. Burggraaf. “Importance of the surface exchange kinetics as rate limiting step in oxygen permeation through mixed-conducting oxides”. *Solid State Ionics* 72 (1994), 185–194.

[10] Y.-S. Lin, W. Wang, and J. Han. “Oxygen permeation through thin mixed-conducting solid oxide membranes”. *AIChE J.* 40 (1994), 786–798.

[11] H. J. M. Bouwmeester. “Dense ceramic membranes for methane conversion”. *Catal. Today* 82 (2003), 141–150.

[12] F. Schulze-Küppers, S. Baumann, F. Tietz, H. J. M. Bouwmeester, and W. A. Meulenberg. “Towards the fabrication of $La_{0.98\text{-}x}Sr_xCo_{0.2}Fe_{0.8}O_{3\text{-}\delta}$ perovskite-type oxygen transport membranes”. *J. Eur. Ceram. Soc.* 34 (2014), 3741–3748.

[13] X. Chang, C. Zhang, Y. He, X. Dong, W. Jin, and N. Xu. “A Comparative Study of the Performance of Symmetric and Asymmetric Mixed-conducting Membranes”. *Chinese J. Chem. Eng.* 17 (2009), 562–570.

[14] J. Da Costa, S. Smart, J. Motuzas, L. Shaomin, and D. Zhang. “State of Art (SOTA) Report on Dense Ceramic Membranes for Oxygen Separation from Air” (2013), 1–13.

[15] P. Lemes-Rachadel, G. Sachinelli, R. Antonio, and F. Machado. “Current Developments of Mixed Conducting Membranes on Porous Substrates”. 17 (2014), 242–249.

[16] S. Remsen and B. Dabrowski. “Synthesis and oxygen storage capacities of hexagonal $Dy_{1\text{-}x}Y_xMnO_{3+d}$”. *Chem. Mater.* 23 (2011), 3818–3827.

[17] C. Abughayada, B. Dabrowski, S. Kolesnik, D. E. Brown, and O. Chmaissem. “Characterization of Oxygen Storage and Structural Properties of Oxygen-Loaded Hexagonal $RMnO_{3+\delta}$ (R = Ho, Er, and Y)”. *Chem. Mater.* 27 (Sept. 2015), 6259–6267.

[18] A. Gibbs, K. Knight, and P. Lightfoot. “High-temperature phase transitions of hexagonal $YMnO_3$”. *Phys. Rev. B* 83 (2011), 1–9.

[19] B. B. Van Aken, T. T. M. Palstra, A. Filippetti, and N. a. Spaldin. “The origin of ferroelectricity in magnetoelectric $YMnO_3$.” *Nat. Mater.* 3 (2004), 164–170.

[20] S. Dong, J.-M. Liu, S.-W. Cheong, and Z. Ren. “Multiferroic materials and magnetoelectric physics: symmetry, entanglement, excitation, and topology”. *Adv. Phys.* 64 (2015), 519–626.

[21] S. M. Selbach, A. Nordli Løvik, K. Bergum, J. R. Tolchard, M.-A. Einarsrud, and T. Grande. “Crystal structure, chemical expansion and phase stability of $HoMnO_3$ at high temperature”. *J. Solid State Chem.* 196 (2012), 528–535.

[22] K. Bergum, H. Okamoto, H. Fjellvåg, T. Grande, M.-A. Einarsrud, and S. M. Selbach. “Synthesis, structure and magnetic properties of nanocrystalline $YMnO_3$.” *Dalton Trans.* 40 (2011), 7583–7589.

[23] K. Momma and F. Izumi. “VESTA 3 for three-dimensional visualization of crystal, volumetric and morphology data”. *J. Appl. Crystallogr.* 44 (Oct. 2011), 1272–1276.

[24] M. Lilienblum, T. Lottermoser, S. Manz, S. M. Selbach, A. Cano, and M. Fiebig. “Ferroelectricity in the multiferroic hexagonal manganites”. *Nat. Phys.* (2015).

[25] J.-W. G. Bos, B. B. van Aken, and T. T. M. Palstra. “Site Disorder Induced Hexagonal-Orthorhombic Transition in $Y_{1-x}Gd_xMnO_3$”. *Chem. Mater.* 13 (2001), 4804–4807.

[26] R. D. Shannon. “Revised Effective Ionic Radii and Systematic Studies of Interatomic Distances in Halides and Chalcogenides”. *Acta. Cryst.* (1976).

[27] A. Kjekshus. “Synthesis of Metastable Perovskite-type $YMnO_3$ and $HoMnO_3$”. *J. Solid State Chem.* 340 (1997), 334–340.

[28] M. Chen, B. Hallstedt, and L. J. Gauckler. “Thermodynamic assessment of the Mn-Y-O system”. *J. Alloys Compd.* 393 (2005), 114–121.

[29] A. R. West. *Solid State Chemistry and its Applications*. Wiley, 2014.

[30] S. H. Skjærvø, E. T. Wefring, S. K. Nesdal, N. H. Gaukås, G. H. Olsen, J. Glaum, T. Tybell, and S. M. Selbach. “Interstitial Oxygen as a Source of p-type Conductivity in Hexagonal Manganites” (Submitted 2016).

[31] H. L. Lein. “Mechanical Properties and Phase Stability of Oxygen Permeable Membranes $La_{0.5}Sr_{0.5}Fe_{1-x}Co_xO_{3-\delta}$”. PhD thesis. 2005.

[32] M. Tomczyk, A. M. Senos, P. M. Vilarinho, and I. M. Reaney. “Origin of microcracking in $YMnO_3$ ceramics”. *Scr. Mater.* 66 (2012), 288–291.

[33] M. Tomczyk, A. M. Senos, I. M. Reaney, and P. M. Vilarinho. “Reduction of microcracking in $YMnO_3$ ceramics by Ti substitution”. *Scr. Mater.* 67 (2012), 427–430.

[34] T. Asaka, K. Nemoto, K. Kimoto, T. Arima, and Y. Matsui. “Crystallographic superstructure of Ti-doped hexagonal $YMnO_3$”. *Phys. Rev. B* 71 (Jan. 2005), 014114.

[35] L. E. Smart and E. A. Moore. *Solid State Chemistry: An Introduction, Third Edition*. 2005.

[36] D. W. Richerson. *Modern Ceramic Engineering: Properties, Processing, and Use in Design, Third Edition*. Boca Raton, FL: CRC Press, 2006.

[37] R. J. D. Tilley. *Understanding Solids: The Science of Materials*. John Wiley & Sons, 2013, 576.

[38] M. M. Frydenlund. "Development of a new class of oxygen ion mixed conductors." Master's thesis. NTNU. 2014.

[39] S. M. Hoggen. "Development of oxygen-permeable membranes based on hexagonal manganites". Specialization project. NTNU. 2016.

[40] Y. Noda, Y. Fukuda, and H. Kimura. "Review and prospect of ferroelectricity and magnetism in YMn_2O_5". *J. Korean Phys. Soc.* 42 (2003), 1192–1195.

[41] E. R. Østli. "Optimization of chemical composition of novel manganite oxides for oxygen permeable membranes". Master's thesis. NTNU. 2015.

[42] N. Wagner. "Permeation and Stability Properties of Asymmetric and Disk Shaped Oxygen Permeable Membranes Intended for Syn-Gas Production". Master's thesis. NTNU. 2012.

Appendices

Appendix A

Standardization of precursors

The results from the standardization of the Y^{3+}, Mn^{3+}, and Ti^{4+} precursors prepared for the citric acid method are given in this appendix. The molality of each precursor was calculated based on the weight of the crucibles and Kaowool before adding the precursor solution, after adding the precursor solution, and after heat treatment resulting in the oxides Y_2O_3, Mn_2O_3, and TiO_2, respectively. The weights of the three crucibles that were used to calculate the molality of the precursors are presented in Table A.1. The precursor molality calculations based on the standardization results are presented in Table A.2.

Table A.1: The weights resulting from the standardization of the Y^{3+}, Mn^{3+}, and Ti^{4+} precursor solutions.

	Weight [g]	**Weight [g]**	**Weight [g]**	**Weight [g]**	**Weight [g]**
Crucible	**Crucible +wool**	**Crucible +wool +solution**	**Crucible +wool +oxide**	**Solution**	**Oxide**
Y^{3+} prec.					**Y_2O_3**
1	14.1820	16.3145	14.1924	2.1325	0.0104
2	13.9769	16.1521	13.9861	2.1761	0.0101
3	13.8869	16.0194	13.8967	2.1325	0.0098
Mn^{3+} prec.					**Mn_2O_3**
1	14.0074	16.1700	14.0131	2.1626	0.0057
2	13.8529	16.0615	13.8585	2.2086	0.0056
3	14.5095	16.6341	14.5150	2.1246	0.0055
Ti^{4+} prec.					**TiO_2**
1	15.0068	17.0044	15.0184	1.9976	0.0116
2	14.2613	16.1391	14.2730	1.8778	0.0117
3	14.7944	16.7959	14.8068	2.0015	0.0124

Table A.2: The calculation of the molality of the Y^{3+}, Mn^{3+}, and Ti^{4+} precursor solutions based on the standardization. The molar masses used for the calculations were 225.81 g/mol, 157.87 g/mol, and 79.87 g/mol for Y_2O_3, Mn_2O_3, and TiO_2, respectively.

	Weight [g]	***n* [mol]**	***n* [mol]**	**Molality [mmol/g]**	**Average molality [mmol/g]**
Crucible	**Oxide**	**Oxide**	**Ion**	**Ion**	**Ion**
Y^{3+} prec.	**Y_2O_3**	**Y_2O_3**	**Y^{3+}**	**Y^{3+}**	
1	0.0104	4.61×10^{-5}	9.21×10^{-5}	0.0432	
2	0.0101	4.47×10^{-5}	8.95×10^{-5}	0.0411	
3	0.0098	4.40×10^{-5}	8.68×10^{-5}	0.0407	0.0417(13)
Mn^{3+} prec.	**Mn_2O_3**	**Mn_2O_3**	**Mn^{3+}**	**Mn^{3+}**	
1	0.0057	3.61×10^{-5}	7.22×10^{-5}	0.0340	
2	0.0056	3.55×10^{-5}	7.09×10^{-5}	0.0321	
3	0.0055	3.48×10^{-5}	6.97×10^{-5}	0.0328	0.0328(6)
Ti^{4+} prec.	**TiO_2**	**TiO_2**	**Ti^{4+}**	**Ti^{4+}**	
1	0.0116	1.45×10^{-4}	1.45×10^{-4}	0.0727	
2	0.0117	1.46×10^{-4}	1.46×10^{-4}	0.0780	
3	0.0124	1.55×10^{-4}	1.55×10^{-4}	0.0776	0.0761(29)

Appendix B

Temperature programs for dilatometry and TGA

The temperature programs used for analyzing bulk $YMn_{0.85}Ti_{0.15}O_3$ and $Y_{0.95}Mn_{0.85}Ti_{0.15}O_3$, and nanocrystalline $YMn_{0.85}Ti_{0.15}O_3$ by dilatometry and thermogravimetric analysis (TGA) are presented in this appendix. The dilatometry temperature program is shown in Table B.1. The temperature program for TGA in oxygen atmosphere is presented in Table B.2.

Table B.1: The temperature program used for dilatometry analysis.

Step	T_{initial} **[°C]**	**Ramp [°C/min]**	T_{end} **[°C]**	**Dwell time [min]**	**Atmosphere**	**Flow [mL/min]**
1	30	2	1400	-	Synthetic air	20-30
2	1400	-	1400	1	Synthetic air	20-30
3	1400	10	30	-	Synthetic air	20-30

Table B.2: The temperature program used for thermogravimetric analysis in oxygen atmosphere.

Step	T_{initial} **[°C]**	**Ramp [°C/min]**	T_{end} **[°C]**	**Dwell time [min]**	**Atmosphere**	**Flow [mL/min]**
1	30	10	600	-	O_2	20-30
2	600	-	600	10	O_2	20-30
3	600	10	30	-	O_2	20-30
4	30	1	600	-	O_2	20-30
5	600	-	600	60	O_2	20-30
6	600	1	30	-	O_2	20-30

Appendix C

X-ray diffractograms and Pawley refinements

C.1 Standardization of precursors

The oxides resulting from standardization of the Y^{3+}, Mn^{3+}, and Ti^{4+} precursor solutions were analyzed by X-ray diffraction in order to ensure that the correct oxide had been obtained. The diffractograms are presented in Figures C.1, C.2, and C.3 for Y_2O_3, Mn_2O_3, and TiO_2, respectively. The results were matched to characteristic diffraction lines by the software DIFFRAC.EVA v4.1 corresponding to the PDF cards 00-005-0574, 03-065-1798, and 00-021-1276, respectively, shown as black bars in the figures. The impurity peaks found in the diffractogram of TiO_2 were found to correspond to the Kaowool used during standardization.

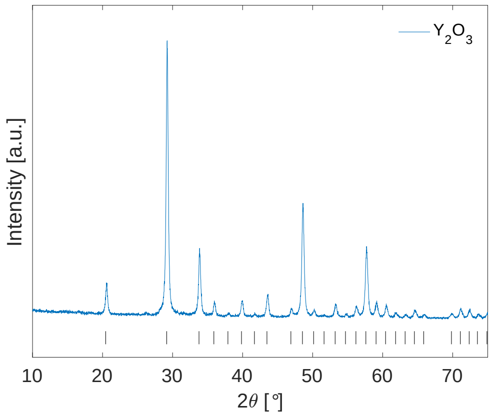

Figure C.1: The X-ray diffraction results for Y_2O_3 resulting from standardization of the Y^{3+} precursor. The characteristic lines from PDF card 00-005-0574 are shown as black bars in the figure.

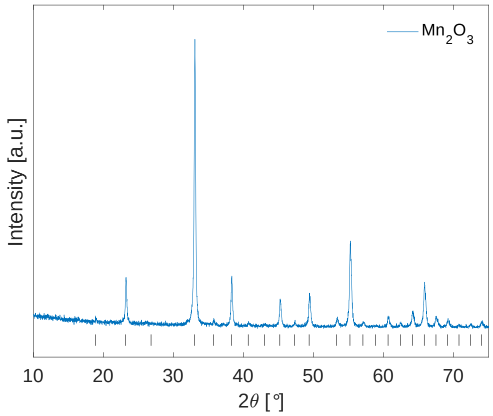

Figure C.2: The X-ray diffraction results for Mn_2O_3 resulting from standardization of the Mn^{3+} precursor. The characteristic lines from PDF card 03-065-1798 are shown as black bars in the figure.

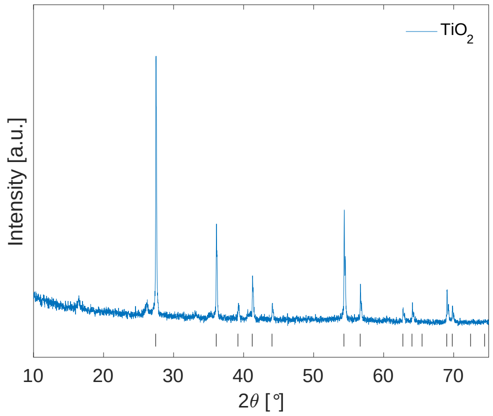

Figure C.3: The X-ray diffraction results for TiO_2 resulting from standardization of the Ti^{4+} precursor. The characteristic lines from PDF card 00-021-1276 are shown as black bars in the figure.

C.2 Pawley refinement of nanocrystalline powder

Since one nanocrystalline sample, N1(800), showed a small signal from the orthorhombic YMn_2O_5, another Pawley refinement was performed that combined the hexagonal space group $P6_3cm$ with the orthorhombic space group $Pbam$. The resulting lattice parameters for both space groups are presented in Table C.1. The hexagonal lattice parameters are approximately the same as when not including the orthorhombic phase in the refinement, however, the fit for the refinement is much better when including the orthorhombic phase, with $R_{\mathrm{wp}} = 3.033$ versus $R_{\mathrm{wp}} = 6.277$ as shown in Table 4.2.

Figure C.4a shows the measured data, the refined data, and the difference between the refined and the measured data, when only space groups $P6_3cm$ is included in the refinement. Figure C.4b shows the measured data, the refined data, and the difference between the refined and the measured data, when both space groups $P6_3cm$ and $Pbam$ are included in the refinement. It can be seen that the fit is much better when including the orthorhombic phase, as the difference between the measured and calculated data is smaller in Figure C.4b than in Figure C.4a.

Table C.1: Results from the Pawley analysis of the X-ray diffraction data from nanocrystalline $YMn_{0.85}Ti_{0.15}O_3$ for the hexagonal space group $P6_3cm$ combined with the orthorhombic space group $Pbam$ for the secondary phase YMn_2O_5. a, b, and c are the lattice parameters, and R_{wp} is the goodness of fit.

Sample	**Space group**	***a* [Å]**	***b* [Å]**	***c* [Å]**	**Crystallite size [nm]**	**R_{wp}**
N1(800)	$P6_3cm$	6.1333(15)	-	11.2788(16)	24.1(2)	3.033
N1(800)	$Pbam$	7.3156(18)	8.537(3)	6.6398(12)	35(3)	3.033

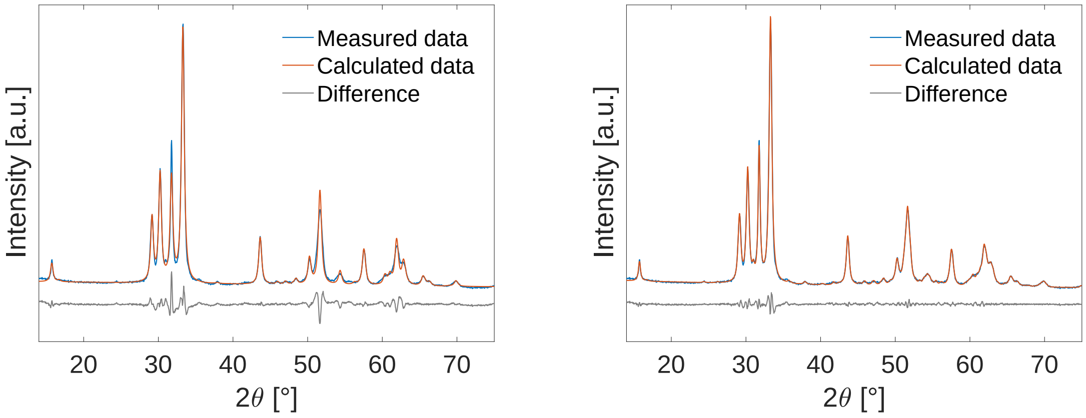

(a) **(b)**

Figure C.4: The results from the Pawley refinement of the X-ray diffraction data from the nanocrystalline $YMn_{0.85}Ti_{0.15}O_3$ (N1(800)). (a) The hexagonal space group $P6_3cm$, and (b) the hexagonal space group $P6_3cm$ combined with the orthorhombic space group $Pbam$.

Appendix D

Microstructure of produced powders

Scanning electron microscope (SEM) was used to investigate the approximate particle sizes of the prepared samples. Images of the powders from the bulk samples prepared by the solid state synthesis are presented in Figures D.1a to D.1e. Figure D.1f shows an image of the mortared and sieved nanocrystalline $YMn_{0.85}Ti_{0.15}O_3$ powder fired at 900 °C.

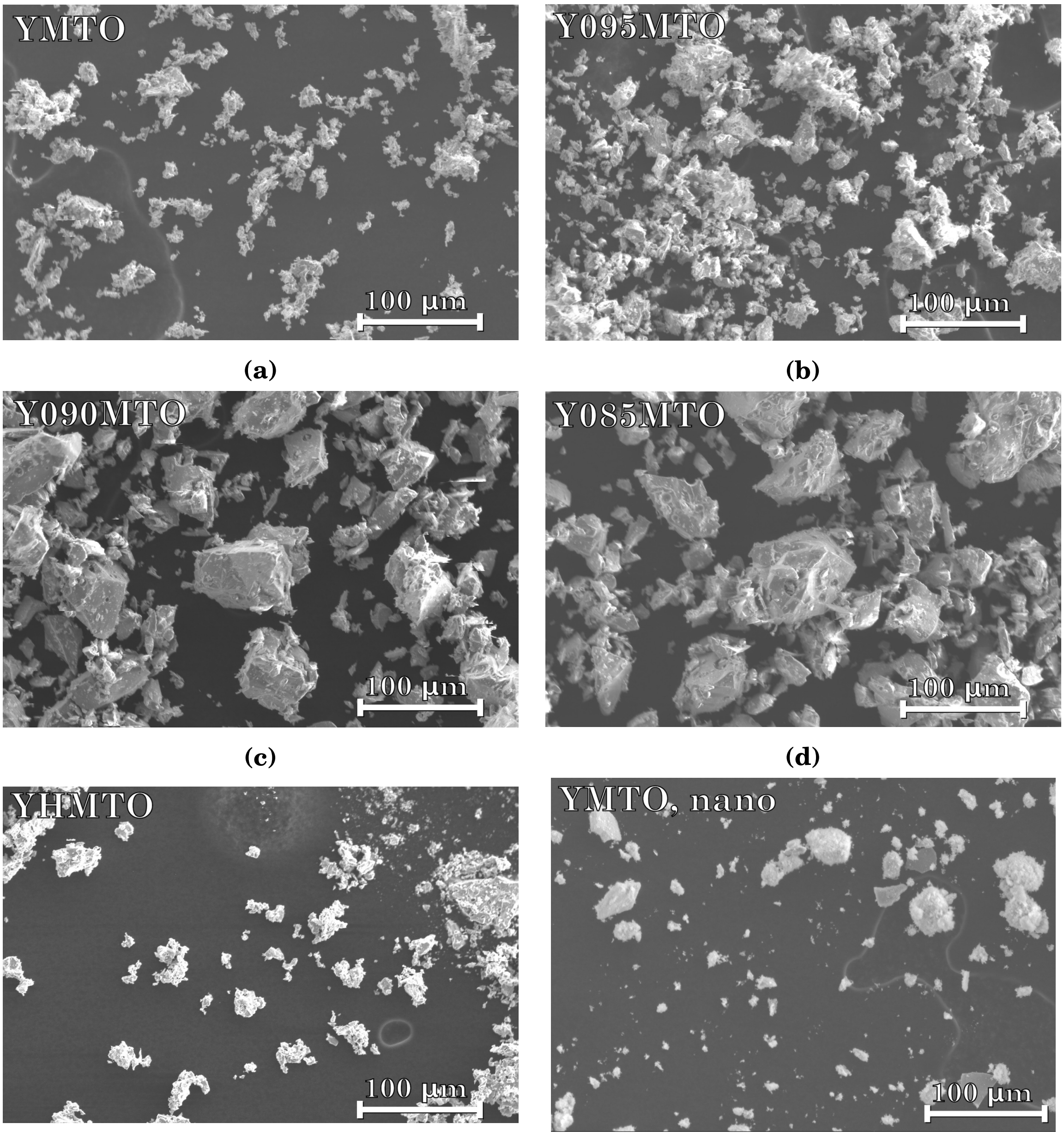

(a) **(b)**

(c) **(d)**

(e) **(f)**

Figure D.1: SEM images of the powders made from the solid state synthesis (a-e) and the citric acid method (f). (a) $YMn_{0.85}Ti_{0.15}O_3$, (b) $Y_{0.95}Mn_{0.85}Ti_{0.15}O_3$, (c) $Y_{0.90}Mn_{0.85}Ti_{0.15}O_3$, (d) $Y_{0.85}Mn_{0.85}Ti_{0.15}O_3$, (e) $Y_{0.95}Ho_{0.05}Mn_{0.85}Ti_{0.15}O_3$, (f) sieved nanocrystalline $YMn_{0.85}Ti_{0.15}O_3$.